

RICE UNIVERSITY

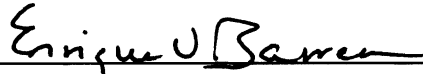
**A Multiscale Model of the Enhanced Heat  
Transfer in a CNT-Nanofluid System**

by

**Jonathan Winnie Lee**

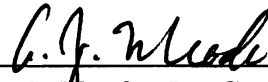
A THESIS SUBMITTED  
IN PARTIAL FULFILLMENT OF THE  
REQUIREMENTS FOR THE DEGREE  
**Doctor of Philosophy**

APPROVED, THESIS COMMITTEE:



---

Enrique V. Barrera, Committee Co-Chair  
Professor of Mechanical Engineering and  
Materials Science



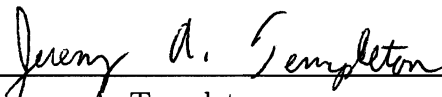
---

Andrew J. Meade, Jr., Committee  
Co-Chair  
Professor of Mechanical Engineering and  
Materials Science



---

Walter G. Chapman  
William W. Akers Professor of Chemical  
Engineering



---

Jeremy A. Templeton  
Technical Staff of Thermal/Fluid Science  
& Engineering at Sandia National  
Laboratories

Houston, Texas

April, 2011

## ABSTRACT

A Multiscale Model of the Enhanced Heat Transfer in a CNT-Nanofluid System

by

Jonathan Winnie Lee

Over the last decade, much research has been done to understand the role of nanoparticles in heat transfer fluids. While experimental results have shown “anomalous” thermal enhancements and non-linear behavior with respect to CNT loading percentage, little has been done to replicate this behavior from an analytical or computational standpoint. This study is aimed towards using molecular dynamics to augment our understanding of the physics at play in CNT-nanofluid systems. This research begins with a heat transfer study of individual CNTs in a vacuum environment. Temperature gradients are imposed or induced via various methods. Tersoff and AIREBO potentials are used for the carbon-carbon interactions in the CNTs. Various chirality CNTs are explored, along with several different lengths and temperatures. The simulations have shown clear dependencies upon CNT length, CNT chirality, and temperature. Subsequent studies simulate individual CNTs solvated in a simple fluidic box domain. A heat flux is applied to the domain, and various tools are employed to study the resulting heat transfer. The results from these simulations are contrasted against the earlier control simulations of the CNT-only domain. The degree by which the solvation dampens the effect of physical parameters is discussed. Effective thermal conductivity values are computed, however the piecewise nature of the temperature gradient makes Fourier’s law insufficient in interpreting the heat

transfer. Nevertheless, the computed effective thermal conductivities are applied to classical models and better agreement with experimental results is evident. Phonon spectra of solvated and unsolvated CNTs are compared. However, a unique method utilizing the Irving-Kirkwood relations reveals the spatially-localized heat flux mapping that fully illuminates the heat transfer pathways in the solid-fluid composite material. This method confirms why conventional models fail at predicting effective thermal conductivity. Specifically, it reveals the volume of influence that the CNT has on its surrounding fluid.

## Acknowledgements

Firstly, I would like to thank my advisors, Dr. Barrera and Dr. Meade. Dr. Barrera, it's pretty amazing that we first met in 1998 at Jones College. Then, when I came in 2006, you provided the perfect project topic for me when I had none. You gave me the freedom to choose my own direction. Dr. Meade, my Berkeley advisor, always with the jokes. From Day 1, you were always very open and accommodating. Thank you both for giving me the opportunity to study at Rice. Also, thank you for allowing me to pursue internships and collaborations at Sandia National Laboratories.

I am particularly grateful to Jeremy Templeton, my mentor at Sandia. Jeremy, I have learned so much from you, not only regarding LAMMPS and molecular simulation, but how to effectively present my research to others in various forms. Notably, wordsmithery! Thank you so much for the internships and our future endeavors, as well. Thanks for being so patient and flexible with your time. I could not have asked for a better mentor.

I also would like to thank Dr. Chapman. I first learned about molecular simulation in your class in Spring 2007, and it has certainly served me well. You are a wonderful instructor, and I am completely grateful that you were the one to teach it to me. You have provided several useful discussions over the years, and I very much enjoyed

bouncing ideas off of you. It has been very comforting to have you on my Qualifiers and Defense committees.

I owe thanks to Dr. Houchens and Dr. Bayazitoglu, who have been wonderful professors and committee members for me during my time at Rice. Dr. Houchens, I appreciate that you were always eager to discuss research topics with me. Your enthusiasm towards both teaching and research is greatly inspiring. Dr. Bayazitoglu, thank you for your kindness and confidence in me. Thanks for thinking of me when you come across nanofluid papers.

I would like to thank Sandia National Laboratories and my mentors, colleagues, and fellow interns during my time there. Bryan Wong, thank you for your guidance and friendship. I have learned a great deal from you, and I aspire to emulate your work ethic and research successes. Thanks for taking the time to work with me, despite not being in the field. Thank you also for allowing me to dabble in your field as we move forward. Jonathan Zimmerman, thank you for dedicating your time to help me learn. Thank you for introducing me to the EPSRI program and ultimately finding a good match for me in Jeremy. Reese Jones, thanks for helping me, particularly with the Irving-Kirkwood computations when you were abroad. Tricia Gharagozloo, thanks for all the advice and showing me the ropes in Montreal. Thanks to the Sandia interns of 2009 and 2010 for enjoyable summers in Livermore. Particularly, I would like to thank Andy Kung, Andrew August, Lucas Hale, and Jeff Lloyd. Finally, I owe thanks to Sandia High Performance Computing for providing computing resources.

Thanks to my colleagues in the Barrera group: Daneesh Simien, Grace Rojas, Qiang Zeng, Laura Peña Parás, Divya Chakravarthi, Marvin Cummings, Hubert Phillips, Jennifer Luna, Sukesh Shenoy, Pdraig Moloney, Yao Zhao, Claudia Arias, Andrés Rodela, Suman Khatiwada, Luke Boyers, Jaime Tijerina, and Dario Prieto; and the Meade group: Justin Kugler, Ankur Srivastava, Xiao Xu, and Matt Wilkinson. You guys have all been awesome. Jennifer, thanks for sticking through it with me, and I'm so sorry to leave you now. You can do it! And thanks for providing snacks at *both* my defenses! Yao, our most productive researcher and my RGA/RVA buddy (for a few years)—thanks for being a great friend and a true inspiration to me. Your work ethic is uncanny, and you will certainly go far. Also, thanks for the lunches! Ankur, Xiao, and Matt, thank you for being great officemates. I am grateful for having you guys around for our various discussions and certainly our times “screwing around.” And of course, special thanks go to my wonderful friend and Mexican super-cousin, Profesora Laura Peña Parás. You have provided invaluable support throughout the years in so many different ways. I cannot thank you enough for your help with my research, but more importantly, spending time joking around, hanging out, and playing El Rock Band with me. I will never forget the moment I found out we were fellow geeks. And artists! Sí man!

I would like to thank my grade school teachers, particularly Mr. Wilson Bascom and Mrs. Beverly Stross Sivaslian, for making school (science specifically) an enjoyable experience. Your guidance and encouragement has helped direct me along this path, and for that I am grateful.

I am thankful for my best friend, David Hwang. We've been through everything together. We first met in 1990 at 洛城中文學校, but we didn't become friends until a few weeks into school when we played G.I. Joe's one morning before class. Thanks for being there, through 黎明, Frost, Wootton, and my time away from home. Friends for 20+ years, I already feel like we're old men reminiscing sometimes. But I can always thank you for bringing me back to the present, back down to Earth. Thanks for the encouragement through all my endeavors, be they comics-, volleyball-, life-, or school-related. And thanks for the race. I win, by the way.

I would like to thank my dear Houston friends who have kept me entertained and loved these past five years: Nori Nagaya, Mihir Choudhury, Laura Peña Parás, Nick Parra-Vasquez, Jennifer Luna, Stan Chang, Jenchi Chang Tsou, Mike Chen, Brian Sheen, Bing Wen, Robert Wanichakorn, Lee Chang, Thomas Le, Annie Ma, Lina Fuh, Billy Wang, Jacky Huang, Yao Zhao, Wei Chen, Jiehong Liao, Galen Papkov, Fung Ou, Pete Lukkana, Josephine Hsu, Cary Riina, Nick Tiee, Mark Cheng, Fernanda Ruiz, and Carol Chuang. Mihir, my first teammate at Rice, I am so grateful for meeting you when I did. You provided a centerpiece to build around for all the teams we have played on. Also, thanks for the help with the Fourier Transforms! Laura, you get a double-shoutout because you are just that awesome. Nick PV, thanks for helping me survive grad school and always being there to discuss whatever. "Discuss." Thanks for the late night dinners and the football games. Go Bears! Stan and Jen, thanks to both of you for making me feel so welcome and at home in Houston. Wei, my good luck charm, thank you for being my setter, my deputy, and most importantly, my friend. Thanks for holding down the fort

while I was away. Thanks for the 9-man seasons, and here's to many more! Long live 龍星! Jie and Galen, thank you guys for making volleyball fun. You two were my coaching guinea pigs, and I loved teaching and playing with both of you. Thanks for the fantastic vacation in Hawaii and the 9-man tournaments! Pete, thanks for putting up with my amateur coaching and supporting me through it all. You believed in my potential and challenged me to be better. Cary, thanks for your passion and your craziness. I can never forget the pterodactyl scream and the Tigers! Baby Nick, thanks for being simultaneously awesome and awkward. Thanks for supporting me through Rice Volleyball and coming out to Boston for 9-man. Fernanda, thank you for entertaining me every day during my time in California. Thanks for encouraging me to get out and have fun (but also calling me a slacker). Lastly, 可柔, thank you for being such a kind, caring, and dependable friend. We've only known each other briefly, but thank you for being so supportive of all my endeavors, and thank you for spending so much time with me when you had better things to do. To my Houstonian friends, I love you all very much!

I would like to thank the past and present members of the Rice Men's Volleyball Club: Cary Riina, Wei Chen, Nick Parra-Vasquez, Nick Tiee, Pete Lukkana, Mihir Choudhury, Brett Kaufman, Stan Chang, Galen Papkov, Mark Cheng, Tyler Young, Daniel Young, Sean Murray, David Heleniak, Andrew Briggs, Tony Kellems, Kyung Oh, Ray Throckmorton, Brian Gilcrease-Garcia, Mark Ware, Henry Zhang, Nate Lee, Storm Slivkoff, Ryan Glassman, Vince Wang, Gianmarco Raddi, Chris Roy, Scott Norgaard, Kevin Lin, Aaron Sharpe, Michael Yu, Michael Tang, Steve Bachicha, Shidong Chen, Ray Wong, Matti Gralka, Paul Haugen, and Joseph Song. You are all great friends and



teammates, and I loved playing with all of you. To our guest coaches, Jessica Holderness, Karen Morgan, Ekaette Shammah, Tracey Lam, and Jordan Meredith, thank you for contributing the time to help make my job easier. Big thanks to Justyna Brewczyk for your dedication, passion, and friendship. We are undoubtedly better because of you. I appreciate you all contributing to this club and allowing this pet project of mine to come to fruition. Best of luck for the future!

Lastly, I would like to thank my family. To all my uncles and aunts, and to my cousins: 啲寶, Justin, 乖寶, 歡歡, Jamie, John, Larry, Andy, Eugene, Cindy, Tony, and Amy, I thank you all for your love, support, and being so inspirational to me growing up. 大寶, of course, I must thank you for giving me my name. Thanks for being a wonderfully caring 姊姊. Of course, we don't always agree on things, but I know at the end of the day, you are there looking out for me. Thanks for helping me through school, life, and shopping! Oh, and thanks for the cars, too. They've been handy.

爺爺、奶奶，我好想念您們。從小您們就特別關心我、稱讚我。現在您們看不見我完成學業，可是我想您們在天上一一定也為我高興，而且誇獎著說：「小寶書讀得真好，了不起！我們家的孩子都很了不起！」

公公、婆婆，我非常感謝您們從小給我的教誨。小時候從學校回家，我就知道您們一定煮好了我喜歡的綠豆湯等著我。我無聊的時候，拉著公公打籃球，找婆婆學畫畫，或者我們三個人一起打麻將。我練彈鋼琴的時候，您們總是專心地聽。

謝謝您們對我的學習這麼的關心，也因此我一路把博士念完。公公，您在天上好嗎？謝謝您和婆婆對我這麼好，我愛您們！

Finally, I would like to give a very big thank you to my parents. It is because of your belief in me (and certainly a good deal of prodding) that I have been able to come this far. At times, it seemed I could not find a single person more interested in my studies than you two. Commonly, I would hear, “ok, 趕快去讀書了！不做功課，就早點去休息！” at the end of phone conversations. Unintentionally amusing, but I understand. You have always kept me diligent, despite my tendencies otherwise. I hope this thesis is a strong indication that you have done a good job, and I hope that I have made you proud.

Thank you all! And in case I don't see you, good afternoon, good evening, and good night!

This project was supported by the Welch Foundation Grant: C-1494.

# Contents

Abstract	ii
Acknowledgments	iv
List of Figures	xiii
List of Tables	xxi
<b>1 Introduction</b>	<b>1</b>
<b>2 Molecular Dynamics</b>	<b>19</b>
2.1 Introduction . . . . .	19
2.2 Classical Molecular Dynamics . . . . .	20
2.2.1 Statistical Mechanics . . . . .	20
2.2.2 Molecular Dynamics Algorithm . . . . .	25
2.2.3 Interaction Potentials . . . . .	27
2.2.4 Boundaries . . . . .	32
2.2.5 Thermostats . . . . .	34
2.3 Thermal Conductivity . . . . .	36
2.3.1 NEMD Method . . . . .	36
2.3.2 EMD Method . . . . .	38
2.4 AtC . . . . .	39
<b>3 Simulation</b>	<b>41</b>
3.1 General Procedure . . . . .	41
3.1.1 Initialization . . . . .	41
3.1.2 Minimization . . . . .	43

3.1.3	Equilibration . . . . .	44
3.1.4	Temperature Ramping . . . . .	44
3.1.5	Steady State . . . . .	45
3.1.6	Post Processing . . . . .	46
3.2	Domain-Specific Procedures . . . . .	46
3.3	Interaction Potentials . . . . .	47
<b>4</b>	<b>Unsolvated CNT</b>	<b>49</b>
4.1	Introduction . . . . .	49
4.2	Computational Details . . . . .	60
4.3	Results and Discussion . . . . .	65
4.4	Phonon Density of States . . . . .	71
4.5	Conclusion . . . . .	80
<b>5</b>	<b>Solvated CNT</b>	<b>83</b>
5.1	Introduction . . . . .	83
5.2	Computational Details . . . . .	86
5.2.1	Initialization and Equilibration . . . . .	87
5.2.2	Generating the Temperature Gradient . . . . .	90
5.3	Results - One-Dimensional Analysis . . . . .	93
5.3.1	CNT in Vacuum . . . . .	93
5.3.2	CNT in Fluid . . . . .	96
5.4	Results - Phonon Analysis . . . . .	101
5.5	Results - Irving-Kirkwood-based Analysis . . . . .	105
5.6	Conclusion . . . . .	119
<b>6</b>	<b>Conclusions and Future Work</b>	<b>121</b>
	<b>Bibliography</b>	<b>127</b>

## List of Figures

- 1.1 A summary of TC enhancements of CNT-nanofluids in the literature. Each series of lines denotes a different set of experiments, which is a proximate reason for the variation. In general, the large spread in the data suggests the system may be sensitive to many factors, and significant work is necessary to understand these sensitivities. . . . . 8
- 4.1 A summary of TC measurements of (10,10) SWNTs in the literature. Blue markers denote MD simulations performed with the Tersoff potential. Red markers denote MD simulations performed with the REBO potential. Black markers indicate experimental measurements taken of SWNTs with unknown chiralities, i.e., not necessarily (10,10). 58
- 4.2 An example of the time-averaged temperature gradient of a CNT in vacuum simulation. Depicted here is a 100 nm (6,6) CNT at 300 K computed with the direct method using the Tersoff potential. Note the non-physical behavior at the ends of the CNT, and the monotonic trend throughout. A least-squares linear line is used to fit the data sufficiently far away from the source/sink regions. . . . . 64

- 4.3 TC measurements of CNTs at various lengths with numerical variations for (a) (10,10), (b) (6,6), (c) (10,0), and (d) (9,0) chiralities. Measurements are plotted offset from nominal CNT lengths, which are denoted by the dashed lines. Arrows indicate particular simulation ensembles of which some or all produced oscillatory temperature gradients. . . . . 66
- 4.4 TC measurements of CNTs at various temperatures using the Ikeshoji Method with the Tersoff potential for (a) (10,10) and (b) (9,0) chiralities. In agreement with the classical limit, TC decreases with increasing temperature due to Umklapp processes. . . . . 67
- 4.5 A superposition of the (10,10) CNT spread from the current study on Figure 4.1. The spread is denoted by the minimum to maximum of all the measurements, aggregated by length. The axes are zoomed relative to Figure 4.1 to highlight the general trend. . . . . 68
- 4.6 Two other examples of the time-averaged temperature gradient of a CNT in vacuum simulation. Both are from the same set of replicate simulations of a 100 nm (6,6) CNT at 300 K using the Ikeshoji Method with the Tersoff potential. (a) The temperature profile in this case is approximately linear within the line-fitting region. (b) The temperature profile here resembles a standing wave and has potential to significantly alter the measured TC. Note the difference in slopes relative to one another. Notice also that the Ikeshoji Method does not directly control the temperature gradient, and may result in much larger slopes compared to the direct method (see Figure 4.2). . . . . 70

4.7 The (a) longitudinal and (b) transversal DOS of a 25 nm (10,10) CNT simulated in equilibrium conditions at 300 K. The blue spectra is computed with the Tersoff potential while the red spectra represents the AIREBO simulation. While a few features are similar, particularly in the range less than 30 THz, the two spectra contain decidedly different features. The inset in (a) shows the comparison at low frequencies. . . . . 74

4.8 The (a) longitudinal and (b) transversal DOS of a 100 nm (6,6) CNT simulated with the Tersoff potential using the direct and Ikeshoji methods. The green spectra come from the direct method simulations, and the Ikeshoji Method simulations is represented by the blue and red spectra. The blue spectra come from the replicate runs which produced the smooth temperature gradients, as seen in Fig. 4.2. The red spectra come from the replicate runs which produced the oscillatory temperature gradients, as seen in Fig. 4.6. The insets show the magnified the low frequency behavior. The Ikeshoji Method enhances the low frequency peaks, particularly in the oscillatory temperature gradient cases. . . . . 76

4.9 A comparison of DOS spectra with variations in physical parameters. All DOS spectra are from (6,6) SWNT simulations using the AIREBO potential. The blue spectra denote simulations performed at 200 K, and the red spectra are from 400 K simulations. (a) and (b) are Longitudinal spectra of 25 nm and 100 nm long CNTs, respectively. (c) and (d) are the analogous Transversal spectra. Insets in all figures magnify the key differences. . . . . 78

- 4.10 A comparison of DOS spectra with variations to zigzag-type chiralities. All spectra are from 300 K simulations using the AIREBO potential with the Ikeshoji Method. The blue spectra denote simulations of (9,0) CNTs, and the red spectra denote simulations of (10,0) CNTs. Both CNTs are approximately 400 nm in length. Comparisons between the chiralities are shown for (a) the Longitudinal spectra and (b) the Transversal spectra. Insets in all figures magnify some key differences. . . . . 79
- 5.1 An example of the time-averaged temperature gradient of a CNT in vacuum simulation. Depicted here is a 100 nm (6,6) CNT at 300 K. The source/sink regions are denoted by the black dotted lines and the line-fitting region is denoted by the red dotted lines. Note the non-physical behavior at the ends of the CNT, and the monotonic trend throughout. The least-squares linear line, depicted in blue, is fit the data sufficiently far away from the source/sink regions and used to compute an effective thermal conductivity of the unit cell. . . . . 94
- 5.2 TC measurements of CNTs with various lengths and chiralities. The chiralities are depicted with different colors. Simulations were performed at a nominal temperature of 300K using the Ikeshoji method. The AIREBO potential was used for carbon-to-carbon interactions. . . . . 95



- 5.3 An example of the time-averaged temperature gradient of a CNT in fluid simulation. Depicted here is a 25 nm (6,6) CNT initialized to 300 K. The red data points refer to the CNT temperature while the green data points indicate the fluid temperature. The system temperature is shown in black. Note the piecewise nature of the profile due to the presence of the CNT. A least-squares linear line is used to fit the data sufficiently far away from the source/sink regions. This particular example produces a TC of approximately 0.8692 W/mK, which corresponds to a 163.4% enhancement, relative to a base fluid conductivity of 0.33 W/mK. This enhancement does not directly correspond to macroscopic enhancements measured in experiments, but merely provides a measure for comparison. . . . . 97
- 5.4 HC model applied to enhancement results from MD simulation cases. The experimental data from Figure 1.1 is overlaid. The model still suggests a roughly linear trend in the region of interest, however the model produces values that are on a similar order of magnitude as the experimental data. Cases 2 and 3 are highlighted in red because they both represent more physically-motivated examples than the rest. 102
- 5.5 The same data as presented in Figure 5.4 without the experimental data. The axes are zoomed out to display more concentrated loading percentages and the emergence of nonlinearity. The nonlinearity becomes particularly apparent with Cases 2 and 3. . . . . 103

- 5.6 The (a) longitudinal and (b) transversal DOS of a 100 nm (6,6) CNT simulated at 300 K. The blue spectra is from the CNT in vacuum simulations while the red spectra is the corresponding solvated case. The CNT in vacuum case presented here was subjected to a  $4.806 \times 10^{-7}$  W heat flux using the Ikeshoji Method. While the overall features remain the same, the low frequency peaks are highly attenuated in the solvated case. The inset shows the comparison at low frequencies. A distinct feature of the vacuum simulation is a large first peak below 1 THz. The aqueous simulation specifically does not share this feature. The large peak near 50 THz is narrowed and most features appear to be blueshifted and smoothed. . . . . 106
- 5.7 The (a) longitudinal and (b) transversal DOS of a 25 nm (10,10) CNT simulated at 300 K. The blue spectra is from the CNT in vacuum simulations while the red spectra is the corresponding solvated case. The CNT in vacuum case presented here was simulated in an equilibrium environment with no applied fluxes. The comparison is very similar to Figure 5.6. Most features appear in both spectra, except the low frequency peaks are noticeably washed out in the aqueous simulations. The in-fluid peaks in general are also blueshifted. 107
- 5.8 A diagram of the domain where the blue box and red tube represent the fluid box and CNT, respectively. The diagram is not drawn to scale. The cylinder shows data is averaged over  $\theta$  and collapsed onto the green plane. The green plane is the area shown in each of the subsequent mappings. . . . . 112

- 5.9 An example of the time-averaged longitudinal heat flux density of a CNT in fluid simulation. Depicted here is a 25 nm (6,6) CNT, Case 1 from Table 5.3. The top-most plot shows the fluid-fluid heat flux density with the solid-solid heat flux density overlaid using a different scale. The other two plots show the fluid-solid and solid-fluid heat flux densities. The longitudinal components of the heat flux density vector show boundary conditions accurately persisting through the fluid until the CNT disrupts the “bulk” behavior. The CNT carries much of the heat transport load, particularly closer to the center. . . . 113
- 5.10 An example of the time-averaged radial heat flux density of a CNT in fluid simulation. Depicted here is a 25 nm (6,6) CNT, Case 1 from Table 5.3. The top-most plot shows the fluid-fluid heat flux density. The other two plots show the fluid-solid and solid-fluid heat flux densities. The radial components of the heat flux density vector show relatively zero heat flux radially except at the solid-fluid interface. . . . 114
- 5.11 The temperature distribution from the 25 nm (6,6) CNT example above. Most of the temperature gradient exists in the fluid due to the lower thermal conductivity of the fluid. In the region near the CNT, the temperature gradient is diminished due to heat being primarily transported through the highly conducting CNT. . . . . 115
- 5.12 The distribution of computed TC values for the base fluid according to Equation (5.11). The distribution presented is evaluated from the Case 1 data presented in the above figures. Outlier values are truncated, and the mean value is 0.3247 W/mK. . . . . 116

- 5.13 The distribution of computed Kapitza resistance values for the interfacial boundary according to Equation (5.12) with slight modifications specified in the text. The distribution presented is evaluated from the Case 1 data presented in the above figures. Outlier values are truncated, and the mean value is  $1.36 \times 10^{-8}$  Km<sup>2</sup>/W. This value agrees in order of magnitude with results from Shenogin *et al.* . . . . . 117

## List of Tables

3.1	Interaction potential, potential coefficients, and reference for pairwise interactions. . . . .	48
3.2	Lennard-Jones 93 Wall interaction parameters. Only wall-water interactions are utilized in these studies. . . . .	48
4.1	TC results from previous computer simulations of isolated SWNTs at or near 300 K. . . . .	57
5.1	LJ interaction potential coefficients and reference for pairwise interactions. Carbon-carbon interactions are modelled with the AIREBO potential. The LJ 9-3 wall is described later and has a modified functional form from the usual LJ potential. . . . .	88
5.2	TC values of selected CNT in vacuum simulations at 300K. . . . .	96
5.3	Cases of solvated CNT simulations performed. . . . .	98
5.4	TC enhancements of solvated CNT simulations assuming base fluid TC of 0.33 W/mK. . . . .	99

# Chapter 1

## Introduction

Fluids have long been used for heat transfer purposes, including vehicular and avionics cooling, heating and cooling systems in buildings, as well as numerous industrial processing plants. With the onset of Micro-Electro-Mechanical Systems (MEMS) and nanotechnology, the pursuit of miniaturization has made heat transfer fluids (HTFs) all the more important. Many other technologies ranging from fuel cells to space suits require new and innovative cooling systems as well [1, 2].

HTFs typically (unfortunately) have relatively low thermal conductivities (TCs). Water for example, is roughly three orders of magnitude less conductive than copper. What fluids lack in TC however, is compensated by their ability to flow. The primary mechanism for heat transfer in fluids is convection. Still, if the TC of an HTF were enhanced, the HTF would be much more effective. Thus came about the idea to introduce conducting particles into fluids. Such an option was considered over a century ago; James Clerk Maxwell pioneered the field and formulated a method to calculate the effective conductivity of such a suspension [3]. This work was later followed up in the early 1900's (Maxwell-Garnett), 1960's (Hamilton and Crosser), and 1970's (Rocha and Acrivos) to account for particle shape [4–7]. While such models worked well for HTFs of the time, namely suspensions of micro- and macro-sized

particles, those HTFs proved problematic for implementation. For example, micro- and macro-sized particles tended to sediment too rapidly unless circulation rate was increased. In addition, increasing flow also increased erosion of the heat transfer devices. Furthermore, fluids of this type have considerably larger pressure drops, thus making flow through small channels much more difficult. Using suspensions for HTFs was therefore temporarily halted [1].

Modern materials technology has allowed the opportunity to revisit the HTF-suspensions route. In the 1990's, Stephen Choi from Argonne National Laboratories (ANL) proposed the idea of suspending nanoparticles [2]. He designated this new type of fluid a "nanofluid." The beauty of this concept is that nanofluid HTFs (n-HTFs) don't have many of the problems associated with the large-particle suspensions. Furthermore, since the suspended particles have a higher surface area to volume ratio, the expected enhancement is increased even further. n-HTFs exhibit large enhancements for small increases in concentration as well as a dependence on the particle size. Most interesting from a research perspective is the anomalous TC enhancement - large deviations from contemporary theories [1, 2].

Three types of particles have been used for n-HTFs: ceramic, metallic, and nanotube. Ceramic n-HTFs were first tested in the late 90's by Choi's group at ANL [8]. They performed conductivity measurements on fluids that contained  $\text{Al}_2\text{O}_3$  and  $\text{CuO}$  nanoparticles in water and ethylene glycol. They observed linear increases in enhancement with respect to volume fraction. When ethylene glycol was used as the

base fluid, they observed a 21% enhancement at 4% volume fraction of CuO and an 18% enhancement at 5% volume fraction of Al<sub>2</sub>O<sub>3</sub>. When water was used as the base fluid, they observed a 12% enhancement at 3.5% CuO, and 10% enhancement at 4% Al<sub>2</sub>O<sub>3</sub>. Wang *et al.* [9] also measured TC of nanofluids with CuO and Al<sub>2</sub>O<sub>3</sub> but with smaller particle sizes. They tested water, ethylene glycol, and engine oil (Pennzoil 10W-30) as the base fluid. Their measurements indicate dependencies on particle size and method of dispersion. Xie *et al.* [10,11] measured Al<sub>2</sub>O<sub>3</sub> and  $\alpha$ -Al<sub>2</sub>O<sub>3</sub> nanofluids with even smaller nanoparticles, and observed the effect of particle size and base solution. In general, the more conductive the base fluid, the less enhancement is observed. Murshed *et al.* performed conductivity measurements on spherical and cylindrically-shaped TiO<sub>2</sub> nanoparticles [12]. They showed a 33% enhancement at 5% volume fraction of 10 nanometers (nm)  $\times$  40 nm (diameter by length) rods, which was slightly greater than the enhancement from 15 nm-diameter spherical particles. They also observed a nonlinear dependence of TC enhancement with respect to particle concentration.

Metallic n-HTFs were first produced by Xuan and Li [13]. They produced copper particle-based nanofluids with transformer oil. The nanoparticles were approximately 100 nm in size, and the enhancement was reported to be 55% with 5% volume fraction. Subsequent groups utilized much smaller nanoparticles and achieved far greater enhancements. Choi's ANL group achieved 40% enhancement with 0.3% concentration of 10 nm sized copper nanoparticles in ethylene glycol [14]. Patel *et al.* [15]



used 10-20 nm gold nanoparticles and 60-80 nm silver nanoparticles. They found that for vanishingly small concentrations, the enhancements were still perceptible. The toluene-gold nanofluid was enhanced by 3-7% for volume fractions of 0.005-0.011%. The water-gold nanofluid enhancement was 3.2-5% for volume fractions of 0.0013-0.0026%. The relatively larger silver nanoparticles, despite having higher TC, provided less enhancement to the fluid conductivity. Hong *et al.* [16] reported 18% enhancement with 0.55% volume fraction of 10 nm sized Fe nanoparticles in ethylene glycol.

Carbon nanotube (CNT) n-HTFs have proved to be the most interesting and most promising. CNTs are a relatively new type of molecule comprised of only carbon atoms. They take the form of cylindrical tubules, as if sheets of graphene were rolled onto themselves. Due to their unique shape, aspect ratio, and composition, these materials display very unique properties [17-20]. CNTs have diameters of  $\mathcal{O}(1)$  to  $\mathcal{O}(10^{-1})$  nm and lengths of up to  $\mathcal{O}(10^1)$  micrometers. They are distinguishable by their chirality, which is a set of two integers that indicates how the tubule is rolled. Depending on the chirality, a CNT can be electronically conducting or semiconducting.

CNTs are special materials because they are highly anisotropic in shape as well as in TC. The TC along the tube-axis direction can be extremely high (typically reported as  $\mathcal{O}(10^3)$ W/mK), and it can be extremely low in the transverse directions (down to insulator-type values). CNTs have shown the largest TC enhancement of

all n-HTFs. In 2001, Choi *et al.* [21] produced nanofluids with CNTs and observed anomalous conductivity enhancements with respect to loading percentage. Choi *et al.* used multi-walled CNTs (MWNTs) suspended in engine oil with volume fractions up to 1%. The TC enhancement was observed to increase nonlinearly with respect to loading percentage, with an approximate 160% increase with 1% volume fraction loading. Generally, an additional technique such as adding a chemical surfactant or covalently bonding functional groups to the nanoparticle is performed to synthesize nanocomposites. These techniques are used to improve the interaction between solvent and solute, thereby improving dispersion and preventing precipitation.

Other works followed with various solvents, surfactants, and dispersion techniques. Xie *et al.* [22] used acid treatment to introduce hydrophilic functional groups to their MWNTs (treated CNTs abbreviated as TCNTs), and produced suspensions with distilled water (DW), ethylene glycol (EG), and decene (DE) as the solvents. The DW and EG suspensions required no surfactants, while the DE suspension used a small amount of oleylamine. Dispersion was achieved by sonication only. At 1% volume loading, the DW, EG, and DE suspensions achieved 6%, 12%, and 19% TC enhancements, respectively. It has been observed to be generally true that the relative enhancement decreases as the base fluid conductivity increases. It is inconclusive what causes the discrepancy with Choi *et al.*'s results, but possible contributing factors include choice of solvent, dispersion technique, and presence of functional groups. It is unclear what techniques Choi *et al.* used for achieving dispersion and stability of

their suspensions.

Liu *et al.* [23] created CNT-nanofluids using EG and engine oil as their base fluids. The engine oil suspensions used *N*-hydroxysuccinimide as a dispersant while the EG suspensions had no dispersants. Dispersion for both composite fluids was achieved with a combination of magnetic stirring and sonication. At 1% volume loading, the EG-CNT suspensions achieved a 13% conductivity enhancement compared to approximately 8% enhancement with the engine oil. However, at 2% volume loading, the engine oil suspension reached 30% enhancement. Ding *et al.* [24] produced nanofluids using DW as the solvent and Gum Arabic as the surfactant. They used sonication and high shear mixing to achieve dispersion and homogenization. At 1% loading by weight, they observed an 80% enhancement in thermal conductivity.

Marquis and Chibante [25] attempted to reproduce the results from Choi *et al.* They obtained two types of MWNTs, believed to be similar to those used by Choi *et al.*, and produced nanofluids with Poly- $\alpha$ -Olefin engine oil. At 1% volume, they observed an enhancement of 175% with one batch of MWNTs, exceeding Choi *et al.*'s. Hwang *et al.* [26] also processed MWNT nanofluids with DI-water and ethylene glycol as the base fluids. They used the transient hot-wire method to measure the effective TC of the composite fluid. At 1% volume, the EG-MWNT nanofluid measured a 30% enhancement and the DI-water-MWNT nanofluid measured a 11.3% enhancement.

Another study, by Assael *et al.* [27], tested various solvents, dispersants, and homogenization time. The CNT loading was kept constant at 0.6% by volume.

For the solvent, they mostly used water but they also tested a few cases with EG. Sodium dodecyl sulfate (SDS), hexadecyltrimethyl ammonium bromide (CTAB), *t*-octylphenoxypoly-ethoxyethanol (Triton X-100), and Nanospense AQ were all examined as various dispersants, with varying loading percentages. In general, their results suggest a convergence towards approximately 10% enhancement with increasing homogenization time, regardless of solvent and amount of dispersant. The enhancements are generally larger (and more scattered) with less homogenization time. Across these various experimental studies, it appears there is little agreement. However, since the materials used and procedures followed are all at least slightly different, the studies are not necessarily in disagreement.

Figure 1.1 shows the variation in experimental data for CNT-nanofluid enhancements. Note that Assael *et al.*'s data is not presented here since their data uses one loading percentage and varies many other parameters which cannot be displayed in this plot. In general, it is apparent that some groups achieve much larger enhancements than others. The amount of nonlinearity also varies significantly. This suggests that the system has many sensitivities. A systematic approach would be very useful in understanding the sensitivities and physics associated with this type of system. Theoretical work is required to better understand the nature of the thermal enhancements.

What follows will be a review of a few key models developed over the years that have progressed towards modelling CNT n-HTF systems. The first attempt at mod-



elling effective conduction through heterogeneous media was done in the late 19th century by Maxwell [3], and later revisited by James Clerk Maxwell-Garnett [4] (not to be confused with his godfather, James Clerk Maxwell). Maxwell's theoretical work dealt with electrical conduction through two media with a surface of separation. There are two conditions which are assumed to be true: 1) the condition that the potential must be continuous, and 2) the condition of 'continuity' of the electric currents. For the thermal analogue, the potential is similar to the temperature, and the electric current is like the heat current. In a resistor circuit, the potential drop across a resistor means electric current is flowing through it. Similarly, in a thermally conducting medium, a temperature gradient over the medium means there is a heat flux through it. The first condition, in thermal terms, means that the temperature at the interface should be the same in both materials. This is actually not quite the case, and will be revisited in Chapter 5. The second condition is that the heat flux measured at the interface should be the same on both sides, regardless of medium. In other words, there should be no accumulation of heat anywhere in the system. Maxwell's model is given as

$$\frac{\kappa^{eff}}{\kappa^f} = 1 + \frac{3(\kappa^s/\kappa^f - 1)\phi}{(\kappa^s/\kappa^f + 2) - (\kappa^s/\kappa^f - 1)\phi}, \quad (1.1)$$

where  $\kappa$  is the TC,  $\phi$  is the volume fraction of nanoparticles, and the superscripts *eff*, *f*, and *s* refer to "effective for the suspension," "base fluid," and "solid particle," respectively. This type of model is referred to as an effective medium theory (EMT).

The Hamilton-Crosser (HC) model [5,6] was the next significant advancement in

TC modelling for suspensions. Derived in Hamilton's Ph.D. thesis from 1960 and later published in 1962, this model is based on an extension of Maxwell's model. The mixture thermal conductivity in general is given by

$$\kappa^{eff} = \frac{\kappa^f (1 - \phi) \left(\frac{dT}{dx}\right)^f + \kappa^s \phi \left(\frac{dT}{dx}\right)^s}{(1 - \phi) \left(\frac{dT}{dx}\right)^f + \phi \left(\frac{dT}{dx}\right)^s}, \quad (1.2)$$

where  $(dT/dx)^f$  and  $(dT/dx)^s$  are the overall average temperature gradients of the two phases. Maxwell's theoretical work predicts the ratio of these gradients to be

$$\frac{\left(\frac{dT}{dx}\right)^s}{\left(\frac{dT}{dx}\right)^f} = \frac{n\kappa^f}{\kappa^s + (n - 1)\kappa^f}, \quad (1.3)$$

where  $n$  depends on the particle shape and ratio of TCs.  $n$  is defined by

$$n = \frac{3}{\Psi}, \quad (1.4)$$

where  $\Psi$  is the sphericity. The sphericity is defined as the ratio of the surface area of a sphere, with a volume equal to that of the particle, to the surface area of the particle [28]. Substituting Equation (1.3) into Equation (1.2) yields the HC model:

$$\frac{\kappa^{eff}}{\kappa^f} = \frac{\kappa^s/\kappa^f + (n - 1) - (n - 1)\phi(1 - \kappa^s/\kappa^f)}{\kappa^s/\kappa^f + (n - 1) + \phi(1 - \kappa^s/\kappa^f)}. \quad (1.5)$$

The result of the HC model has been displayed in Figure 1.1 as a solid black line. In the model, the thermal conductivity of the CNT is taken as 2000 W/mK and that of the fluid as 0.1448 W/mK. The sphericity is taken to be 6. Note that it largely underestimates the enhancement and produces a mostly linear response.

Yu and Choi presented renovated Maxwell and HC models in 2003 and 2004, respectively [28, 29]. They argued that due to interfacial phenomena, stabilizing agents,

adsorbed substances, ordered liquid layer, and other surface effects, the nanofluid should be modelled as three phases, rather than two. In this case, each solid particle is surrounded with a thin layer of intermediate TC. The “nanolayer,” as they call it, is a hypothesized phenomena, and it is very difficult to predict its size and properties, let alone prove its existence. The only experimental evidence of the nanolayer shows that it can only exist up to a few atomic diameters [1].

Regardless, Yu and Choi modelled the nanolayer with empirical variables for the thickness,  $t$ , and conductivity,  $\kappa^{nl}$ . They modelled the particle (CNT) as an ellipsoid with semiaxes  $a$ ,  $b$ , and  $c$  such that  $a \gg b = c$ . Then the equivalent TC of the particle plus nanolayer is given by

$$\kappa_j^s = \left( 1 + \frac{\kappa^s - \kappa^{nl}}{\kappa^s [rd(j, 0) - d(j, t)] - \kappa^{nl} [rd(j, 0) - d(j, t) - r]} \right) \kappa^{nl}, \quad (1.6)$$

where  $j$  ( $= a, b$ , and  $c$ ) is along the semiaxes directions of the ellipsoid,  $r$  is the volume ratio defined by

$$r \equiv \frac{1}{abc} \sqrt{(a^2 + t)(b^2 + t)(c^2 + t)}, \quad (1.7)$$

$d(j, v)$  is the depolarization factor defined by

$$d(j, v) \equiv \frac{1}{2} \sqrt{(a^2 + v)(b^2 + v)(c^2 + v)} \times \int_0^\infty \frac{dw}{(j^2 + v + w) \sqrt{(a^2 + v + w)(b^2 + v + w)(c^2 + v + w)}}, \quad (1.8)$$

and the superscript  $nl$  refers to the nanolayer. The value of  $v = 0$  refers to the outside surface of the particle, and  $v = t$  refers to the outside surface of the nanolayer.

Equation (1.8) satisfies the condition

$$d(a, v) + d(b, v) + d(c, v) = 1. \quad (1.9)$$



For a needle-shaped ellipsoid,  $d(a, v)$ ,  $d(b, v)$ , and  $d(c, v)$  tend to 0, 1/2, and 1/2, respectively. The equivalent volume concentration of the particle/nanolayer ellipsoid can be expressed as

$$\phi_e = \frac{\phi}{abc} \sqrt{(a^2 + t)(b^2 + t)(c^2 + t)} = r\phi. \quad (1.10)$$

Treating the second phase of the HC model as the particle/nanolayer combination, Equation (1.6) combines with Equation (1.5) to ultimately give

$$\frac{\kappa^{eff}}{\kappa^f} = 1 + \frac{n\phi_e A}{1 - \phi_e A}, \quad (1.11)$$

where  $A$  is defined by

$$A = \frac{1}{3} \sum_{j=a,b,c} \frac{\kappa_j^s - \kappa^f}{\kappa_j^s + (n-1)\kappa^f}. \quad (1.12)$$

Also worthy to note is that Yu and Choi redefined the shape factor from Equation (1.4) to

$$n = \frac{3}{\Psi^\alpha}, \quad (1.13)$$

where  $\alpha$  is an empirical parameter depending on the particle sphericity or eccentricity and the particle-to-liquid TC ratio. Yu and Choi used a value of  $\alpha = 1.55$  [28] to fit with Choi *et al.*'s experimental data [21]. The shape factor was generalized to a power law model particularly for extreme sphericity cases, and a non-unity value of  $\alpha$  further suggests the validity of this generalization.

Other variations of EMTs have been derived to consider various effects, e.g., the Leong model [30,31]. However, even as complexity is added to these models (and infa-

mous fitting parameters), the models' key weaknesses are that they cannot reproduce the nonlinear response that has been observed in experiments.

The work by Nan *et al.* [32–35] extends the Maxwell EMT [3, 4]. This theory is assumed valid for low concentrations of particles because the domains are considered to be spatially separated. Nan *et al.* introduced the interface boundary layer into their model. The effective TC is given by

$$\frac{\kappa^{eff}}{\kappa^f} = \frac{3 + \phi(\beta_x + \beta_z)}{2 - \phi\beta_x}, \quad (1.14)$$

where  $\beta_x = \frac{2(\kappa_{11}^c - \kappa^f)}{\kappa_{11}^c + \kappa^f}$  and  $\beta_z = \frac{\kappa_{33}^c}{\kappa^f} - 1$ . The parameters  $\kappa_{11}^c$  and  $\kappa_{33}^c$  are the equivalent thermal conductivities of the the composite unit cell in the transverse and longitudinal directions, respectively. They are given by

$$\kappa_{11}^c = \frac{\kappa^s}{1 + \frac{2a_K}{d} \frac{\kappa^s}{\kappa^f}}, \quad (1.15)$$

$$\kappa_{33}^c = \frac{\kappa^s}{1 + \frac{2a_K}{L} \frac{\kappa^s}{\kappa^f}}, \quad (1.16)$$

where  $a_K = R_K \kappa^f$ , and  $R_K$  is the interfacial thermal resistance, or Kapitza resistance [36].

In 1935, Bruggeman [37] developed a different type of EMT based on an average polarization theory. It is derived from considering incremental dispersed neighboring particles and the surrounding medium at each stage. The TC is integrated to form the final expression. More recently, Bruggeman's model was generalized for CNT composites [38, 39]. Factoring in CNT dimensions and the Kapitza resistance, the

effective TC is given by the following relation:

$$9(1-\phi)\frac{\kappa^{eff}-\kappa^f}{2\kappa^{eff}+\kappa^f}+\phi\left[\frac{\kappa^{eff}-\kappa_{33}^c}{\kappa^{eff}+L_z(\kappa_{33}^c-\kappa^{eff})}+4\frac{\kappa^{eff}-\kappa_{11}^c}{2\kappa^{eff}+(1-L_z)(\kappa_{11}^c-\kappa^{eff})}\right]=0, \quad (1.17)$$

where  $L_j$  is the depolarization factor depending on the nanotube aspect ratio  $P = L/d$ , expressed as

$$L_z = \frac{1}{2(P^2-1)^{3/2}} \left[ P \ln \frac{P + \sqrt{P^2-1}}{P - \sqrt{P^2-1}} - 2\sqrt{P^2-1} \right], \quad (1.18)$$

$$L_x = \frac{1-L_z}{2}. \quad (1.19)$$

Since Bruggeman's formulation is based on the consideration of neighboring particles, it assumes a denser system than the Maxwell-based models. This type of model predicts a nonlinear trend with respect to volume fraction.

The previous models are all continuum-based models attempting to capture molecular effects. Since the speculated sources of discrepancy are all atomistic-scale effects, i.e., particle size, particle shape, particle motion, surface action, electro-kinetic effects, liquid layering, and Brownian motion [1, 28, 29, 40–46], a more meaningful, albeit computationally expensive, method to understand this behavior should involve an explicitly atomistic model. However, there have only been a couple atomistic-scale simulations of CNT-nanofluid systems to study heat transfer.

The first atomistic heat transfer study of CNT-nanofluids is from Huxtable *et al.* [47] with follow-up publications by Shenogin *et al.* [48,49]. This study used molecular dynamics (MD) to simulate a SWNT solvated in octane to discern the interfacial

thermal resistance between the composite materials. The details of MD simulations will be discussed in Chapter 2. Essentially, MD simulations are atomistic models where atoms are simulated as point masses. The interactions between atoms are pre-defined, and Newton's laws of motion are applied to advance to subsequent time-steps. In Huxtable *et al.*'s simulations, two methods were performed to understand the heat transfer of the system. In the first method, the CNT temperature was increased instantaneously via velocity rescaling, and the system was then allowed to relax. In the second method, the solvated CNT is heated up with a constant heat source, and the same amount of heat was removed from a cylindrical bin of the surrounding fluid in the far-field. The temperature response of the fluid was monitored. This is similar to a method proposed by Ikeshoji and Hafskjold [50] except with a cylindrical geometry. The temperature eventually reaches a steady state, and the temperature drop at the interface is used to estimate the thermal resistance. Shenogin *et al.* report that the interfacial thermal resistance is equivalent to the resistance of about 5- to 15-nm thick layer of low conductivity matrix material. By extension, they report that due to this large thermal resistance, the majority of the temperature drop occurs at and is controlled by the interface.

Unnikrishnan *et al.* [51] performed a similar set of MD simulations as Huxtable *et al.* and Shenogin *et al.*. They simulated SWNTs and double-walled CNTs (DWNTs) in a fluid domain. Two fluids were tested: pure water and water with CuO additives. Interfacial resistance values are computed with the same techniques as Shenogin *et*

*al.* Values are quantitatively on the same order of magnitude. There is a marginal increase in thermal resistance when the water contains the CuO additive. Unnikrishnan *et al.* applied their Kapitza resistance values to some EMTs to compute TC sensitivity to Kapitza resistance and loading percentage.

Recently, Thomas *et al.* [52] also simulated heat transfer in a composite system with a CNT. They also used an MD approach, but simulated a water-filled SWNT (i.e., no surrounding liquid) to observe the influence of water in the tube axis. In this study, heat flow was simulated in the longitudinal direction by scaling the velocities in the end regions to effectively impose a heat flux. The resulting temperature gradient yields the TC via Fourier's law. This method is the one proposed by Ikeshoji and Hafskjold. They observed that the addition of water inside the CNTs causes the critical length for fully diffusive heat transport to decrease, and thus it exhibits a lower maximum TC. Furthermore, as the CNT radius decreases, the encased water becomes increasingly structured, which has a more concentrated effect of disrupting and eliminating low frequency phonons in the CNT. As a result, they postulate that bulk-like water on the outside of a CNT will have a relatively small effect on the TC compared to the structured water inside the CNT.

The aim of this dissertation is to use an atomistic model of a CNT-nanofluid to augment the current understanding of the physics at play in CNT-nanofluid systems, namely to understand the unexpected increase in TC and its nonlinearity. So far, researchers have theorized several mechanisms that could be responsible (or partly

responsible) for the anomalies between theory and experiment [1, 28, 29, 40–46].

The proposed model in this work is based on an MD framework. The base MD code is called LAMMPS (Large-scale Atomic/Molecular Massively Parallel Simulator) [53]. LAMMPS is a popular MD code developed at Sandia National Laboratories (SNL). The model utilizes an Atomistic-to-Continuum (AtC) coupling scheme also developed at SNL [54, 55]. The AtC package provides, but is not limited to, an intermediate post-processing step which allows a clean extraction of various output quantities and vectors. The base fluid is a simple coarse-grained model for water. Many variations of the model are explored, ranging from numerical technique variations (e.g., choice of force fields, choice of thermostat, and method of imposing/inducing temperature gradients) to physical system variations (e.g., CNT chirality, CNT radius, CNT length, solvation box size, and temperature). The base MD models will serve as unit cells for a HC-type analysis to compute the overall effective TC of the macroscopic bulk n-HTF. The phonon density of states for the CNTs in vacuum and aqueous environments are also compared.

Chapter 2 helps the reader to understand the basics of the numerical techniques used, namely Classical MD modelling and the AtC coupling scheme. Chapter 3 specifically discusses the general simulation setup and procedure used for the MD models. Chapters 4-5 present the domain-specific procedures and results of CNTs in vacuum and in solution. A final discussion of this project's achievements is presented in Chapter 6. A comparison of all the numerical results with experimental results

in the literature sheds light on the overall understanding of the important physics in nanoscale heat transfer. This comparison is discussed at length in this final chapter.

## Chapter 2

# Molecular Dynamics

### 2.1 Introduction

Computer simulation began in the 1950s when the electronic computing machines developed during and after the Second World War were put to use in a diverse range of applications. Molecular Dynamics (MD) is one of the two main forms of molecular simulation that spawned in this era (the other being Monte Carlo). The first MD simulations were performed in the late 1950s, and the basic algorithms are still essentially the same [56].

MD simulation is essentially the time integration of Newton's equations of motion in atomistic systems. Atoms (and molecules by extension) are allowed to interact with one another via interaction potentials. With large enough systems, integrated for sufficiently long time, one achieves statistical ensemble averages that reveal insight to the corresponding macroscopic domain. In this sense, it is the numerical realization of statistical mechanics.



## 2.2 Classical Molecular Dynamics

### 2.2.1 Statistical Mechanics

While MD is used for learning about physical properties of materials, those properties cannot be directly obtained from an MD simulation. The raw output of an MD simulation contains highly detailed information, i.e., the positions and velocities of all atoms in the system at each timestep. This information is hardly comparable to any sort of data a macroscale experiment might yield. Statistical mechanics allows one to translate the atomistic information into discernible macroscopic physical quantities. It provides an explanation of classical thermodynamics in terms of statistics and mechanics at the microscopic level. The following is a brief overview of some statistical mechanics concepts.

We denote  $\Omega(E, V, N)$  as the number of eigenstates with energy  $E$ , volume  $V$ , and number of particles  $N$ . It is then assumed that a system with fixed  $N$ ,  $V$ , and  $E$  is equally likely to be found in any of its  $\Omega(E)$  eigenstates. This is the underlying assumption of statistical mechanics [56]. Now let us consider a system with total energy  $E$  that consists of two weakly interacting subsystems. In other words, the sum of the energies of the subsystems,  $E_1$  and  $E_2$ , is equal to the total energy. For a given  $E_1$ , the number of degenerate states of the whole system is  $\Omega_1(E_1) \times \Omega_2(E - E_1)$ . It is more convenient to have quantities that are additive, which the natural logarithm conveniently yields:

$$\ln \Omega(E_1, E - E_1) = \ln \Omega_1(E_1) + \ln \Omega_2(E - E_1). \quad (2.1)$$

While each individual energy state of the total system is equally likely, the most likely distribution of energy maximizes the degeneracy  $\ln \Omega(E_1, E - E_1)$ . This condition is expressed as

$$\left( \frac{\partial \ln \Omega(E_1, E - E_1)}{\partial E_1} \right)_{N, V, E} = 0 \quad (2.2)$$

or, in other words,

$$\left( \frac{\partial \ln \Omega_1(E_1)}{\partial E_1} \right)_{N_1, V_1} = \left( \frac{\partial \ln \Omega_2(E_2)}{\partial E_2} \right)_{N_2, V_2} . \quad (2.3)$$

Common notation designates

$$\beta(E, V, N) \equiv \left( \frac{\partial \ln \Omega(E, V, N)}{\partial E} \right)_{N, V} . \quad (2.4)$$

Therefore, Equation (2.3) can be rewritten as

$$\beta(E_1, V_1, N_1) = \beta(E_2, V_2, N_2) . \quad (2.5)$$

When this condition is met, there is no longer any net exchange of energy between the two subsystems. In other words, the condition where the total degeneracy of the system  $\ln \Omega$  is maximized can be said to be in thermal equilibrium. It turns out this quantity can be related to the total entropy of the system:

$$S(N, V, E) \equiv k_B \ln \Omega(N, V, E) , \quad (2.6)$$

where  $k_B$  is Boltzmann's constant. Furthermore, it was shown that  $\beta_1 = \beta_2$  is the condition for thermal equilibrium. In common terms, when two systems are in thermal equilibrium, the temperatures are equal. Therefore,  $\beta$  should be in some way related

to the temperature. The thermodynamic definition of temperature is

$$\frac{1}{T} \equiv \left( \frac{\partial S}{\partial E} \right)_{V,N}. \quad (2.7)$$

It follows simply that

$$\beta = \frac{1}{k_B T}. \quad (2.8)$$

The probability that the system is found in a state where subsystem 1 has energy  $E_i$  can be expressed in terms of the degeneracy of subsystem 2 as follows

$$P_i = \frac{\Omega_2(E - E_i)}{\sum_j \Omega_2(E - E_j)}. \quad (2.9)$$

Expanding  $\ln \Omega_2(E - E_i)$  about  $E_i = 0$  gives

$$\ln \Omega_2(E - E_i) = \ln \Omega_2(E) - E_i \frac{\partial \ln \Omega_2(E)}{\partial E} + \mathcal{O}(1/E). \quad (2.10)$$

Substituting in Equations (2.6) and (2.7) yields

$$\ln \Omega_2(E - E_i) = \ln \Omega_2(E) - \beta E_i + \mathcal{O}(1/E). \quad (2.11)$$

Inserting this result into Equation (2.9) gives the Boltzmann distribution:

$$P_i = \frac{\exp(-\beta E_i)}{\sum_j \exp(-\beta E_j)}. \quad (2.12)$$

Given this expression, the ensemble average of any property,  $J$ , is given by

$$\langle J \rangle = \frac{\sum_i J_i \exp(-\beta E_i)}{\sum_j \exp(-\beta E_j)}. \quad (2.13)$$

The denominator is referred to as the partition function:

$$Z = \sum_j \exp(-\beta E_j). \quad (2.14)$$

The angled brackets here are used to denote the *ensemble average*. The ensemble average is the instantaneous average of the collection of phase-space states available to the system.

On the other hand, one typically refers to a system average as being an average of sequential measurements taken over a sufficiently long period of time, i.e.,

$$\bar{J} = \lim_{t \rightarrow \infty} \frac{1}{t} \int_0^t J d\tau \quad (2.15)$$

for continuous variables, or

$$\bar{J} = \lim_{t \rightarrow \infty} \frac{1}{t} \sum_i J_i \Delta t_i \quad (2.16)$$

for discrete variables, where the summation is over all time steps. These are referred to as the *time average*, denoted with the bar.

The “Ergodic Hypothesis” states that the ensemble average is equal to the time average, i.e.,

$$\langle J \rangle = \bar{J}. \quad (2.17)$$

While in general the Ergodic Hypothesis is not true, most systems of interest in computer simulations have been proven to be ergodic. In other words, the average of some property of the system can be determined through ensemble averaging or time averaging. This is particularly useful because MD simulations readily provide temporal information, but ensemble data can only be obtained by running numerous MD simulations with different initial conditions.

An ensemble is a comprehensive collection of all possible states of a system. There are a few thermodynamic ensembles that are particularly of interest in MD

simulations. Oftentimes a simulation domain will be allowed to equilibrate in an Isothermal-Isobaric Ensemble. This ensemble requires that the number of particles ( $N$ ), the system pressure ( $P$ ), and the system temperature ( $T$ ) be held constant, hence it is commonly referred to as NPT. Due to these constraints, a system in the NPT Ensemble will relax to the specified temperature and pressure.

Another common ensemble used for equilibration is the Canonical Ensemble. The Canonical Ensemble requires that  $N$ ,  $V$ , and system temperature ( $T$ ) be held constant. It is also commonly known as the NVT Ensemble. Since  $N$  and  $V$  are typically constants by default (from a programming standpoint), the NVT Ensemble can be conveniently invoked for thermostating purposes. For a system in the NVT Ensemble that is initialized with the incorrect amount of kinetic and potential energy, the applied thermostat will model the exchange of energy with a reservoir, which allows the kinetic energy to seek the specified temperature.

A third type of ensemble commonly found in MD simulations is the Microcanonical Ensemble. It requires a fixed  $N$ ,  $V$ , and total energy ( $E$ ), so it is commonly called the NVE Ensemble. This ensemble is the least “intrusive” to the system because  $N$ ,  $V$ , and  $E$  are all intrinsically held constant with the MD formulation. Due to its passive nature, it can be applied to systems (or subsystems) after they have been equilibrated and have reached steady state. It is generally during this steady-state period that a system’s thermodynamic information is time averaged for its ensemble average value.

### 2.2.2 Molecular Dynamics Algorithm

The basic structure of an MD algorithm is very simple. It consists of initialization and time integration. To initialize a system, each atom needs to be assigned a position and a velocity. Generally it is advantageous to assign positions based on a lattice and to allow the time integration to introduce “randomness.” Atom velocities are chosen from a random distribution and scaled to adjust for the desired kinetic energy. In thermal equilibrium,

$$\sum_i^N \frac{1}{2} m^i (\mathbf{v}^i)^2 = \sum_i^N \frac{dof^i}{2} N k_B T, \quad (2.18)$$

where  $m^i$ ,  $\mathbf{v}^i$ , and  $dof^i$  are the mass, velocity, and number of degrees of freedom of the  $i^{th}$  atom, respectively, and the summation is over all  $N$  atoms. From this, the instantaneous temperature  $T(t)$  can be adjusted to match the desired temperature  $T$  by scaling all velocity components by  $\sqrt{T/T(t)}$ . However, the system will likely change in order to seek the most probable energy partition, which corresponds to an equipartation of kinetic and potential energy. The initial assignment of temperature will likely change as the system seeks this special degenerate state. Insight into the potential energy of the initial configuration can help determine an initial kinetic energy that will expedite the equilibration of the system. There are also common techniques for eliminating overall linear or angular momentum from the system, if the user so chooses.

The time integration procedure is also straight-forward. For each timestep, there are two basic steps.

1. Find the net force applied to each atom
2. Update positions and velocities of each atom according to Newton's equations of motion

There are numerous contributions to the net force that can be considered. The interaction between or among atoms is determined by the interaction potentials. A few example choices for these potentials are discussed in Section 2.2.3. Electric and gravity fields can also provide contributions, for example. A fictitious offset force could be added to mimic Poiseuille flow. When all force contributions are summed together, the net force provides the instantaneous acceleration of the atom via Newton's Second Law:

$$\mathbf{F} = m\mathbf{a}. \quad (2.19)$$

One popular method of updating the position of an atom is called the velocity-Verlet algorithm [57, 58]. The derivation of the velocity-Verlet algorithm begins with the Taylor expansion of a particle's position about time  $t$ :

$$\mathbf{r}(t + \Delta t) = \mathbf{r}(t) + \dot{\mathbf{r}}(t) \Delta t + \frac{\ddot{\mathbf{r}}(t)}{2!} \Delta t^2 + \mathcal{O}(\Delta t^3). \quad (2.20)$$

The velocity on the other hand is incremented in half-timesteps. For the first half-timestep, the velocity is advanced by the acceleration at time  $t$ , whereas it is incremented by the acceleration at time  $t + \Delta t$  for the second half-timestep.

$$\dot{\mathbf{r}}(t + \Delta t/2) = \dot{\mathbf{r}}(t) + \frac{1}{2} \ddot{\mathbf{r}}(t) \Delta t + \mathcal{O}(\Delta t^2), \quad (2.21)$$

$$\dot{\mathbf{r}}(t + \Delta t) = \dot{\mathbf{r}}(t + \Delta t/2) + \frac{1}{2} \ddot{\mathbf{r}}(t + \Delta t) \Delta t + \mathcal{O}(\Delta t^2). \quad (2.22)$$

Substituting the first half-timestep velocity into the second yields

$$\dot{\mathbf{r}}(t + \Delta t) = \dot{\mathbf{r}}(t) + \frac{\ddot{\mathbf{r}}(t) + \ddot{\mathbf{r}}(t + \Delta t)}{2} \Delta t + \mathcal{O}(\Delta t^2). \quad (2.23)$$

The new position estimate from Equation (2.20) is accurate to order  $\Delta t^3$ , where  $\Delta t$  is the MD timestep. Using the new position, the new acceleration  $\ddot{\mathbf{r}}(t + \Delta t)$  is determined from the interaction potential. Then the new velocity estimate is obtained from Equation (2.23), and it is accurate to order  $\Delta t^2$ . The velocity is used to compute the kinetic energy and, thereby, the instantaneous temperature. With the positions updated and the instantaneous output recorded, the old positions,  $\mathbf{r}(t)$ , and velocities,  $\dot{\mathbf{r}}(t)$ , can be discarded.

### 2.2.3 Interaction Potentials

As mentioned previously, the force contributions from neighboring atoms are determined by the interaction potentials. Interaction potentials define the energy of an atom's interactions with its surrounding atoms, and, thereby, determine the force contributions. The force is given by the derivative of the potential energy with respect to the atomic position. Interaction potentials can be pairwise, such as the Lennard-Jones interaction, or many-body potentials, such as the Tersoff potential.

#### Lennard-Jones Potential

The Lennard-Jones (LJ) potential is a popular pairwise interaction, expressed as

$$U^{ij}(r^{ij}) = 4\epsilon \left[ \left( \frac{\sigma}{r^{ij}} \right)^{12} - \left( \frac{\sigma}{r^{ij}} \right)^6 \right], \quad (2.24)$$



where  $U^{ij}$  is the potential energy of the interaction between the  $i^{\text{th}}$  and  $j^{\text{th}}$  atoms,  $r^{ij}$  is the distance between the atoms, and  $\epsilon$  and  $\sigma$  are numerical parameters [59]. The parameter  $\epsilon$  is the energy of the potential well and  $\sigma$  is the (finite) distance at which the potential is zero. The parameters can be fitted to experimental data or quantum chemistry calculations. The  $r^{-6}$  term represents the long range attraction force, or van der Waals force, while the  $r^{-12}$  term models the Pauli exclusion principle. The terms are purely empirical, and the form is chosen out of computational convenience (since the  $r^{-12}$  term is the square of the  $r^{-6}$  term).

In computation, it is impossible to evaluate a potential out to a distance of infinity, so potentials are truncated with a cutoff distance. There are three commonly used forms of the truncated Lennard-Jones potential. The first simply terminates beyond the cutoff, i.e.,

$$U^{ij}(r^{ij}) = 4\epsilon \left[ \left( \frac{\sigma}{r^{ij}} \right)^{12} - \left( \frac{\sigma}{r^{ij}} \right)^6 \right], \quad r^{ij} < r_c, \quad (2.25)$$

where  $r_c$  is the cutoff distance.

Another common form is truncated and shifted so that the potential is not discontinuous at the cutoff location, i.e.,

$$U^{ij}(r^{ij}) = 4\epsilon \left[ \left( \frac{\sigma}{r^{ij}} \right)^{12} - \left( \frac{\sigma}{r^{ij}} \right)^6 \right] - U_c, \quad r^{ij} < r_c, \quad (2.26)$$

where  $U_c$  is the potential evaluated at the cutoff.

The third form uses a smoothing function in a range around the cutoff to smoothly force the potential to zero. The potential is evaluated according to Equation (2.25) within the inner cutoff distance, and multiplied by a function that gradually dies to

zero within a range between the inner and outer cutoffs. The Chemistry at HARvard Macromolecular Mechanics (CHARMM) MD code utilizes this type of implementation [60].

### **Bond Order Potentials**

Bond order potentials are a class of interatomic potentials which can be used to simulate different bonding states of an atom. Examples include the Tersoff potential [61–63], the Tersoff-Brenner potential [64], the Finnis-Sinclair potentials [65], the Reactive Empirical Bond Order (REBO) potential [66], and the Adaptive Intermolecular REBO (AIREBO) potential [67]. Bond order potentials are based on the Linus Pauling bond order concept [68] that the chemical bond strength depends on the bonding environment.

In the Tersoff potential, the energy  $U$  for a system of atoms is given by

$$U = \frac{1}{2} \sum_i \sum_{j \neq i} V^{ij} \quad (2.27)$$

$$V^{ij} = f_C(r^{ij}) [f_R(r^{ij}) + b^{ij} f_A(r^{ij})] \quad (2.28)$$

$$f_C(r) = \begin{cases} 1 & r < R \\ \frac{1}{2} - \frac{1}{2} \sin\left(\frac{\pi}{2} \frac{r-R}{S-R}\right) & R < r < S \\ 0 & r > S \end{cases} \quad (2.29)$$

$$f_R(r) = A \exp(-\lambda_1 r) \quad (2.30)$$

$$f_A(r) = -B \exp(-\lambda_2 r) \quad (2.31)$$

$$b^{ij} = (1 + \beta^n (\zeta^{ij})^n)^{-\frac{1}{2n}} \quad (2.32)$$

$$\zeta^{ij} = \sum_{k \neq i, j} f_C(r^{ik}) g(\theta^{ijk}) \exp[\lambda_3^m (r^{ij} - r^{ik})^m] \quad (2.33)$$

$$g(\theta) = 1 + \frac{c^2}{d^2} - \frac{c^2}{d^2 + (\cos \theta - \cos \theta_0)^2}, \quad (2.34)$$

where  $f_R$  represents a repulsive pair potential,  $f_A$  represents an attractive pair potential, and  $f_C$  is a smooth cutoff function to limit the ranged functions between  $r = R$  and  $r = S$ . The parameter  $b^{ij}$  provides a measure of the bond order, in which the three-body interaction is implicitly included.  $\zeta^{ij}$  is the effective coordination number, and  $\theta^{ijk}$  is the bond angle between bonds  $ij$  and  $ik$ .

The Tersoff-Brenner and REBO potentials are highly parametrized versions of the Tersoff potential which include terms that correct for an inherent overbinding of radicals. The potential is made continuous by using cubic splines in the modified

bond order term to interpolate between values at discrete numbers of neighbors. The AIREBO potential by Stuart *et al.* is nearly identical to the REBO potential, except a few fitted spline values are slightly different, and optional LJ and Torsional terms are included for longer range effects. The potential is expressed as

$$U = \frac{1}{2} \sum_i \sum_{j \neq i} \left[ U_{ij}^{REBO} + U_{ij}^{LJ} + \sum_{k \neq i, j} \sum_{l \neq i, j, k} U_{kijl}^{TORSION} \right], \quad (2.35)$$

where  $U^{REBO}$  is essentially the same as the REBO potential. The LJ term adds interactions beyond 2 Å. The torsional term is turned off for CNT simulations.

### Coulombic Interaction

Another common interaction potential is the electrostatic interaction that comes straight from Coulomb's Law:

$$U^{ij}(r^{ij}) = \frac{q^i q^j}{4\pi\epsilon_0 r^{ij}}, \quad (2.36)$$

where  $q$  denotes the charge of the atom and  $\epsilon_0$  is the permittivity of free space. Like the other potentials described above, this interaction is also truncated or smoothed beyond a cutoff distance. While the simulations that are performed in this project are not motivated by electrostatic interactions, the existence of a polar solvent would make the local effect of these interactions very important. Coulombic interactions from multiple sources can sometimes have a net long-range effect (e.g., parallel plate capacitors), so a few long-range Coulombic solvers exist, such as Ewald Sums and Particle-Particle Particle-Mesh (PPPM or P<sup>3</sup>M), which utilize Fourier space [69, 70].

### 2.2.4 Boundaries

Oftentimes, boundaries are used in MD simulations to prevent atoms from escaping the simulation domain. Two boundary types that are utilized in this research are described below. The first are Periodic Boundary Conditions (PBCs), and the second are Lennard-Jones 93 Walls.

#### Periodic Boundary Conditions

PBCs are a type of boundary condition used to model a large system by computing a small unit cell sufficiently far away from any edges. The simulated system is tiled out to infinity such that each tile is a perfect replica of the unit cell. When a particle exits one face of the unit cell, it reappears from the opposite face with the same velocity. The system is essentially infinite in size yet only the dynamics within the unit cell need to be computed. PBCs are commonly used in MD simulations to simulate bulk fluids and crystals.

#### Lennard-Jones 93 Walls

The LJ 93 wall is a boundary condition which acts as an attractive and repulsive wall. At long distances, it is attractive; at very close distances, it becomes repulsive.

It has the functional form

$$U^i = \epsilon \left[ \frac{2}{15} \left( \frac{\sigma}{r} \right)^9 - \left( \frac{\sigma}{r} \right)^3 \right], \quad (2.37)$$

where  $U^i$  is the energy of the  $i$ -th atom at a distance  $r$  away from the wall. The numerical parameters  $\epsilon$  and  $\sigma$  are similar to the ones in the LJ interaction potential. Much like the LJ potential, the LJ 93 wall has a positive term for near-field repulsion and a negative term for far-field attraction. The functional form is derived from integrating a half lattice of fixed solid LJ atoms.

It should be noted that LJ 93 walls are a source of error in conserving energy. With the LJ interaction potential, atoms exert equal and opposite forces on one another. In the case of the LJ 93 walls, the force exerted on the atoms is not exerted back on anything else in the system. In other words, the atoms are interacting with an object that is external to the system. It is important to ensure that the potential well of the LJ 93 wall is at least as deep as  $3k_B T$ , twice the kinetic energy of the system. Twice the kinetic energy is an approximate measure of the total energy of any given particle. If the energy level of the particle is less than the depth of the well, the LJ 93 wall will look approximately quadratic. The apparent harmonicity of the well will approximate an energy conserving interaction. If the energy is greater than the well depth, the particle will exit with a different amount of energy than it entered with. The unfortunate cost of this constraint is that atoms can potentially be trapped within the well.

### 2.2.5 Thermostats

Thermostats are a very important part of MD simulations. Thermostats regulate the temperature of the simulation, and effectively serve to equilibrate or relax the system during equilibration.

#### Velocity Rescaling

The simplest way to thermostat is to use velocity rescaling. This method is exactly as described in the initialization scheme at the beginning of Section 2.2.2. In summary, to change the temperature instantaneously from a starting temperature,  $T(t)$  to a desired temperature,  $T$ , one needs only to scale the velocities by  $\sqrt{T/T(t)}$ . This is a very robust method that forces the (instantaneous) temperature to match the desired temperature exactly. However, while this method is quick and convenient, it is actually a very poor thermostat. First of all, this thermostat does not sample from any particular ensemble. The methodology is not physically motivated. Secondly, an instantaneous change in temperature disturbs the interchange of kinetic and potential energies.

There are instances in this work where velocity rescaling will be utilized. For example, in some simulations, the total linear and angular momentum of a group of atoms may be periodically zeroed. The act of zeroing the momentum reduces the total kinetic energy of the group of atoms, causing the total energy, and hence temperature, of the system to drop. In this case, to maintain the correct kinetic

energy, the velocities of the group of atoms can be scaled back up to the original temperature. This process leaves the system unperturbed from an energy standpoint since the potential energy and kinetic energy are the same as before.

### Nosé-Hoover

The Nosé-Hoover thermostat is a deterministic thermostat very commonly used in MD simulations. The formulation was originally introduced by Shuichi Nosé [71] and later implemented by William G. Hoover [72]. The idea is that the system is in thermal contact with a larger heat bath. To simulate the interaction with the heat bath, an artificial force is added to the Hamiltonian of each thermostatted atom.

The modified Newton's Second Law is expressed as

$$m^i \dot{\mathbf{v}}^i = \mathbf{f}^i + \phi^i - \chi(t) m^i \mathbf{v}^i, \quad (2.38)$$

where the  $i$  superscript denotes the  $i$ -th atom,  $m$  is the mass,  $\mathbf{v}$  is the velocity,  $\mathbf{f}$  is the net interatomic force,  $\phi$  is the external force, and  $\chi$  is defined by

$$\dot{\chi} \equiv \frac{1}{\tau^2} \frac{T - T^*}{T^*}. \quad (2.39)$$

$T$  is the temperature,  $T^*$  is the target temperature, and  $\tau$  is a relaxation time (normally in the range  $0.5 \text{ ps} \leq \tau \leq 2 \text{ ps}$ ). The term  $-\chi(t) m^i \mathbf{v}^i$  is the artificial force added to the system. It should be noted that the Nosé-Hoover thermostat applied to only a portion of the entire system adds finite traces of angular momentum to the system. Only if it is applied to the entire specimen is the linear and angular momentum conserved, in which case the NVT ensemble is sampled.



## 2.3 Thermal Conductivity

Fourier’s law defines the TC of a material in terms of the heat current and the temperature gradient as

$$J_\mu = - \sum_\nu \kappa_{\mu\nu} \frac{\partial T}{\partial x_\nu}, \quad (2.40)$$

where  $J_\mu$  is a component of the thermal current in the  $\mu$  direction,  $\kappa_{\mu\nu}$  is an element of the TC tensor, and  $\partial T/\partial x_\nu$  is the gradient of the temperature  $T$  in the  $\nu$  direction. Experimentally,  $\kappa$  is typically determined by measuring the temperature gradient that results from the application of a heat current. In MD simulations,  $\kappa$  can be obtained from Non-Equilibrium MD (NEMD) [73–88] or Equilibrium MD (EMD) [73–76, 89–95] simulations. The two most common methods for computing thermal conductivity via MD are known as the “direct method” and the Green-Kubo method. The direct method is an example of an NEMD method, and the Green-Kubo method is an example of an EMD method. These methods will be discussed in detail in the following sub-sections.

### 2.3.1 NEMD Method

NEMD is directly based on Fourier’s law. It involves setting up a temperature gradient across the simulation domain, mimicing an experimental situation. This can be done by either imposing a temperature gradient or a heat flux.

### Imposed Temperature Gradient

The following method utilizes thermostats to fix the temperature at the ends of the domain. With the temperatures fixed, a steady state thermal gradient will develop across the system. Generally, one can expect the temperature near the thermostatted regions to exhibit some non-linear behavior [74]. The remaining temperature data can be time-averaged (and ensemble-averaged, if available) and fit to a linear line. This is  $\partial T/\partial x_\nu$  from Fourier's law.

Similarly, the energy injected to or extracted from the system via thermostats will also reach a steady-state rate. The amount of energy injected or extracted via thermostat can be monitored. This rate is also time-averaged (and ensemble-averaged, if available); this is  $J_\mu$  from Fourier's law.

Note that in this case,  $\mu$  and  $\nu$  are in the same direction. Therefore, this method is an evaluation of one diagonal component of the full TC tensor.

### Imposed Heat Flux

The Imposed Heat Flux method can be thought of as the opposite of the previous method. In this case, the heat flux is imposed and the temperature gradient is induced. There are numerous ways to accomplish this. The Müller-Plathe method achieves a heat flux by exchanging particle velocities in the “hot” and “cold” regions [77]. Another method utilizes the velocity rescaling technique, but rescales at a fixed rate rather than to a target temperature [50, 74]. This method was proposed

by Ikeshoji and Hafskjold [50], and will be referred to as the Ikeshoji Method for simplicity.

With this method, the heat flux current is known exactly, and the resulting temperature gradient is computed as in the previous method. Again, this evaluates a single component of the TC tensor.

The simulations done in this thesis primarily utilize this method, specifically the velocity rescaling technique. While velocity rescaling is a crude thermostat, it is acceptable in this situation because the heat flux to the system should be a flux of thermal energy. Velocity rescaling directly affects only the kinetic energy of the system.

### 2.3.2 EMD Method

The Green-Kubo method uses the fluctuation-dissipation theorem to compute the TC. Since the simulations are done in equilibrium, there is no driving force so the system is always in the linear-response regime. The Green-Kubo expression,

$$\kappa_{\mu\nu}(\tau_m) = \frac{1}{\Omega k_B T^2} \int_0^{\tau_m} \langle J_\mu(\tau) J_\nu(\tau) \rangle d\tau, \quad (2.41)$$

relates the equilibrium current-current autocorrelation function to the TC, where  $\Omega$  is the system volume, and the angle brackets denote the ensemble-average (or in the case of MD simulation, both time- and ensemble-average when available). The heat current is written as

$$\mathbf{J} = \frac{d}{dt} \sum_i \mathbf{r}^i(t) \epsilon^i(t), \quad (2.42)$$

where  $\mathbf{r}^i(t)$  is the time-dependent coordinate of atom  $i$  and  $\epsilon^i(t)$  is the site energy density. The site energy can be evaluated by summing half the pairwise potential energy with the atom's kinetic energy:

$$\epsilon^i \mathcal{V} = \frac{1}{2} m^i (\mathbf{v}^i)^2 + \frac{1}{2} \sum_j U^{ij}, \quad (2.43)$$

where  $\mathcal{V}$  is a unit volume. The benefit of this method is that the full TC tensor can be evaluated with one simulation, as opposed to the NEMD cases where a direction of thermal current is picked *a priori* and only the diagonal term in that direction is computed. The downside, however, is that the site energy is dependent on assigning a portion of the interaction potential energy to the site. In pairwise interactions, the choice is straightforward; the pairwise energy is divided in half. For three- and other many-body potentials such as Tersoff and AIREBO, this choice becomes more arbitrary.

## 2.4 AtC

Since the goal of this research is to understand the continuum-level phenomenon of heat transfer within an atomistic system, we will utilize a multiscale coupling scheme to interpret atomistic data in terms of continuum variables. Atomistic-to-Continuum (AtC), as implemented in LAMMPS, uses multiscale coupling definitions to create a coupled finite element (FE) and MD simulation and/or on-the-fly post processing of continuum fields. In this work, AtC will be used to post-process atomistic data so that it can be presented in a continuum sense. The method of projecting atomistic

data onto a FE mesh utilizes Hardy's formalism for atomistic-continuum equivalence [96–98].

Hardy defines the continuum fields of mass density,  $\rho$ , linear momentum density,  $\mathbf{p}$ , and internal energy density,  $e$  as functions of a fixed spatial point  $\mathbf{x}$  at time  $t$  in terms of the atomistic positions  $\mathbf{x}^i$  and velocities  $\mathbf{v}^i$  by using localization functions,  $\psi$ :

$$\rho(\mathbf{x}, t) = \sum_{i=1}^N m^i \psi(\mathbf{x}^i - \mathbf{x}), \quad (2.44)$$

$$\mathbf{p}(\mathbf{x}, t) = \sum_{i=1}^N m^i \mathbf{v}^i \psi(\mathbf{x}^i - \mathbf{x}), \quad (2.45)$$

$$e(\mathbf{x}, t) = \sum_{i=1}^N \left\{ \frac{1}{2} m^i (\mathbf{v}^i)^2 + \phi^i \right\} \psi(\mathbf{x}^i - \mathbf{x}), \quad (2.46)$$

where  $m^i$  and  $\phi^i$  are the mass and potential energy, respectively, of atom  $i$ . The summations are over all atoms ( $i = 1, 2, \dots, N$ ), and the localization function  $\psi$  allows each atom to contribute to the continuum property. It has units of inverse volume, is peaked at  $\mathbf{x}^i = \mathbf{x}$ , and tends to zero as  $|\mathbf{x}^i - \mathbf{x}|$  becomes large. Other quantities such as temperature, stress, and heat flux can similarly be projected onto a FE mesh. This method is used extensively in this work.

## Chapter 3

### Simulation

#### 3.1 General Procedure

The general procedure of the simulations can be broken down to the following steps:

1. Initialization
2. Minimization
3. Equilibration
4. Temperature ramping
5. Steady state and
6. Post-processing

Each of these procedures will be addressed in detail in the following subsections.

##### 3.1.1 Initialization

Initialization includes setting up the domain and assigning velocities. Setting up the atomic states can be quite challenging in some cases. Sometimes the positions are relatively simple, and they can be initialized in a lattice structure. Other times when

there are different components, the components may have to be set up separately and merged together such that the components are not in energetically unfavorable configurations. For example, a fluid might be initialized according to a simple-cubic lattice structure. However if there is a solvated molecule within the fluid, special care must be taken to avoid having overlapping molecules. Furthermore, one needs to be particularly aware *a priori* of the volume available to the solvating fluid. Many fluids are highly incompressible; perturbations to the fluid density can put the fluid in unphysical thermodynamic states.

The second part of initialization is assigning velocities. This procedure is explained in Section 2.2.2. One important aspect to consider when assigning velocities is the potential energy of the initial configuration. Typically a minimization procedure (Step 2) may be done to minimize the potential energy of the system. However sometimes it does not make sense to minimize a material (e.g., a fluid). Whatever the case may be, the state of the potential energy plays a large role in how the temperature will evolve initially. Take a simple harmonic oscillator as example: a pendulum. Assuming the system is isolated, the sum of the kinetic and potential energies is constant. When the pendulum is at the bottom in the vertical position, its potential energy is minimized and its kinetic energy is maximized. Similarly, when the pendulum is at the top of its swing, the potential energy is maximized and the kinetic energy is minimized. The “temperature” of the system would be the temperature evaluated at the position where the kinetic and potential energies are equal. In other words, the time-averaged

state of the pendulum yields an equipartition of energy. Since the minimized potential energy corresponds to the maximized kinetic energy, its instantaneous temperature should be equal to twice the time-averaged temperature. Therefore, it is common practice to minimize a system and then initialize the temperature to double the target temperature, allowing the system to naturally (and quickly) seek its equilibrium configuration. Now take the case where the initial potential energy is exceeding the targeted total energy. A negative kinetic energy is impossible. The best option would be to initialize all the velocities to zero. The potential energy would quickly convert a large portion to kinetic energy. Then it would be up to the thermostat to remove the excess energy.

### 3.1.2 Minimization

Minimization, as mentioned previously, is the recursive perturbation of particle positions in the direction of decreasing potential energy. Minimization does not include any time integration. It is in some ways similar to a Monte Carlo simulation. In general, minimization will only find a local minimum of the system, but ideally, it will place the system in an energetically stable configuration. Minimization is generally only performed for solid materials. There is no concept of potential energy for ideal gases. So as a material's phase shifts from solid to liquid to gas, the idea of minimization loses meaning.



### 3.1.3 Equilibration

Equilibration, also mentioned above, is the relaxation of a system to an energetically favorable partition of kinetic and potential energies. Typically this is done in an NVT ensemble so that the system temperature tends towards a target value and the total energy is not directly constrained. It may also be performed in an NPT ensemble if the domain is compatible to volume changes. Equilibration is achieved when the time-averaged temperature (and pressure, if applicable) settles on the target value. One test to determine if a system is equilibrated is to allow the system to subsequently run in an NVE ensemble to see if the temperature changes.

### 3.1.4 Temperature Ramping

There are two methods used in this dissertation to determine the thermal conductivity. Both methods are NEMD methods. The first is achieved by imposing a temperature gradient, as described in the first part of Section 2.3.1. Since the method requires an applied temperature gradient, the two ends of the system must be set to distinct target temperatures. Rather than instantaneously changing the temperature boundary condition, the boundaries are gradually changed over time to match the boundary conditions. This step is referred to as temperature ramping. The tail sections of domain are used to thermostat the edges. The target temperature of the thermostat is linearly ramped in time until the target temperature matches the final desired target temperature. Meanwhile, the rest of the domain is allowed to evolve according

to an NVE ensemble. Note, however, that this middle region of the domain does not necessarily have a fixed number, volume, and temperature because it interacts with the boundary regions. Denoting the ensemble as NVE is actually in this sense a misnomer. It really means the region is allowed to evolve without thermostats.

The second method used in this dissertation for determining the thermal conductivity is the Ikeshoji method, as described in the second part of Section 2.3.1. Here, the temperature gradient is induced by applying a heat flux to the system. This is done by adding or subtracting a specified amount of non-translational kinetic energy to the boundary regions periodically during the ramping phase. For convenience, this procedure will also be referred to as temperature ramping. The whole system will be run in the NVE ensemble since the temperature will no longer be regulated at either end.

### **3.1.5 Steady State**

After the temperature ramping phase, the temperature gradient must be held in place to collect a statistically significant time average of the system behavior. The procedure here is the same as before, but for the Imposed Temperature Gradient method, the target bath temperatures are held constant. Even though the temperature ramping phase was performed gradually over a period of time, a transient period following the end of the ramping phase should be expected. The system should be allowed some time to relax from the transient response, then the system can be considered in

steady state. The simulation should continue to run for a long period of time while in steady state to collect sufficient data for time-averaging.

In the Ikeshoji method, the transient period is the same as the temperature ramping period. In the Imposed Temperature Gradient method, however, the temperature ramping period is only a subset of the transient period.

### **3.1.6 Post Processing**

After the simulation has ended, the thermal data should be collected and time-averaged. Specifically, one needs to determine the time-averaged temperature gradient and time-averaged heat flux. Regardless of which was applied and which was induced, both could be expected to deviate from applied boundary conditions. Using Fourier's Law as a baseline model for comparison purposes, the temperature gradient and heat flux will yield the effective TC of the simulated atomistic domain.

## **3.2 Domain-Specific Procedures**

There are three particular domain-types that are explored in this study. The first is an individual, unsolvated CNT. The second is a water box. The third is an individual CNT solvated in a water box. A parameter space study will be performed on these three domain-types. The aim of this approach is to determine what effect the presence of the fluid has on the thermal transport through the CNT. Conversely, one could think about this as an approach to study the effect that the presence of the CNT has

on the thermal transport through the fluid.

For each of the domain-types, the general procedure described in Section 3.1 has specific modifications and/or considerations. These will be discussed in Chapters 4-5.

### 3.3 Interaction Potentials

A number of interaction potentials were tried during the course of this work. The next chapter will discuss that study in more detail. The interaction parameters that were ultimately used for the reported results will be described in this section.

The water is modelled as a simple LJ fluid. Rather than modelling the full H<sub>2</sub>O molecule, the hydrogen atoms are ignored and the oxygen atom is charge neutral. This coarse-graining will be discussed further in later Chapter 5. The water-water interaction is taken from the oxygen-oxygen interaction from the TIP3P model [99]. Interactions between carbon atoms in the CNT are modelled with the AIREBO potential [66]. The water/carbon interactions are modelled using the LJ parameters from Werder *et al.*, which was parametrized to reproduce the experimentally observed contact angle of water on graphite [100]. Refer to Table 3.1 below for the parameters.

The wall boundaries that don't utilize PBCs will have Lennard-Jones 93 walls. Since the CNTs will not approach the walls, wall-CNT parameters do not need to be specified. The wall-water parameters are chosen such that the interaction is comparable to water-water interactions. The coefficients are listed in Table 3.2 below.

Table 3.1 : Interaction potential, potential coefficients, and reference for pairwise interactions.

Species 1	Species 2	Potential	Coefficients	Source
Fluid	Fluid	LJ	$\epsilon = 0.006596 \text{ eV}, \sigma = 3.1507 \text{ \AA}, r_c = 10 \text{ \AA}$	[99]
Fluid	CNT	LJ	$\epsilon = 0.004063 \text{ eV}, \sigma = 3.19 \text{ \AA}, r_c = 10 \text{ \AA}$	[100]
CNT	CNT	AIREBO	see [67]	[66]

Table 3.2 : Lennard-Jones 93 Wall interaction parameters. Only wall-water interactions are utilized in these studies.

$\epsilon$	$\sigma$	$r_c$
0.05 eV	3.3 Å	10 Å

## Chapter 4

# Unsolvated CNT

### 4.1 Introduction

\* Advances in a vast range of technologies including electronics, communication, and computing in the last few decades has led to a miniaturization of devices and increase in power density. Numerous other technologies such as aeronautics, automotives, and solar power also have an increasing demand for improved thermal management. One solution is the development of novel heat transfer materials based on CNTs. Significant amounts of research have been focused on CNTs for their unique characteristics [17–20]. Since CNTs are like one-dimensional versions of graphene, they exhibit preferentially biased thermal properties, which can be used advantageously. Across the various research efforts, TC measurements vary by two to three orders of magnitude. With this large spread, it is difficult to engineer useful applications for CNTs as heat transfer materials.

Experimental studies report a wide range of TCs for individual CNTs [102–106]. Kim *et al.* [102] first measured the temperature dependence of individual MWNT TC using a joule heating microfabricated device. Yu *et al.* [103] used a similar experi-

---

\*The work presented in this chapter has been published in Reference [101].

mental setup to measure the TC of an individual SWNT. Both reported an increasing thermal conductance with increasing temperature. Kim *et al.* measured over a wider range of temperatures, and showed a peak thermal conductance just above 300 K. They reported a room temperature TC value of 3000 W/mK using an estimate for the cross-sectional area (although the exact method of conversion from conductance to conductivity is unclear). By comparison, TC at room temperature in Yu *et al.*'s SWNTs was observed within a range between 2000 W/mK and 10,000 W/mK, depending on their estimates for the geometry. Nevertheless, both agree well on the temperature dependence trend. Another study, by Fujii *et al.* [104], presented a microfabricated T-type nanosensor to measure the thermal conductivity of MWNTs. They obtained results from MWNTs with three different sizes: 1) outer diameter of 9.8 nm, inner diameter of 5.1 nm, length of 3700 nm; 2) outer diameter of 16.1 nm, inner diameter of 4.9 nm, length of 1890 nm; and 3) outer diameter of 28.2 nm, inner diameter of 4.2 nm, length of 3600 nm. Overall, their thermal conductivity estimates ranged from under 100 W/mK up to approximately 3000 W/mK, depending on geometry, temperature, and definition of cross-sectional area. Their MWNTs with comparable outer diameter to Kim *et al.* measured 30 to 50% lower at room temperature.

Shortly after Yu *et al.*'s publication, Pop *et al.* [105] also published a study on SWNT TC. They employed direct self-heating of a SWNT under high-bias current flow between 250 K and 400 K to obtain resistivity measurements. An inverse solver

was used to relate the resistivity to thermal conductivity values between 300 K and 800 K. Qualitatively, the results from Yu *et al.* and Pop *et al.* combine quite nicely and achieve good agreement with Kim *et al.* Another study, by Choi *et al.* [106], presented a novel four-point-probe third-harmonic method to estimate the thermal conductivity of an individual MWNT. They measured a value of 300 W/mK at room temperature, which is approximately an order of magnitude lower than the other studies. All five works agree on the temperature dependence trend (except Choi *et al.*, who only report a value at room temperature), but it is difficult to compare the results quantitatively. The chiralities (and diameters by extension) are all uncertain. Three reported MWNT measurements and the other two reported SWNT measurements. The CNT lengths vary from 1400 nm up to 3700 nm. Difficulty also arises due to differing experimental techniques, as the error and assumptions associated with each technique might not be comparable across studies. Without accurate knowledge of the chirality and geometrical conditions, it is very difficult to accurately scale thermal conductance measurements to tractable conductivity values. As suggested by the data, the TC and thermal conductance are functions of (but not limited to) chirality, diameter, length, number of CNT walls, and temperature. Even a direct comparison of thermal conductance values may be misleading if these factors are not all considered.

Hu *et al.* [107] and Akoshima *et al.* [108] measured CNT TC from bulk CNT samples. Hu *et al.* grew CNT samples on silicon chips using direct synthesis with



a trilayer catalyst configuration and microwave plasma enhanced chemical vapor deposition. The vertically oriented MWNTs were measured while still attached to the silicon substrate using the third-harmonic technique. This study produced an effective TC at 300 K of approximately 76 W/mK. The effective TC was defined as a volume-based weighted average of TCs of CNT and air.

Akoshima *et al.* used a different method to characterize the heat transfer in CNTs. They used a “supergrowth” water-assisted Chemical Vapor Deposition method to grow SWNT forests up to millimeter-length scales. Then the thermal diffusivity of the supergrowth forests was measured using a laser flash method. The laser flash method uses a laser to pulse-heat a sample, and subsequent heat diffusion is observed as a change in surface temperature on the rear face of the sample. The thermal conductivity can then be estimated using the diffusivity, specific heat capacity, and density. Akoshima *et al.* measured diffusivity of as-grown and solidified samples. The as-grown samples produced a TC of 1.9 W/mK. The solid samples, depending on density definitions, produced conductivities in a range from 38 W/mK to 2369 W/mK.

Alternatively, computer simulations can be useful to precisely control many factors. MD is utilized for this purpose and the high fidelity data that is available for more detailed investigations. Some of the drawbacks to MD include difficulty imposing boundary conditions exactly, finite size constraints, and a reliance on empirically fitted interatomic potentials. MD simulations integrate Newton’s equations of motion

for systems of atoms that interact via interatomic potentials. Atoms are modelled as point masses, and electrons are not explicitly modelled. Thermal transport in CNTs has however been shown to be dominated by phonon-phonon interactions in all temperature ranges of interest [20, 109, 110], so MD is an appropriate choice for modelling heat conduction in CNT systems. What follows is an overview of previous studies which employed MD simulations to model the TC of SWNTs.

Berber *et al.* [86] and Che *et al.* [90] were the first two groups to publish results from MD simulations, followed shortly by Osman and Srivastava [111]. All three groups used different numerical methods to compute TC. Che *et al.* used an EMD method which utilizes the Green-Kubo relations [112] in an equilibrium environment with no external fluxes imposed. All of their calculations were performed at 300 K. Osman and Srivastava used an NEMD method in which a temperature gradient is imposed, and the required heat flux to maintain that gradient is monitored. From Fourier's law, the quotient of these two quantities is the TC. Osman and Srivastava used nominal temperatures from 100 K to 500 K, with a temperature drop across the CNT of roughly 100 K. Berber *et al.* used a combination of the two techniques known as homogenous NEMD. They used a periodic system 2.5 nm in length, which is equivalent to 10 repeated CNT rings. Their simulations were performed at temperatures from 50 K up to 400 K. All three groups used the Tersoff interatomic potential [61, 62] with the Brenner parametrization [64]. CNT lengths were all under 50 nm, and all three groups used PBCs. These early works reported TC values on the order of  $10^3$

W/mK.

Since the previous three works all used PBCs, a potential concern arose due to residual stress in the CNT. PBCs restrict the dimensions of the system. Since the CNTs are typically initialized in pristine, equilibrium positions, thermalizing will cause the CNT to expand. In a constrained periodic system, the CNT will not be allowed to expand, and internal stresses will develop. Maruyama [88] and Moreland *et al.* [113] attempted to prevent these stresses from influencing their results. Maruyama modelled finite length CNTs with free boundaries. Moreland *et al.* ran initial simulations with free boundaries to find the natural length of the thermalized CNT, then ran NEMD simulations on a periodic system with the un-strained length imposed. They achieved a temperature gradient by applying thermostats to their source and sink regions such that the drop across the CNT would be 20 K. Maruyama simulated CNTs from 20 K up to 500 K, and Moreland *et al.* measured at nominal temperatures of 100 K, 290 K, and 400 K. Both studies were also computed with the Tersoff potential. Their results agree fairly well with one another in order of magnitude, although they are approximately one order of magnitude smaller than the earlier works. Maruyama reported a power law model with respect to CNT length, but did not achieve length convergence. Moreland *et al.* showed an increasing TC with length, with signs of a plateau beginning at 400 nm.

Padgett and Brenner [114] were the first to use the REBO potential [66], a second-generation Brenner potential, to model CNT thermal conductivity. Their goal in-

volved exploring the TC of CNTs with phenyl group sidewall functionalizations, but they also performed pristine CNT calculations for comparison. They used an NEMD method called the Müller-Plathe [77] method, which exchanges the smallest and largest velocities from the source and sink regions, respectively. The Müller-Plathe method is commonly used with PBCs. Their simulations were restricted to a nominal temperature of 300 K. Their results agree qualitatively well with Moreland *et al.* but observe values several hundred W/mK lower. Moreover, they begin to observe length convergence near 250 nm.

Lukes and Zhong [76] attempted a comprehensive study of CNT TC with MD, but restricted to length scales of less than 50 nm. They used the EMD method with the REBO potential and examined both free and periodic boundary conditions. They also applied a quantum correction, but this had only a small effect on room temperature cases. Their results show an increasing TC with increasing length, although they have not achieved length convergence since their longest CNT is 40 nm. They also measured at temperatures from 100 K to 500 K, and prior to applying the quantum correction, they observed a monotonically decreasing conductivity with respect to increasing temperature, which is notably different from Berber *et al.* and Osman and Srivastava, but similar to Maruyama. Their length dependence results are in good agreement with Padgett and Brenner.

Thomas *et al.* [52] used an NEMD method to study the effect of water inside CNTs, but the data presented here is from their control study of empty CNTs. Their NEMD

method scales the velocities in the source/sink regions to effectively impose a heat flux on the system. In a way, it is similar to the Müller-Plathe method since the heat flux is controlled rather than the temperature. This method was first proposed by Ikeshoji and Hafskjold [50]. They also used the REBO potential. Thomas *et al.* were interested in length convergence, so their CNT lengths are an order of magnitude longer than those of Lukes and Zhong. Their results indicate that (10,10) CNTs converge at a length of 400 nm, while smaller diameter CNTs take up to a micrometer to achieve length convergence. The results agree very well with Padgett and Brenner.

Mingo and Broido [115,116] and later Donadio and Galli [117] explored the length convergence of (10,0) CNTs. Mingo and Broido solved the linearized Boltzmann-Peierls (BP) phonon transport equation with an iterative method to evaluate the thermal conductance. The BP equation fully describes the interactions of phonon flow in solids. The interatomic potential proposed by Mahan and Jeon [118], which was constructed to reproduce quadratic phonon dispersions of the flexural modes, was used in their model. They found that the inclusion of second order 3-phonon processes causes the conductivity to reach a finite value at infinite lengths. The ballistic length scale was observed to be on the order of a few micrometers, depending on the temperature. At 316K, their CNTs reached convergence around  $10\text{-}10^2$  micrometers. They report an infinite-length TC of approximately 4000 W/mK, although they warn that the results should be viewed as only qualitatively correct. Donadio and Galli compared an EMD approach to the BP equation approach by Mingo and Broido.

The two approaches were shown to be in quantitative agreement with one another. Furthermore, they confirmed the finite TC for infinite-length CNTs, and reported a value of 7000 W/mK. They attribute the difference to the use of Tersoff as their interatomic potential. Their length convergence was observed around 20 nm, which is considerably shorter than most other works.

Table 4.1 : TC results from previous computer simulations of isolated SWNTs at or near 300 K.

	$\kappa$	CNT Length	Chirality
	(W/mK)	(nm)	
Berber <i>et al.</i> [86]	6600	2.5	(10, 10)
Che <i>et al.</i> [90]	2980	40	(10, 10)
Osman & Srivastava [111]	1700	30	(10, 10)
Maruyama [88]	210 – 560	10 – 400	(5, 5) – (10, 10)
Moreland <i>et al.</i> [113]	215 – 831	50 – 1000	(10, 10)
Padgett & Brenner [114]	40 – 320	20 – 310	(10, 10)
Lukes & Zhong [76]	15 – 140	5 – 40	(10, 10)
Thomas <i>et al.</i> [52]	250 – 430	200 – 1400	(6, 6) – (10, 10)
Mingo & Broido [115, 116]	50 – 4000	10 – $\infty$	(10, 0)
Donadio & Galli [117]	0 – 7500	0.5 – 200	(10, 0)

Figure 4.1 : A summary of TC measurements of (10,10) SWNTs in the literature. Blue markers denote MD simulations performed with the Tersoff potential. Red markers denote MD simulations performed with the REBO potential. Black markers indicate experimental measurements taken of SWNTs with unknown chiralities, i.e., not necessarily (10,10).

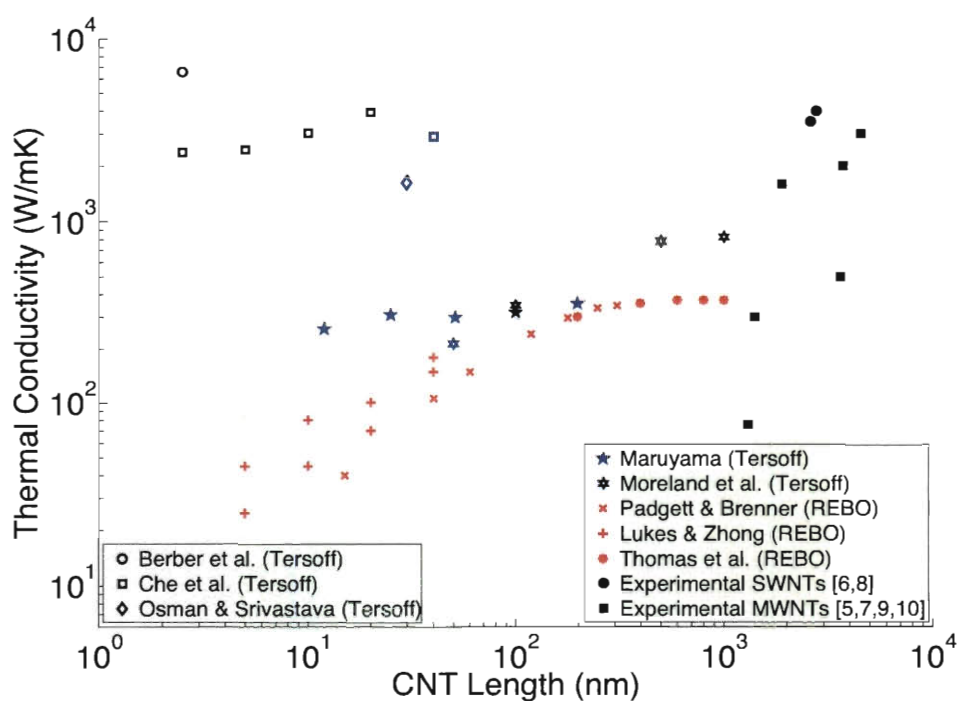


Table 4.1 lists the results at or near 300 K from several previous computer simulation studies of isolated SWNTs. A summary of these previous works is also presented in Figure 4.1 with respect to CNT length to better illustrate the spread. The MD data presented in Figure 4.1 is restricted to (10,10) CNTs at room temperature, although some experimental results with similar length scales but unknown chiralities are also presented for comparison purposes [102–107]. From this depiction, several observations can be made. First, as length increases, there is better agreement across MD simulations. Shorter CNTs, particularly with earlier studies, seem to yield a wide range of values from different sources. One possible cause is that the mean free path of phonons is much longer than the simulation domain at those length scales, and the phonons are interfering with their own periodic images. A second observation is that the studies computed with the REBO potential all appear to agree well with one another, and measure decidedly lower values compared to the Tersoff potential. Length convergence appears to be well agreed upon among the latter several studies. It is interesting to note that the Tersoff simulations that accounted for internal stresses measured considerably smaller values than those that did not, although this may just be coincidental. The REBO simulations seemingly did not reproduce this effect. The experimental results show a wide spread of conductivity values. In general, the comparison shows that the computational and experimental results span the same orders of magnitude. The discrepancies can be partially explained by the difference in length and the uncertainty of the chirality in the experimental cases.



The current work is aimed at characterizing TC sensitivities to various parameters to help put this observed spread in context. MD simulations are used so that physical and numerical parameters can be systematically altered, and highly detailed data can be analyzed by post processing. Section 4.2 discusses the methods used for computing the TC of the CNTs. Section 4.3 presents the TC results, and Section 4.4 explores further into the phonon DOS spectra for particular subsets of simulations. The conclusion is in Section 4.5.

## 4.2 Computational Details

MD simulations were performed with the LAMMPS software package [53] to discern the effect of physical and numerical variations on CNT TC in vacuum. The simulation domain consists of one individual finite-length SWNT. Different CNT types are tested without the use of PBCs. Two armchair-type CNTs, (6,6) and (10,10), and two zigzag-type CNTs (9,0) and (10,0), are simulated at lengths of approximately 25 nm, 100 nm, and 400 nm. Simulations are performed at a nominal temperature of 300 K, with a few tests at 200 K, 400 K, and 500 K to examine the sensitivity to temperature. Both Tersoff [61,62] and AIREBO [67] potentials are tested for the interactions in the CNT. The AIREBO potential is similar to the REBO potential, except it includes a term for longer range interactions. The end regions of the domains are specified for enforcing thermal boundary conditions. Two NEMD methods are utilized for creating a temperature gradient, which will be discussed later.

Equations of motion are integrated with the velocity-Verlet algorithm [57, 58]. A timestep of 0.5 femtoseconds (fs) is used. Linear and angular momentum of the CNT is removed every 0.05 picoseconds (ps) to ensure the CNT remains near the center of the simulation domain. Coordinates of the carbon atoms are initialized to a minimum potential energy state using a CNT generator algorithm from the Doren Research Group at the University of Delaware, TubeGen 3.2 [119]. The mass of the carbon atoms is assigned 12.0107 grams per mole. The initial velocities are assigned randomly from a Gaussian distribution. Equilibration is performed with a Nosé-Hoover thermostat [71, 72] at the target temperature with a damping parameter of 0.100 ps. This step is performed for 1000 ps, which was observed to be more than sufficient for these systems. Following equilibration, the system is released from the thermostat. A temperature gradient is created with one of two methods. The first method is sometimes referred to as the direct method. The second method is the one proposed by Ikeshoji and Hafskjold, and will be referred to as the Ikeshoji Method for simplicity.

In the direct method, Nosé-Hoover thermostats are applied to the source/sink regions to create a 20 K temperature drop across the CNT. This is a common technique, and has been utilized by some of the aforementioned groups [88, 111, 113], although the choice of thermostat may also vary. The target temperature of the thermostats are ramped over 250 ps until the target temperatures have a difference of 20 K. Then the thermostats work to hold those boundary conditions constant. In each timestep,

the thermostats report the amount of energy added or subtracted to the system to maintain the target temperature.

In the Ikeshoji Method, a steady heat flux is applied to the system. This was achieved by rescaling particle velocities in the source/sink boundary regions at every timestep. The same amount of energy is added to the source region as is subtracted from the sink region. An energy rate of 3 eV/ps is injected and removed from those regions. Since this rescaling process is not spectrally equivalent to a heat flux, the temperature in and near the boundary regions is expected to exhibit non-physical behavior. This is the same method that was utilized by Thomas *et al.*, and similar to the Müller-Plathe method used by Padgett and Brenner.

In both cases, there is a period of transience before a statistical steady state is achieved. This amount of time is determined by post processing. The remaining simulation data is time-averaged (and ensemble-averaged across five runs) for the average steady state behavior. A least squares fit is used to determine the slope of the temperature gradient. A direct application of Fourier's law gives a measure of the CNT's TC:

$$J_\mu = - \sum_\nu \kappa_{\mu\nu} \frac{\partial T}{\partial x_\nu}, \quad (4.1)$$

where  $J_\mu$  is a component of the thermal current in the  $\mu$  direction,  $\kappa_{\mu\nu}$  is an element of the thermal conductivity tensor, and  $\partial T/\partial x_\nu$  is the gradient of the temperature  $T$  in the  $\nu$  direction. In this case,  $\mu$  and  $\nu$  are the same direction, so only one of the diagonal components of the  $\kappa$  tensor is determined. The thermal current term is an

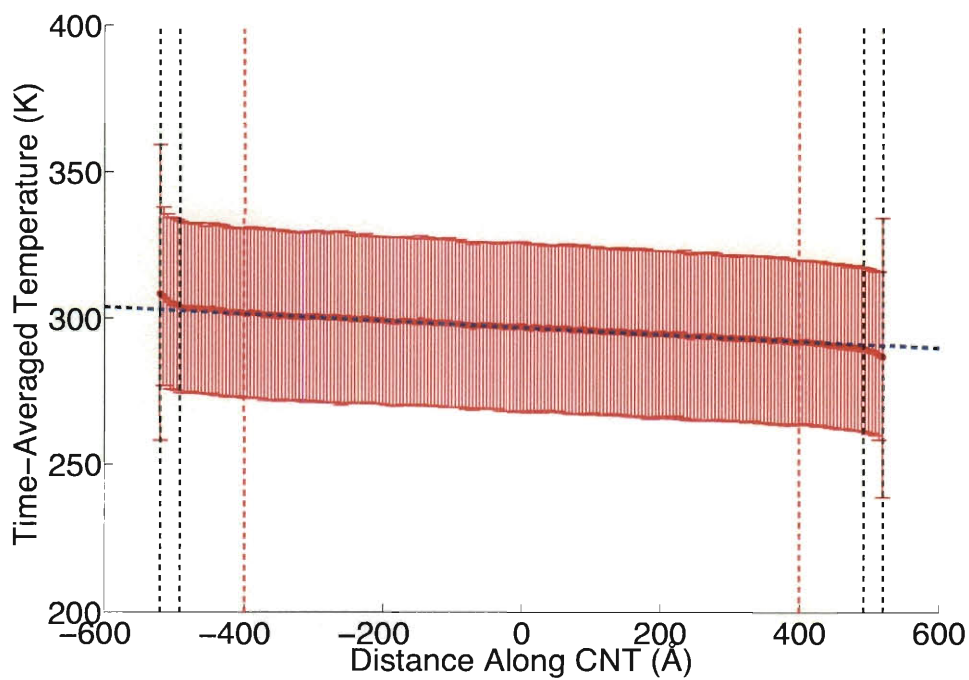
energy rate per area, where the area is the cross sectional area of the CNT. For this study, the area will be defined as

$$A \equiv \pi db, \quad (4.2)$$

where  $d$  is the non-thermalized diameter of the CNT (using a 1.42 Å bond length), and  $b$  is a van der Waals thickness of 3.4 Å.

Spatial dependent temperatures are extracted from the domain via the AtC interpolation method [55]. The resolution of the 1-D continuum mesh is approximately 10 to 15 Å. Temperature here is based purely on the kinetic energy contribution; mechanical vibration of the CNT is included in the temperature to capture the long wavelength motions. The temperature data is collected every 0.25 ps to facilitate post-processing. After removing the transient data, the remaining data is time-averaged and ensemble-averaged. Temperature data near the source/sink regions is disregarded for the line-fitting step. An example of the temperature gradient is shown in Figure 4.2. The source/sink regions are denoted by the black dotted lines and the line-fitting region is denoted by the red dotted lines. The error bars are the standard deviation of the temperature data. The uniformity of the error bars across the domain suggest that the error is only due to thermal fluctuations. The blue dotted line denotes the least squares linear fit. The fitted slope ultimately yields the TC of the CNT via Fourier's law.

Figure 4.2 : An example of the time-averaged temperature gradient of a CNT in vacuum simulation. Depicted here is a 100 nm (6,6) CNT at 300 K computed with the direct method using the Tersoff potential. Note the non-physical behavior at the ends of the CNT, and the monotonic trend throughout. A least-squares linear line is used to fit the data sufficiently far away from the source/sink regions.

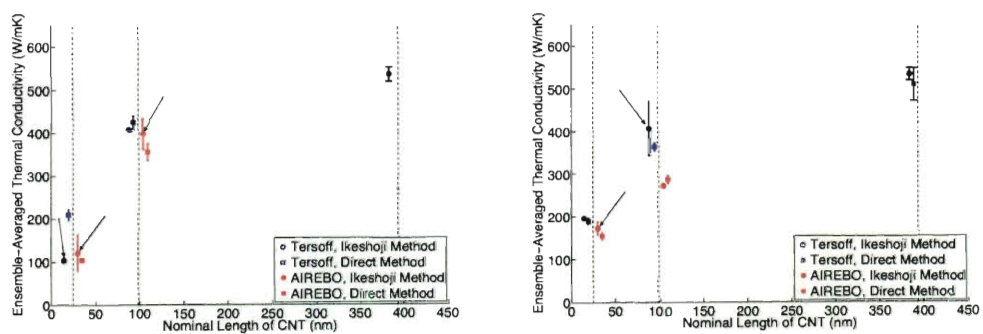


### 4.3 Results and Discussion

The TC results for the (10,10), (6,6), (10,0) and (9,0) CNTs at 300 K are plotted in Figures 4.3 (a), (b), (c), and (d), respectively. The plotted TCs are the ensemble-averaged mean. The results are plotted offset to the left and right of the nominal CNT length to help discern the data points. The nominal CNT lengths are denoted by the dashed lines. The error bars denote the standard deviation of the measurements from all ensemble observations. Qualitatively, the length and radius dependence is as expected. As the length increases, the thermal conductivity increases due to the increased accessibility to longer wavelength phonons. As the CNT approaches micrometer length scales, the thermal transport shifts from ballistic to diffusive, and the thermal conductivity is expected to level off [52]. The current data suggests agreement with this length convergence phenomenon, but it does not definitively show it since only three lengths were simulated.

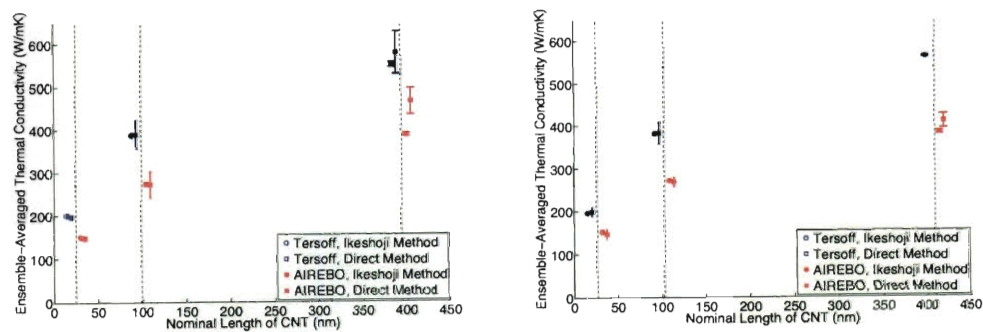
Figures 4.4 (a) and (b) depict the temperature dependent results from the Ikeshoji Method using the Tersoff potential for (10,10) and (9,0) CNTs, respectively. The different lengths are depicted with different colors. The TC is observed to decrease monotonically with respect to temperature for all length scales, but is increasingly noticeable with longer CNTs. This behavior is in good agreement with more recent works [76,88], particularly Lukes and Zhong before they applied a quantum correction. The quantum correction serves to reduce the TC at low temperatures, but for room temperature and above, Lukes and Zhong's results show marginal change. Aside from

Figure 4.3 : TC measurements of CNTs at various lengths with numerical variations for (a) (10,10), (b) (6,6), (c) (10,0), and (d) (9,0) chiralities. Measurements are plotted offset from nominal CNT lengths, which are denoted by the dashed lines. Arrows indicate particular simulation ensembles of which some or all produced oscillatory temperature gradients.



(a) (10,10) SWNTs

(b) (6,6) SWNTs

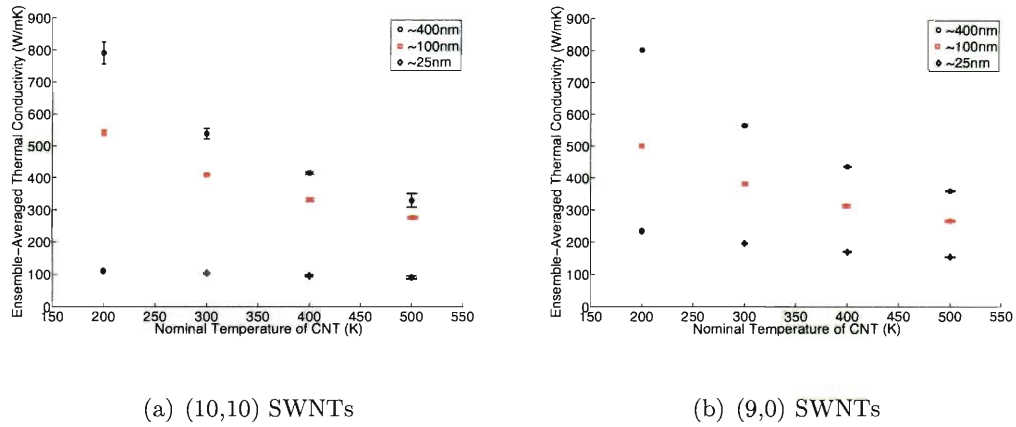


(c) (10,0) SWNTs

(d) (9,0) SWNTs

the low temperature behavior, as temperature increases, Umklapp processes reduce the phonon mean free path, and the thermal conductivity is expected to reduce as  $1/T^n$  where  $n$  is between 1 and 2 [88, 120, 121].

Figure 4.4 : TC measurements of CNTs at various temperatures using the Ikeshoji Method with the Tersoff potential for (a) (10,10) and (b) (9,0) chiralities. In agreement with the classical limit, TC decreases with increasing temperature due to Umklapp processes.

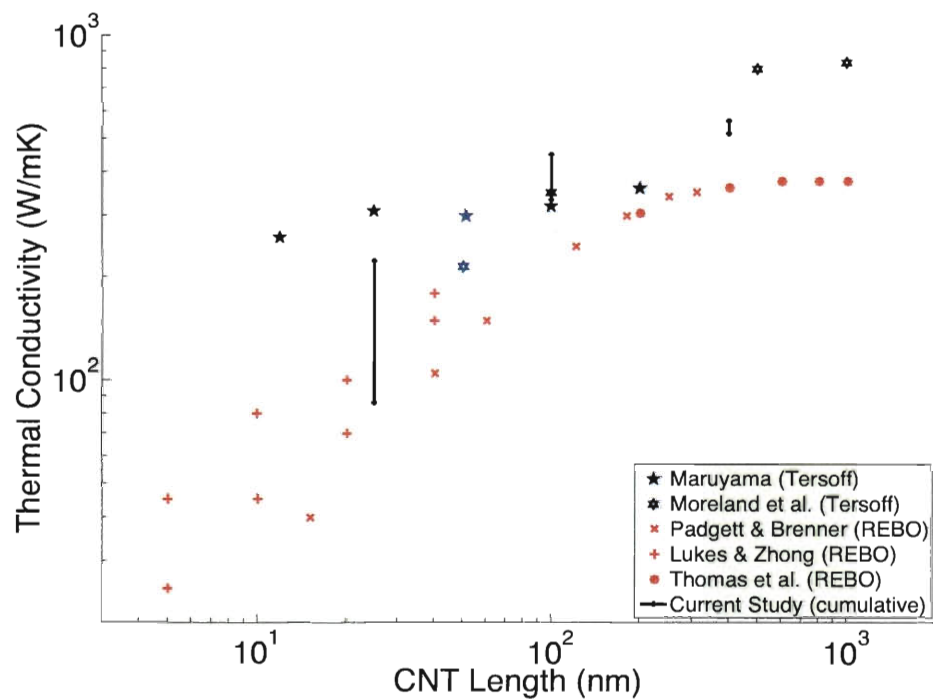


In general, the Tersoff potential yields higher TCs than the AIREBO potential. A similar observation has already been noted in discussing previous studies. The (6,6), (10,0), and (9,0) results strongly indicate that the difference increases as the length scale increases. The same could be said in comparing the more recent Tersoff studies [88, 113] to the previous REBO studies [52, 114]. Unfortunately, the (10,10) results from the current study are rather inconclusive on this topic, for reasons which will be discussed later. Figure 4.5 is a superposition of the uncertainty in the (10,10) CNT results from the current study onto Figure 4.1. The spread is depicted by the



minimum and maximum of all the (10,10) results, aggregated by length. The spread apparently is sufficient to account for much of the disagreement among previous studies.

Figure 4.5 : A superposition of the (10,10) CNT spread from the current study on Figure 4.1. The spread is denoted by the minimum to maximum of all the measurements, aggregated by length. The axes are zoomed relative to Figure 4.1 to highlight the general trend.

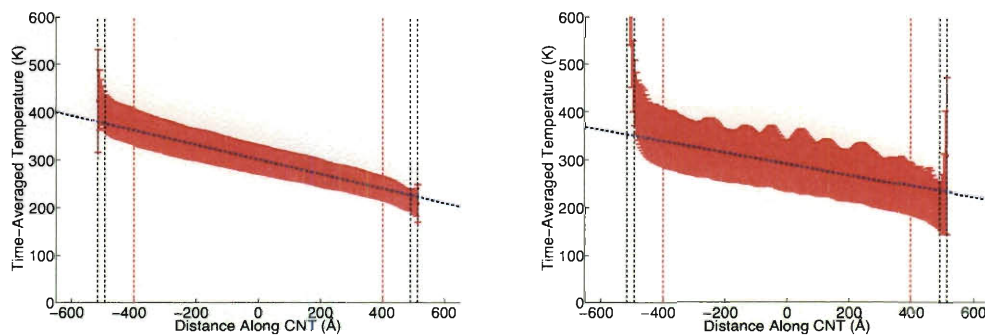


Most interestingly, the choice of NEMD method seems to play a significant yet inconsistent role. While most of the simulations performed with the Ikeshoji Method show close agreement with the direct method, there are a few select cases that stand out. In all cases where the two methods disagree, a closer look reveals that some of

the ensemble simulations produced quite different temperature gradients. An example temperature gradient from the direct method was shown in Figure 4.2. The analogous simulations using the Ikeshoji Method produced two markedly divergent temperature gradients from different replicate simulations, shown in Figures 4.6 (a) and (b). Figure 4.6 (a) depicts a relatively linear slope while Figure 4.6 (b) shows a rather oscillatory temperature gradient. When the simulations produce oscillatory gradients, the TC value is considerably different from the direct method, but usually in good agreement with one another. The simulations which resulted in smooth temperature gradients generally agree very well with the direct method, differing by less than 5 W/mK in most cases.

The ensemble of simulations of which some or all resulted in oscillatory temperature gradients is annotated in Figure 4.3. Notably this observation is never present in the (9,0) and (10,0) CNTs, and it seems to be more prevalent with the (10,10) CNTs than the (6,6) CNTs. Since the (10,10) cases are influenced by this phenomenon, it becomes rather difficult to assess the effect of interatomic potential on TC. More replicate simulations are required to determine the probability of its occurrence and its effect. This observation warrants a closer investigation into the phonon modes, presented in the next section. Another important comparison is that the direct method has greater control over the magnitude of the slope. Since the Ikeshoji Method only indirectly controls the slope (and since the TC value is not known *a priori*), the temperature drop can vary significantly.

Figure 4.6 : Two other examples of the time-averaged temperature gradient of a CNT in vacuum simulation. Both are from the same set of replicate simulations of a 100 nm (6,6) CNT at 300 K using the Ikeshoji Method with the Tersoff potential. (a) The temperature profile in this case is approximately linear within the line-fitting region. (b) The temperature profile here resembles a standing wave and has potential to significantly alter the measured TC. Note the difference in slopes relative to one another. Notice also that the Ikeshoji Method does not directly control the temperature gradient, and may result in much larger slopes compared to the direct method (see Figure 4.2).



(a) Smooth Temperature Gradient

(b) Oscillatory Temperature Gradient

The physical parameters (chirality, length, and temperature) all have reasonable effects on the CNT TC. For example, a (10,10) CNT at 200 K increases in TC by a factor of eight when the length is increased from 25 nm to 400 nm. Moreover, the 400 nm CNT conductivity decreases by a factor of two when heated to 500 K. While the range of values may be large in some cases, the trends agree well with theory and previous simulations. On the other hand, numerical variations were observed to significantly alter some results. In some cases, the Tersoff simulations are within 10 W/mK of their AIREBO analogues. In the other extreme, some analogous results differ by more than 100 W/mK. Similarly for the choice of NEMD method, some differ by less than 5 W/mK while others differ by over 100 W/mK. The variability observed due to numerical variations accounts for a significant amount of uncertainty across most MD simulation works.

#### 4.4 Phonon Density of States

Phonons are quantized lattice vibrations in solids that contribute to a material's TC. Most of the previous works which studied thermal transport in CNTs have examined the phonon density of states (DOS) [52, 76, 88, 114, 122]. The phonon DOS is a representation of the vibrational frequencies which exist in a given material. Sokhan *et al.* [122] first explored the CNT phonon spectra by examining CNTs of different chiralities at various temperatures, ranging from 300 K up to 1500 K. All the previous studies which presented phonon spectra have obtained their spectra from equilibrium

simulations. The first DOS comparison will feature two equilibrium simulations, but the latter comparisons will be computed from non-equilibrium computations. Since the phenomenon of interest happens only in a particular non-equilibrium setting, those DOS spectra must be calculated from those non-equilibrium conditions.

To obtain the phonon DOS, atomic velocities are output every 5 fs. The velocities are used to compute the velocity autocorrelation function (VAF). The Fourier transform of the VAF is the phonon DOS. The full phonon DOS is defined as

$$D_{full}(\omega) = \int_0^{\infty} dt \exp(2\pi i\omega t) \sum_j \frac{\langle \mathbf{v}^j(t) \cdot \mathbf{v}^j(0) \rangle}{\langle \mathbf{v}^j(0)^2 \rangle}, \quad (4.3)$$

where  $\mathbf{v}^j$  represents the velocity of the  $j$ -th atom, and the angle brackets denote an average over all atoms and all time windows. The longitudinal phonon DOS is then

$$D_{long}(\omega) = \int_0^{\infty} dt \exp(2\pi i\omega t) \sum_j \frac{\langle v_z^j(t) v_z^j(0) \rangle}{\langle \mathbf{v}^j(0)^2 \rangle}, \quad (4.4)$$

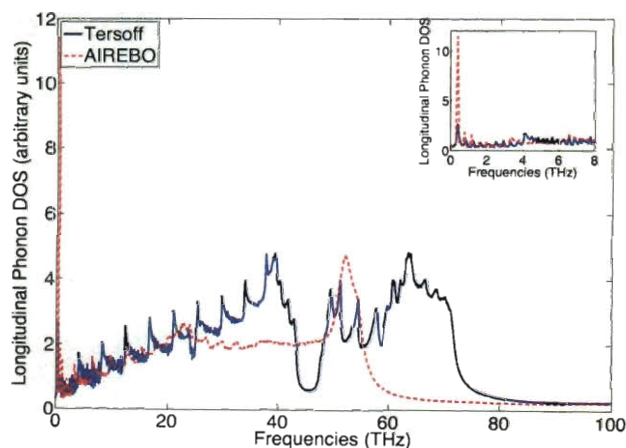
and the transversal phonon DOS is simply the difference of the two. Since there is an observation every 5 fs, the Nyquist frequency is 100 THz, or one half of the observation frequency. A new time origin for each VAF is taken every 2048 velocity outputs, giving a frequency resolution of roughly 0.1 THz.

For the first comparison, Figure 4.7 was generated from equilibrium simulations of CNTs. Depicted is a comparison between simulations with the Tersoff and AIREBO potentials. Both spectra were computed from 25 nm (10,10) CNT simulations at 300 K. There are some common traits between the two spectra, e.g., the cascading peaks in the low frequency longitudinal spectra. The low frequency cascade corresponds

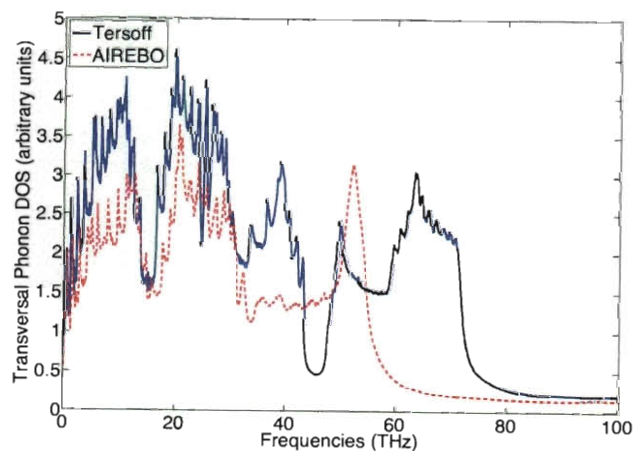
to acoustic phonon modes and, as discussed by others [52, 115, 116], contributes the most to the CNT TC. In general however, the two show quite different features, which probably attributes itself to the difference in TC. For example, the low frequency cascade in the longitudinal AIREBO spectra is nearly twice as compressed relative to the Tersoff spectra. Since those acoustic modes exist at a higher range of frequencies for Tersoff, perhaps this accounts for the larger TC measurements. Another observation is that both spectra have a strong low frequency first peak, but it is much more significant in the AIREBO spectra, as can be seen in the figure inset. Also, the AIREBO spectra, similar to the REBO spectra presented in other works [52, 76, 114], features a broad high frequency peak near 50 THz, but this peak is not observed in the Tersoff case.

Figure 4.8 depicts the longitudinal and transversal DOS of a 100 nm (6,6) CNT from different simulations using the Tersoff potential. The green line represents the CNT simulated with the direct method. The other two represent the two divergent results from the Ikeshoji Method. The blue spectra are computed from the simulations which produced smooth temperature gradients, whereas the red spectra are from the simulations which produced the oscillatory temperature gradients. The key difference in the spectra is the behavior at low frequencies, which is magnified in the figure insets. The Ikeshoji simulations apparently magnify the first three low frequency peaks, compared to the direct method. The oscillatory temperature gradient simulations in particular contribute significantly more energy to those peaks than the

Figure 4.7 : The (a) longitudinal and (b) transversal DOS of a 25 nm (10,10) CNT simulated in equilibrium conditions at 300 K. The blue spectra is computed with the Tersoff potential while the red spectra represents the AIREBO simulation. While a few features are similar, particularly in the range less than 30 THz, the two spectra contain decidedly different features. The inset in (a) shows the comparison at low frequencies.



(a) Longitudinal DOS spectra



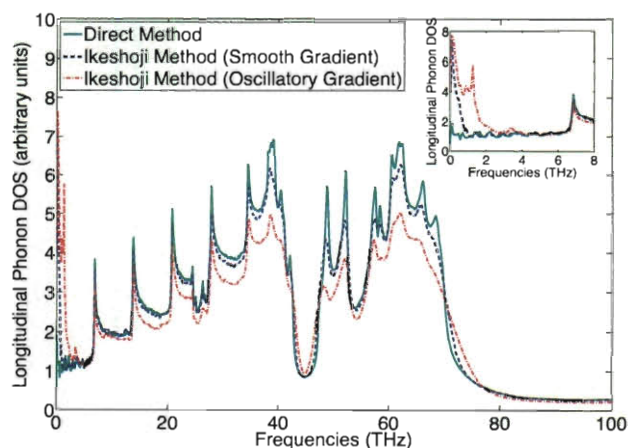
(b) Transversal DOS spectra

smooth gradient Ikeshoji simulations and the direct method. The three peaks occur at 0.1955 THz, 1.271 THz, and 3.421 THz and are present in both the longitudinal and transversal spectra. Presumably since the peaks are stronger in the transversal spectra, the modes are created as transverse waves but scatter to form analogous longitudinal waves.

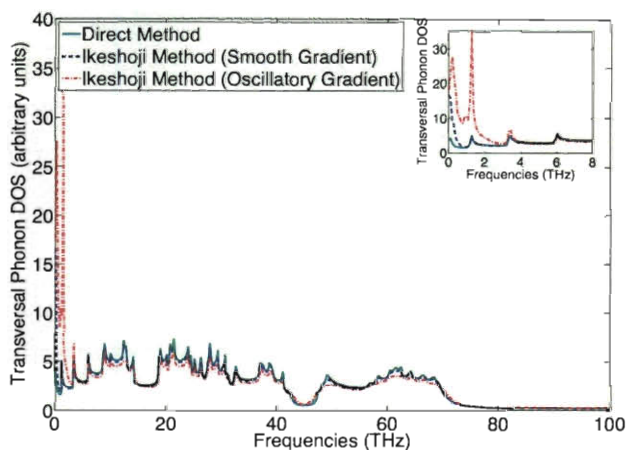
A similar observation was made in Lukes and Zhong's investigation in the effect of PBCs. In the absence of PBCs, they noted that a low frequency peak would appear. It is assumed that the first peak in the green spectra corresponds to the low frequency peak observed in Lukes and Zhong's free boundary cases. The Ikeshoji Method clearly enhances at least that first peak, and even more so in the cases resulting in oscillatory temperature gradients. Lukes and Zhong attribute the peak to boundary scattering from the free ends. Assuming these are indeed the same peaks, it makes sense that the Ikeshoji Method would enhance it relative the direct method. The direct method applies the Nosé-Hoover thermostat, so it is an ergodic influence on the system that depends on the difference in target and actual temperatures (which should be relatively small in general). On the other hand, the Ikeshoji Method rescales particle velocities regardless of the existing temperature. A phonon which enters the boundary region will be modified in both cases, but certainly the rescaling due to the Ikeshoji Method will be a more significant scatterer. It is worthwhile also to note that non-equilibrium simulations can produce comparable spectra to equilibrium simulations. Also interesting is the fact that the spectra reported by Lukes and Zhong



Figure 4.8 : The (a) longitudinal and (b) transversal DOS of a 100 nm (6,6) CNT simulated with the Tersoff potential using the direct and Ikeshoji methods. The green spectra come from the direct method simulations, and the Ikeshoji Method simulations is represented by the blue and red spectra. The blue spectra come from the replicate runs which produced the smooth temperature gradients, as seen in Fig. 4.2. The red spectra come from the replicate runs which produced the oscillatory temperature gradients, as seen in Fig. 4.6. The insets show the magnified the low frequency behavior. The Ikeshoji Method enhances the low frequency peaks, particularly in the oscillatory temperature gradient cases.



(a) Longitudinal DOS spectra

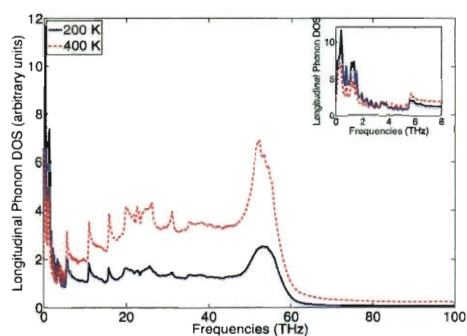


(b) Transversal DOS spectra

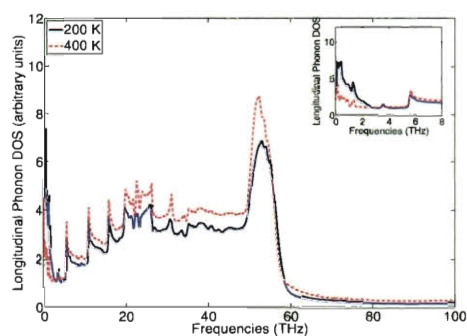
was computed from a REBO computation, whereas Figure 4.8 features a Tersoff simulation. The emergence of the low frequency peak with free boundaries seems consistent across interaction potentials.

Figure 4.9 shows a comparison of phonon DOS spectra from a variety of simulations with changes in only the physical parameters. All of these simulations are performed on an AIREBO (6,6) CNT with the Ikeshoji Method. The longitudinal spectra are the upper two figures, and the lower two are transversal spectra. 25 nm CNTs are shown on the left two figures; 100 nm CNTs are on the right. The blue spectra show simulations performed at 200 K, and the red spectra correspond to 400 K simulations. By definition, the area under the spectra curve is equal to the total number of accessible phonon modes. Particularly in Figure 4.9 (a), the 400 K spectra shows an increase in the overall number of modes, especially as the frequency increases. With less energy available to the system in the 200 K cases, the lower frequency modes are more easily populated, and this is certainly apparent in Figure 4.9(a). Since the higher frequency modes contribute less to the TC and serve to scatter the lower frequency modes, it is reasonable that the higher temperature TCs are lower. As the length increases, boundary scattering becomes less of a factor, and this is suggested by the smaller magnitude first peaks in Figures 4.9(b) and (d), relative to (a) and (c). Also important to note is that, aside from the first peak, the location of all the other peaks remains consistent as the length changes. This observation agrees with that of Lukes and Zhong.

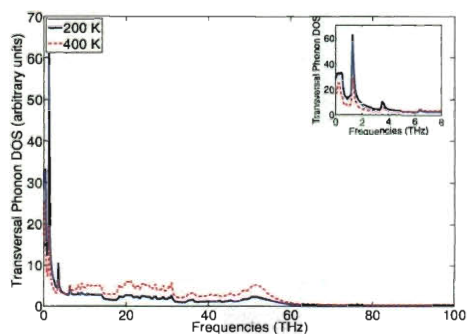
Figure 4.9 : A comparison of DOS spectra with variations in physical parameters. All DOS spectra are from (6,6) SWNT simulations using the AIREBO potential. The blue spectra denote simulations performed at 200 K, and the red spectra are from 400 K simulations. (a) and (b) are Longitudinal spectra of 25 nm and 100 nm long CNTs, respectively. (c) and (d) are the analogous Transversal spectra. Insets in all figures magnify the key differences.



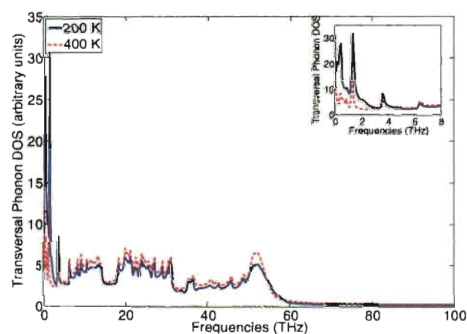
(a) 25 nm CNT, Longitudinal DOS spectra



(b) 100 nm CNT, Longitudinal DOS spectra

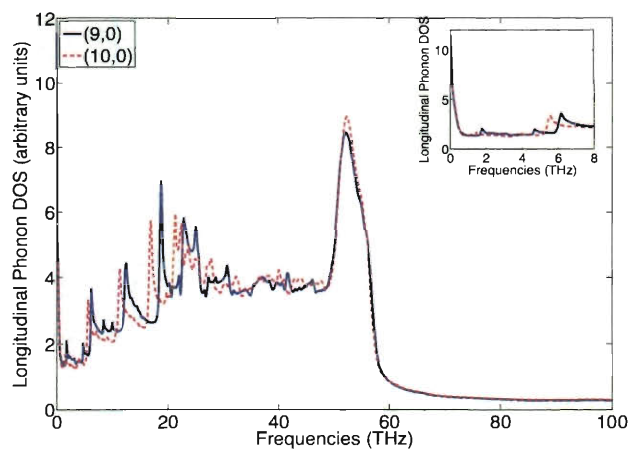


(c) 25 nm CNT, Transversal DOS spectra

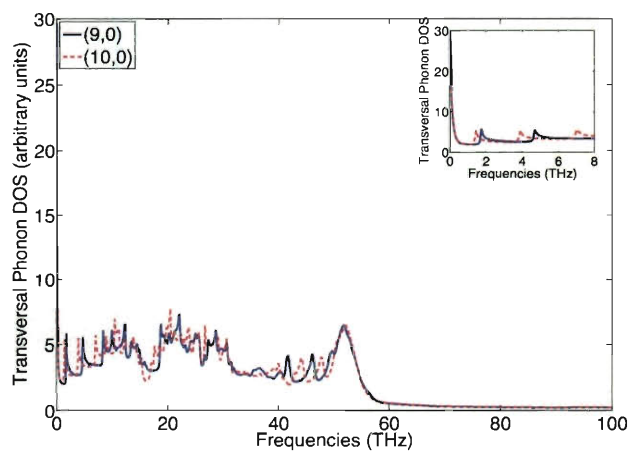


(d) 100 nm CNT, Transversal DOS spectra

Figure 4.10 : A comparison of DOS spectra with variations to zigzag-type chiralities. All spectra are from 300 K simulations using the AIREBO potential with the Ikeshoji Method. The blue spectra denote simulations of (9,0) CNTs, and the red spectra denote simulations of (10,0) CNTs. Both CNTs are approximately 400 nm in length. Comparisons between the chiralities are shown for (a) the Longitudinal spectra and (b) the Transversal spectra. Insets in all figures magnify some key differences.



(a) Longitudinal DOS spectra



(b) Transversal DOS spectra

Figure 4.10 shows the phonon DOS comparison between two SWNTs of different chirality. The (9,0) CNTs are shown in blue while the (10,0) CNTs are shown in red. Both CNTs are approximately 400 nm in length and performed at 300 K with the Ikeshoji Method using the AIREBO potential. The low frequency cascade is apparent in both, although the spacing between the peaks differs. In general, the two chiralities appear to exhibit many similar features, which probably explains the similarity in TC. The similarity in spectra is expected for MD simulations, particularly with two zigzag-type CNTs, because electronic properties and interactions are not included in this type of simulation; the spectra are driven by the mechanical response of the tube which is determined by the model of the interatomic potential. There is some evidence to suggest that the (9,0) metallic CNTs and (10,0) semiconducting CNTs should have somewhat differing phonon spectra due to electronic band structure effects peculiar to metallic nanotubes [123].

## 4.5 Conclusion

CNTs were modelled using molecular dynamics to understand the sensitivity of TC to various physical and numerical parameters. Simulations were performed without the use of PBCs. SWNT chiralities of (6,6), (10,10), and (9,0) were studied. Lengths were varied from 25 nm up to 400 nm; thermal conductivity was observed to increase monotonically with CNT length. The temperature dependence was observed to decrease monotonically as the temperature was varied from 200 K to 500 K. Phonon

spectra were used to support these dependencies on physical parameters. The quantum correction was not applied, although a previous study [76] indicates that the quantum correction serves to adjust measurements to more closely resemble theoretical and experimentally-observed trends. A comparison between the Tersoff and AIREBO interatomic potentials reveals that Tersoff predicts higher values of TC, and that the gap tends to widen as the length scale increases. The phonon spectra from the two potentials showed a few similar features, but overall they were disparate. The difference in the low-frequency cascade is a likely source for the higher measurements by Tersoff simulations. The AIREBO potential produced phonon spectra that closely resembled the spectra computed from the REBO potential by previous authors [52, 76, 114].

Lastly, two NEMD techniques for computing TC were examined. The direct method, which applies thermostats to end regions to enforce a specific temperature gradient, was compared against the Ikeshoji Method, which imposes a specific heat flux on the system and the resulting temperature gradient is monitored. The direct method produced generally very consistent results, whereas the Ikeshoji method resulted in two divergent outcomes. Some produced smooth, nearly linear temperature gradients which matched the direct method quite well. Others produced oscillatory temperature gradients which deviated by over 100 W/mK in some cases. The phonon DOS spectra revealed that the Ikeshoji Method enhances the low frequency response of the CNTs. Furthermore, the simulations which produced the oscillatory tempera-

ture gradients exaggerated the low frequency enhancement even further. The reason for this low frequency peak enhancement is unclear, although certainly provides a proximate cause for the change in temperature gradient. Moreover, it is difficult to actually determine which method produces the physically correct response. Aggregating the results further reveals that the numerical variations that were studied accounted for a significant portion of the spread previously observed in the literature.

## Chapter 5

### Solvated CNT

#### 5.1 Introduction

The most common theoretical framework used to understand the thermal conductivity enhancements due to CNT-nanofluids has been related to weighted averages and incremental improvements to the classical Maxwell model [3, 5–7, 28–31]. Another model, by Sastry *et al.* [124], uses a computational thermal resistor model to compute the effect of a percolating network of CNTs. These attempts are all non-atomistic in nature, and unfortunately, all exhibit a linear (or nearly linear) dependency on loading percentage. A number of theories in the past decade have been postulated, which include the effects of particle size/shape, particle motion, surface action, electrokinetic effects, liquid layering, and Brownian motion [1, 28, 29, 40–46]. Since these hypotheses are all atomistic-related, an atomistic simulation approach is suitable for this problem.

The first atomistic approach to simulating heat transfer in CNT-nanofluid systems was done by Huxtable *et al.* [47] with follow-up publications by Shenogin *et al.* [48, 49]. They used MD to simulate a SWNT immersed in an octane fluid. The octane was used to mimic the hydrophobic ends of a surfactant. PBCs were applied



to all sides of the simulated domain. (5,5) CNT lengths in [48] ranged from 12.2 Å to 87.0 Å. All interactions are modelled using the PCFF force field with the first- and second-order cross terms in the potential energy expression [125]. Two methods were used to extract the interfacial thermal conductance between the CNT and fluid. In the first method, the temperature of the CNT was instantaneously increased via velocity rescaling, and then the system was allowed to relax. In the second method, heat energy is constantly added to the CNT and removed at the same rate from a cylindrical shell near the outer boundary of the simulation domain, also via velocity rescaling. The temperature response of the surrounding fluid was monitored. This is similar to the Ikeshoji Method [50] described in the previous chapter, except with a cylindrical geometry. It was observed that most of the temperature drop occurs across the CNT-fluid interface. Huxtable *et al.* report a thermal interfacial conductance of approximately  $25 \text{ MW m}^{-1}\text{K}^{-2}$ . Shenogin *et al.* tested various CNT and domain sizes and reported boundary conductances ranging from 6.79 (for the smallest system) to approximately  $22 \text{ MW m}^{-1}\text{K}^{-2}$  (for the largest systems). These correspond to Kapitza resistances between  $4$  and  $15 \times 10^{-8} \text{ K m}^2\text{W}^{-1}$ . This suggests that the interface thermal resistance is the limiting factor in the effective TC of the composite system. Furthermore, they report that unless the surfactant is covalently bonded to the CNT, the interfacial resistance will be limited by the CNT's ability to transfer high-frequency phonon modes to low-frequency phonon modes where there is better coupling with the surrounding liquid.

Unnikrishnan *et al.* performed similar simulations with SWNTs and DWNTs in fully-periodic fluid domains. The CNT has a length of approximately 23.0 Å. The base fluid is varied between water-only and water with CuO additives. The methodology is the same as with Shenogin *et al.* They use the general-purpose Universal Force Field (UFF) for all atomic interactions [126,127]. UFF is a purely harmonic force field which includes van der Waals, bond stretch, bond angle bend, and torsional rotation terms. Interfacial resistance values between 1 and  $3 \times 10^{-8} \text{K m}^2 \text{W}^{-1}$  were reported for both SWNTs and DWNTs in pure water. The CuO additive marginally increases the interfacial thermal resistance. Various EMT models are applied, given the resistance values. The CNT conductivity was taken as 6000 W/mK, and 0.6 W/mK was taken for water. The Maxwell-Garnett-type model, modified by Nan *et al.*, under-predicts most experimental results.

Recently, Thomas *et al.* [52] also simulated heat transfer in a composite system with a CNT. They also used an MD approach, but simulated a water-filled SWNT (i.e., no surrounding liquid) to observe the influence of water in the tube axis. In this study, heat flow was simulated in the longitudinal direction by scaling the velocities in the end regions to effectively impose a heat flux. The resulting temperature gradient yields the TC via Fourier's law. This method is precisely the Ikeshoji Method. They observed that the addition of water inside the CNTs causes the critical length for fully diffusive heat transport to decrease, and thus exhibit a lower maximum TC. Furthermore, as the CNT radius decreases, the encased water becomes increasingly

structured, which has a more enhanced effect of disrupting and eliminating low frequency phonons in the CNT. As a result, they postulate that bulk-like water on the outside of a CNT will have a relatively small effect on the TC compared to the structured water inside the CNT.

The work presented in this chapter is aimed at understanding the cumulative effect of the solvent on the TC of an immersed CNT. MD simulations are used so that physical parameters can be systematically altered, and highly detailed data can be analyzed by post processing. Section 5.2 discusses the methods used for computing the TC of the CNTs. Section 5.3 presents the TC results, and Section 5.4 explores further into the phonon DOS spectra for particular subsets of simulations. The conclusion is in Section 5.6.

## 5.2 Computational Details

MD simulations were performed with the LAMMPS software package [53] to discern the effect of solvation on CNT thermal conductivity. To better understand the system dependencies, the CNT chirality and length are varied, as well as the size of the fluid box. Two armchair-type CNTs, (6,6) and (10,10), and one zigzag-type CNT, (9,0), are simulated at lengths of approximately 25 nm and 100 nm. Simulations are performed at a nominal temperature of 300 K. The AIREBO [67] potential is used to model the carbon-carbon interactions in the CNT. Fluid-fluid and fluid-solid interactions are modelled with the LJ potential; the parameters are listed in Table 5.1. The LJ

potential is given by

$$U^{ij}(r^{ij}) = 4\epsilon \left[ \left( \frac{\sigma}{r^{ij}} \right)^{12} - \left( \frac{\sigma}{r^{ij}} \right)^6 \right], \quad (5.1)$$

where  $U^{ij}$  is the potential energy of the interaction between the  $i^{th}$  and  $j^{th}$  atoms,  $r^{ij}$  is the distance between the atoms, and  $\epsilon$  and  $\sigma$  are numerical parameters [59]. The parameter  $\epsilon$  represents the energy of the potential well and  $\sigma$  is the (finite) distance at which the potential is zero. The fluid model parameters are based on the oxygen-oxygen potential in TIP3P water [99]. In other words, the hydrogen atoms are removed from the TIP3P model and the particle is electrically neutral. Two system domain configurations are simulated for the comparison, i.e., the CNT in vacuum and in an aqueous environment, although a third fluid-only system is also simulated as a control case. In all cases, equations of motion are integrated with the velocity-Verlet algorithm [57, 58]. A timestep of 0.5 fs is used. The mass of the carbon atoms is assigned 12.0107 grams per mole, and the fluid atoms are assigned 18.0154 grams per mole, the equivalent mass of one water molecule.

### 5.2.1 Initialization and Equilibration

#### CNT in Vacuum

One individual finite-length SWNT is simulated to model the CNT in vacuum case. In addition to the nominal lengths listed above, an extra five repeat rings are added to the ends of the CNT for enforcing thermal boundary conditions, which will be discussed in more detail later. Coordinates of the carbon atoms are initialized to

Table 5.1 : LJ interaction potential coefficients and reference for pairwise interactions. Carbon-carbon interactions are modelled with the AIREBO potential. The LJ 9-3 wall is described later and has a modified functional form from the usual LJ potential.

Species 1	Species 2	$\epsilon$ (eV)	$\sigma$ (Å)	Source
Fluid	Fluid	0.006596	3.150700	[99]
Fluid	CNT	0.004063	3.190000	[100]
LJ 9-3 Wall	Fluid	0.05	3.3	N/A

a minimum potential energy state using a CNT generator algorithm, TubeGen 3.2 [119]. The initial velocities are assigned randomly from a Gaussian temperature distribution. Equilibration is performed with a Nosé-Hoover thermostat [71, 72] at the target temperature with a damping parameter of 0.100 ps for at least 250 ps.

### CNT in Fluid

The CNT in an aqueous environment is simulated as immersed in a box of solvent fluid. In this case, the extra rings are not added since the thermal boundary conditions will be enforced on the fluid instead of directly on the CNT. This is notably different than the approaches by Shenogin *et al.*, Unnikrishnan *et al.*, and Thomas *et al.* Recall that Shenogin *et al.* utilized cylindrically-directed heating, thereby measuring the

sidewall interfacial resistance. The CNT conducts heat longitudinally, so longitudinal heating and tube-end interfacial resistance need to be explored as well. Both Shenogin *et al.* and Unnikrishnan *et al.* also simulated small CNTs with lengths ranging from 12.22 Å to 86.96 Å, and the system was modelled as fully periodic to simulate an infinite system. Thomas *et al.* lacked an external fluid and applied heat directly to the CNT. Applying the heat to the fluid rather than the CNT allows for measurement of the transfer of heat across interfaces. Moreover, Thomas *et al.* was measuring the altered CNT conductivity, whereas the current approach is aimed at measuring the composite fluid's conductivity.

After the CNT is constructed in its pristine form with TubeGen 3.2, the CNT is solvated by adding fluid atoms to randomly selected sites on a generated simple cubic lattice. The center of the CNT is also filled with fluid. Smaller CNTs are filled with a line of fluid atoms while the larger (10,10) CNT is filled with more atoms based on the bulk density of the fluid; again, the simple cubic lattice sites are used for this procedure. The simulation box width is set to approximately three times the diameter of the CNT, although one test case is performed with a significantly larger cross-section. The length is set to approximately 1.5 times the length of the CNT.

PBCs are used for the transverse directions, and LJ 9-3 walls bound the system in the longitudinal direction. The LJ 9-3 potential has the form

$$U^i = \epsilon \left[ \frac{2}{15} \left( \frac{\sigma}{r} \right)^9 - \left( \frac{\sigma}{r} \right)^3 \right]. \quad (5.2)$$

Table 5.1 also includes the parameters used for the LJ 9-3 wall. Those parameters are

obtained by integrating over a half lattice of fixed solid atoms and fitting the result to the above equation. The number of fluid atoms to populate the system is chosen such that the fluid density is approximately similar to water at standard temperature and pressure. Velocities of carbon atoms are initialized as before, but the fluid atoms are initialized with zero velocity. Equilibration is performed with separate Nosé-Hoover thermostats on the fluid and solid parts, followed by a period with a single Nosé-Hoover thermostat on the whole system. The system is equilibrated in the Canonical Ensemble for at least 250 ps, which was observed to be more than sufficient. Linear and angular momentum of the CNT is removed every 0.05 ps to ensure the CNT remains near the center of the simulation domain. Since removal of these momenta removes a portion of kinetic energy, the velocities of the carbon atoms are rescaled to match the original CNT kinetic energy. From an energy standpoint, the system remains unperturbed since both kinetic and potential energies are the same as prior to the momenta removal.

### 5.2.2 Generating the Temperature Gradient

Following equilibration, the system is released from the thermostat. A temperature gradient is created using the Ikeshoji Method. In the Ikeshoji Method, a steady heat flux is applied to the system. This is the same method that was utilized by Huxtable *et al.*, Shenogin *et al.*, and Thomas *et al.* According to the Ikeshoji Method, particle velocities in the source/sink boundary regions are rescaled at every timestep. In the

CNT in vacuum case, the source/sink regions are the extra repeat rings that are added to the ends of the CNT. For the CNT in fluid, the source/sink regions are a 5 nm long box extending from both ends of the fluid domain. The same amount of energy is added to the source region as is subtracted from the sink region. The energy rate varies for different systems in an attempt to keep the temperature gradient manageable relative to its mean. For most of the CNT in vacuum cases, 3 eV/ps is injected and removed from those regions. The energy rate is 0.1 eV/ps in the CNT in fluid cases. Since this rescaling process is not spectrally equivalent to a heat flux, the temperature in and near the boundary regions is expected to exhibit non-physical behavior.

There is a period of transience before a statistical steady state is achieved. This amount of time is determined by post processing. The remaining simulation data is time- and ensemble-averaged for the average steady state behavior. Each ensemble is run for several million timesteps (5 to 10 ns), and five ensembles are run for each configuration. The variation in total timesteps is due to availability of processors and amount of time required to converge a solution. A least squares fit is used to determine the slope of the temperature gradient. Direct application of Fourier's law gives a measure of the CNT's thermal conductivity:

$$J_{\mu} = - \sum_{\nu} \kappa_{\mu\nu} \frac{\partial T}{\partial x_{\nu}}, \quad (5.3)$$

where subscripts denote coordinate directions, as in Einstein vector notation,  $J$  is a component of the thermal current,  $\kappa$  is an element of the TC tensor, and  $\partial T/\partial x$  is



the gradient of the temperature  $T$  in the specified direction. In this case,  $\mu$  and  $\nu$  are the same direction, so only one of the diagonal components of the  $\kappa$  tensor is determined. The thermal current term is an energy rate per area, where the area is the cross sectional area of the applied heat flux. For the CNT in vacuum, the area will be defined as

$$A \equiv \pi db, \quad (5.4)$$

where  $d$  is the non-thermalized diameter of the CNT (using a 1.42 Å bond length), and  $b$  is a van der Waals thickness of 3.4 Å. Note that this definition is somewhat arbitrary, and in general, atomistic systems are better described by thermal conductance where the measure is independent of specimen size. For the fluid domain, the area is simply the cross-sectional area of the simulation box.

Spatially dependent temperatures are extracted from the domain via the AtC projection method onto finite element shape functions [55,128]. The resolution of the continuum mesh in the  $z$ -direction is approximately 5 Å. For the CNT, the mesh is one-dimensional since the temperature variation within each ring is assumed to be negligible at steady state. The fluid (if present) uses a three-dimensional mesh to detect any radial temperature gradients, particularly near the CNT. The  $xy$ -plane of the mesh has a resolution of approximately 3 Å, depending on the box size. In this work, temperature is based purely on the kinetic energy contribution; i.e., mechanical vibration of the CNT is not subtracted out of the temperature in order to capture the long wavelength motions. The temperature data is collected every 0.25 ps to facilitate

post-processing. After removing the transient data, the remaining data is time- and ensemble-averaged. Temperature data near the source/sink regions is disregarded for the line-fitting step.

### 5.3 Results - One-Dimensional Analysis

The results will be presented and discussed in separate subsections. First the simulations performed in vacuum will be presented, followed by the simulations from the aqueous environment. The results will subsequently be compared to one another.

#### 5.3.1 CNT in Vacuum

An example of the temperature gradient for the CNT in vacuum case is shown in Figure 5.1. The error bars are the standard deviation of the temperature data. The uniformity of the error bars across the domain suggest that the error is only due to thermal fluctuations. The blue dotted line denotes the least squares linear fit. The fitted slope ultimately yields the TC of the CNT via Fourier's law, Equation (5.3).

Figure 5.2 shows a summary of the thermal conductivity results for the (6,6), (10,10), and (9,0) CNTs at 300K. The results shown are the time- and ensemble-averaged TCs plotted as a function of CNT length. Selected cases which are repeated for aqueous environments are tabulated in Table 5.2. For a more detailed presentation and discussion of the CNT in vacuum results, refer to Chapter 4.

Figure 5.1 : An example of the time-averaged temperature gradient of a CNT in vacuum simulation. Depicted here is a 100 nm (6,6) CNT at 300 K. The source/sink regions are denoted by the black dotted lines and the line-fitting region is denoted by the red dotted lines. Note the non-physical behavior at the ends of the CNT, and the monotonic trend throughout. The least-squares linear line, depicted in blue, is fit the data sufficiently far away from the source/sink regions and used to compute an effective thermal conductivity of the unit cell.

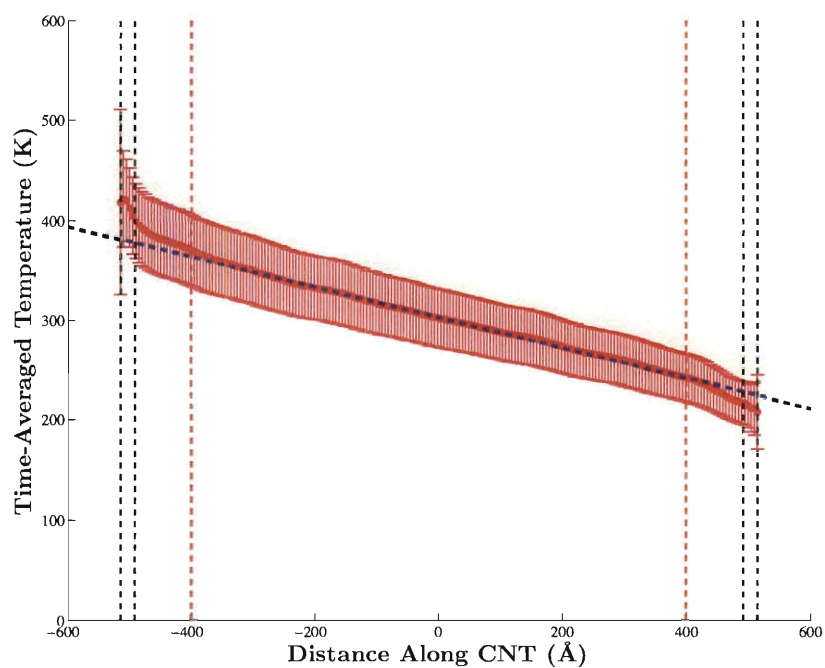


Figure 5.2 : TC measurements of CNTs with various lengths and chiralities. The chiralities are depicted with different colors. Simulations were performed at a nominal temperature of 300K using the Ikeshoji method. The AIREBO potential was used for carbon-to-carbon interactions.

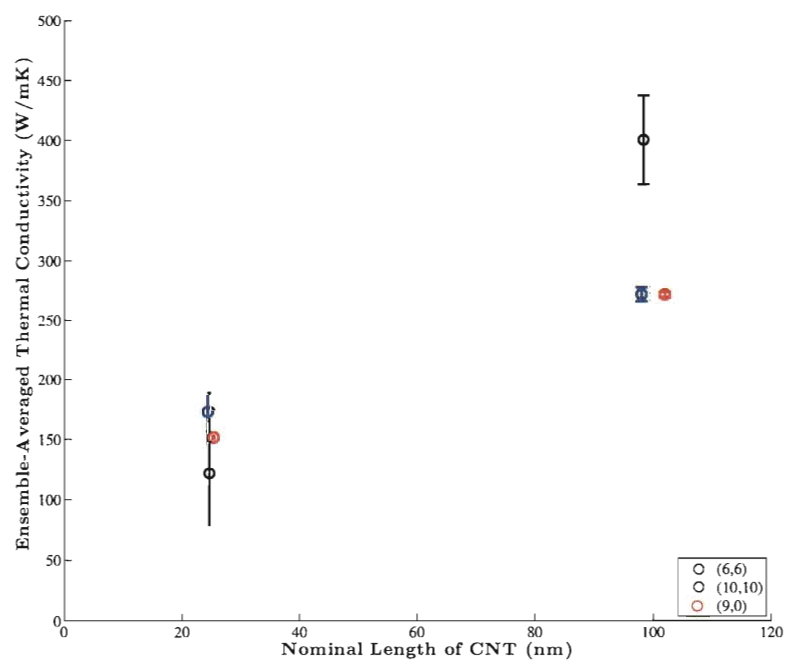


Table 5.2 : TC values of selected CNT in vacuum simulations at 300K.

Chirality	CNT Length (Å)	$\kappa_{vac}$ (W/mK)
(6,6)	245.95	173.27
(6,6)	983.80	272.75
(10,10)	245.95	121.74
(9,0)	255.60	152.22

### 5.3.2 CNT in Fluid

The CNT in fluid cases that were performed are tabulated in Table 5.3. The temperature of the two species can be described independently, and also as a system average. Using just a one-dimensional mesh produces a temperature gradient as shown in Figure 5.3. A least squares linear fit line can be used to approximate an effective system TC. While the fit line clearly does not reproduce the piecewise nature of the temperature profile, it still provides an approximation for a quantitative measurement of the TC enhancement. These enhancement measurements are presented in Table 5.4. The enhancement is defined as  $\frac{\kappa^{eff} - \kappa^{base}}{\kappa^{base}}$ . Note that one should be wary of directly comparing this enhancement with the macroscopic enhancement measured in experiments. Note also that the TCs are orders of magnitude smaller than the TC of a CNT in vacuum.

Figure 5.3 : An example of the time-averaged temperature gradient of a CNT in fluid simulation. Depicted here is a 25 nm (6,6) CNT initialized to 300 K. The red data points refer to the CNT temperature while the green data points indicate the fluid temperature. The system temperature is shown in black. Note the piecewise nature of the profile due to the presence of the CNT. A least-squares linear line is used to fit the data sufficiently far away from the source/sink regions. This particular example produces a TC of approximately 0.8692 W/mK, which corresponds to a 163.4% enhancement, relative to a base fluid conductivity of 0.33 W/mK. This enhancement does not directly correspond to macroscopic enhancements measured in experiments, but merely provides a measure for comparison.

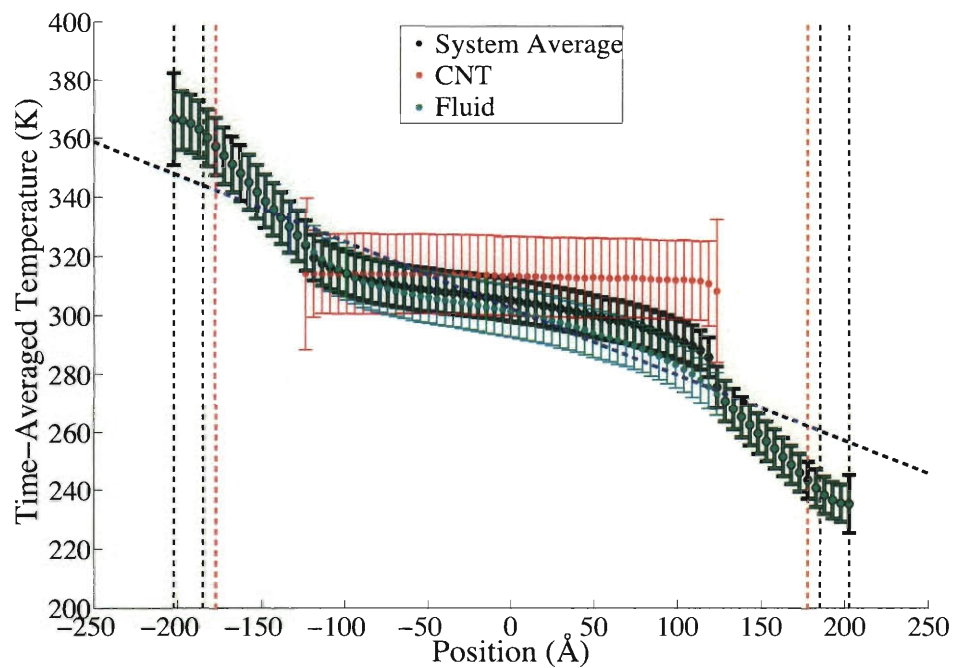


Table 5.3 : Cases of solvated CNT simulations performed.

Case #	Chirality	CNT Length (Å)	Box Dimensions (Å <sup>2</sup> × Å)	Vol. %	Heat Flux (W × 10 <sup>-8</sup> )
1	(6,6)	245.95	28.56 <sup>2</sup> × 400	6.55	1.602
2	(6,6)	245.95	60 <sup>2</sup> × 400	1.48	1.602
3	(6,6)	983.80	28.56 <sup>2</sup> × 1600	6.55	1.602
4	(10,10)	245.95	45 <sup>2</sup> × 400	4.40	1.602
5	(9,0)	255.60	28.56 <sup>2</sup> × 400	5.90	1.602

The results in Table 5.4 are applied to the HC model (Equation (1.5)) to approximate the volume concentration dependency of these nanofluid systems. The entire MD domain is treated as the embedded particle in the HC model, and the volume concentration is modified according to

$$\phi = \frac{V^{MD}}{V^f} \frac{V^s}{V^{MD}} = \frac{V^{MD}}{V^f} \phi^{MD}, \quad (5.5)$$

where the  $MD$  superscript denotes the MD simulation domain.  $\phi^{MD}$  is constant for each case, and is provided in Table 5.3. The volume fraction of the MD domain within the bulk nanofluid is given by  $V^{MD}/V^f$ , and is used as the volume fraction in the HC model. The corresponding  $\phi$  for the particle in the bulk nanofluid is the

Table 5.4 : TC enhancements of solvated CNT simulations assuming base fluid TC of 0.33 W/mK.

Case #	Chirality	CNT Length (Å)	Vol. %	$\kappa^{eff}$ (W/mK)	Enhancement (%)
1	(6,6)	245.95	6.55	0.8692	163.4
2	(6,6)	245.95	1.48	0.5637	70.8
3	(6,6)	983.80	6.55	2.4174	632.5
4	(10,10)	245.95	4.40	0.7692	133.1
5	(9,0)	255.60	5.90	0.8997	172.6

particle volume fraction. The trends are plotted in Figure 5.4 with the experimental results from Figure 1.1 overlaid. The order of magnitude is in good agreement with the experimental results, contrary to the earlier HC model. The trends still appear to be nonlinear in the regime of interest, however zooming out as in Figure 5.5 reveals the nonlinearity, particularly with Cases 2 and 3. These cases are highlighted in red particularly because they represent a more physically-motivated system.

Case 2 is a CNT in a larger fluid box, allowing the fluid to return closer to bulk conditions, i.e., the temperature gradient is less influenced by the CNT near the edges. The idea of using the HC model in this context is that the MD domain represents a



single particle which has no interfacial resistance with a bulk fluid. The more bulk-like the outer fluid is, the more reasonable this approach becomes. It is stated specifically by Maxwell [3] that the effects of different particles disturbing local currents should be independent of each other. Case 3 simulated a longer CNT of approximately 100 nm. The longer CNT allows more long wavelength phonons to exist, which are the primary carriers of heat in CNTs. The CNTs in most experimental results are on the order of hundreds to thousands of nm, so the 100 nm CNT is certainly closer to reality than the shorter 25 nm CNTs of the other cases. The combined effect of having a larger fluid domain and longer CNT may be sufficient to replicate the larger enhancements observed experimentally. However such a task is rather daunting considering the increase in computational cost.

The improvement to the model is two-fold. To understand the improvements, one must first simplify the functional form of the HC model. For  $\kappa^s \gg \kappa^f$  and small  $\phi$ , Equation (1.5) simplifies greatly to

$$\frac{\kappa^{eff}}{\kappa^f} \approx 1 + (n - 1)\phi. \quad (5.6)$$

In earlier publications,  $n$  was taken to be 6 for cylinders. However, based on the definition of sphericity, a value of 6 does not capture the large aspect ratio of typical CNTs. For 10% loading by volume,  $n = 6$  would indicate an approximate 5% enhancement. On the contrary, for a CNT with radius 10 Å and length 10,000 Å,  $n \approx 47$  and the enhancement is approximately 46%.

Secondly, by using the MD domain as the suspended particle, nonlinearity is re-

introduced to the HC model. Recall that one of the assumptions of the original Maxwell model was that there is no temperature drop across the interface. It is well known that a temperature drop does exist across a material interface. Physically, the surrounding fluid in the atomistic simulation provides a natural interface to the bulk fluid. As the fluid buffer increases in size, there are fewer fringe effects from radially varying thermal currents. As the temperature gradient in the outer fluid returns to the bulk temperature gradient, Maxwell's first condition becomes more valid. Mathematically,  $\kappa^s \gg \kappa^f$  is no longer true because  $\kappa^s$  is taken to be the conductivity of the entire MD domain. The aforementioned simplifications are no longer valid, and the denominator terms become more relevant. This has the direct effect of making the trend nonlinear.

## 5.4 Results - Phonon Analysis

In this section, the phonon DOS will be analyzed to discern deviations in the frequency spectra from the in-vacuum simulations. Phonons are quantized lattice vibrations in solids that contribute to a material's TC. Most of the previous works which studied thermal transport in CNTs have examined the phonon DOS [52, 76, 88, 114, 122]. The phonon DOS is a representation of the vibrational frequencies which exist in a given material. To obtain the phonon DOS, atomic velocities are output every 5 fs. The velocities are used to compute the VAF. The Fourier transform of the VAF is the

Figure 5.4 : HC model applied to enhancement results from MD simulation cases. The experimental data from Figure 1.1 is overlaid. The model still suggests a roughly linear trend in the region of interest, however the model produces values that are on a similar order of magnitude as the experimental data. Cases 2 and 3 are highlighted in red because they both represent more physically-motivated examples than the rest.

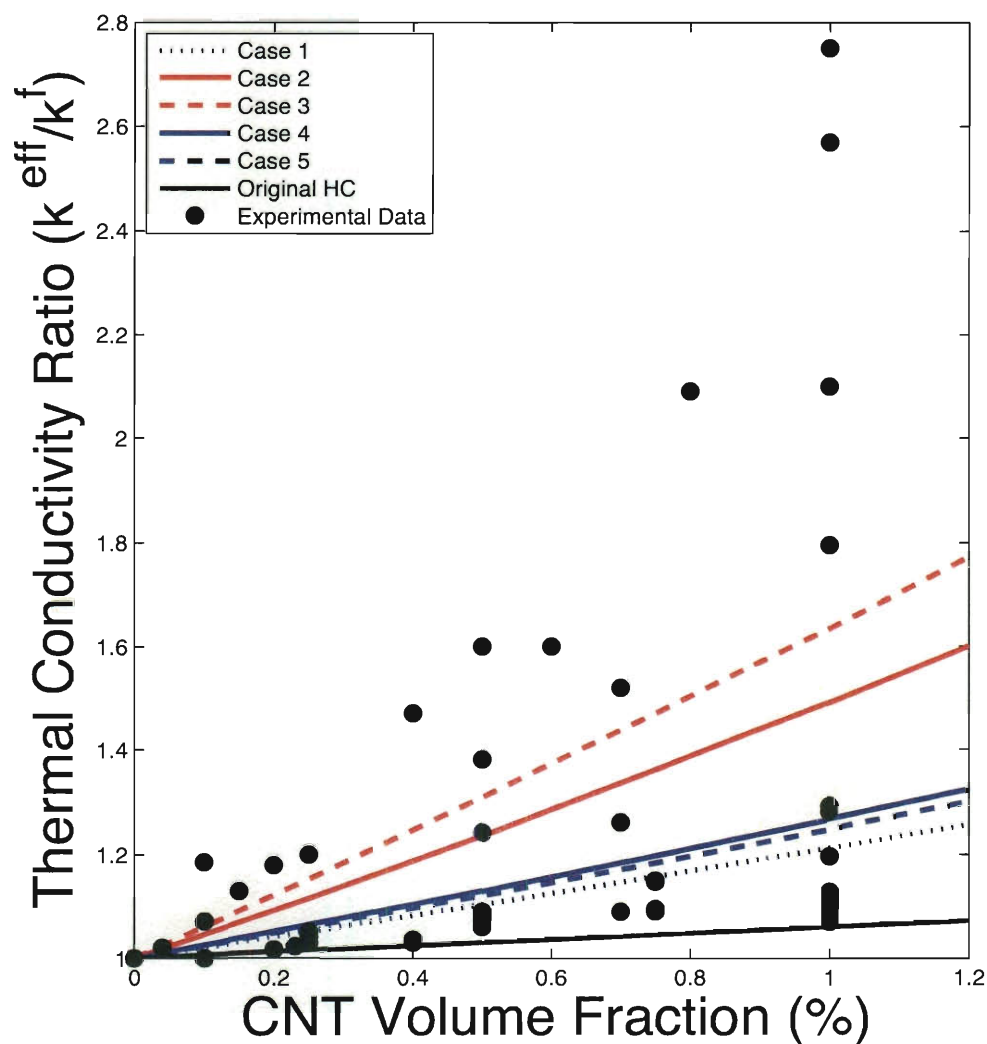
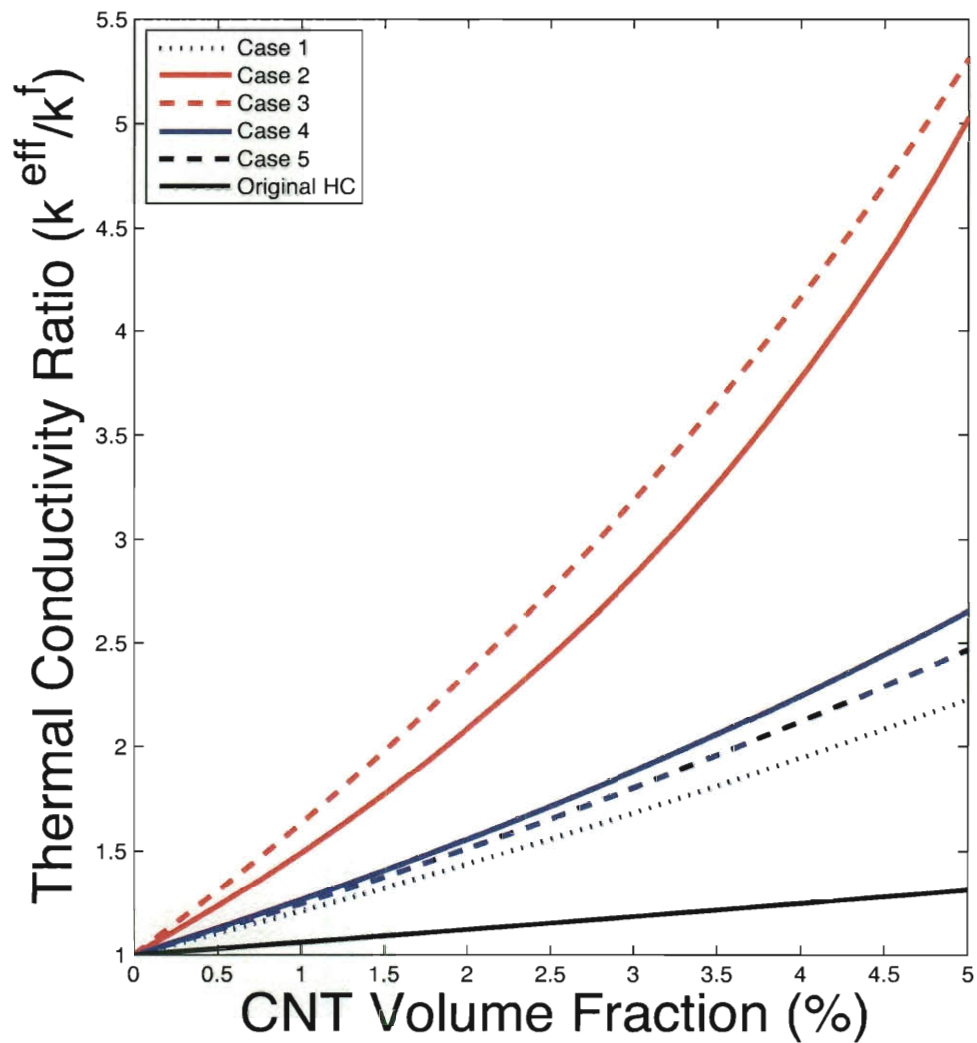


Figure 5.5 : The same data as presented in Figure 5.4 without the experimental data. The axes are zoomed out to display more concentrated loading percentages and the emergence of nonlinearity. The nonlinearity becomes particularly apparent with Cases 2 and 3.



phonon DOS. The full phonon DOS is defined as

$$D_{full}(\omega) = \int_0^\infty dt \exp(2\pi i\omega t) \sum_j \frac{\langle \mathbf{v}^j(t) \cdot \mathbf{v}^j(0) \rangle}{\langle \mathbf{v}^j(0)^2 \rangle}, \quad (5.7)$$

where  $\mathbf{v}^j$  represents the velocity of the  $j$ -th atom, and the angle brackets denote an average over all atoms and all time windows. The longitudinal phonon DOS is then

$$D_{long}(\omega) = \int_0^\infty dt \exp(2\pi i\omega t) \sum_j \frac{\langle v_z^j(t) v_z^j(0) \rangle}{\langle \mathbf{v}^j(0)^2 \rangle}, \quad (5.8)$$

and the transversal phonon DOS is simply the difference of the two. Since there is an observation every 5 fs, the Nyquist frequency is 100 THz. A new time origin for each VAF is taken every 2048 velocity outputs, giving a frequency resolution of roughly 0.1 THz.

Comparisons of the phonon spectra from the in-vacuum and solvated cases are shown in Figures 5.6 and 5.7. The vacuum spectra is shown in blue while the aqueous spectra is shown in red. Both longitudinal and transversal spectra are shown in the figures. Figure 5.6 features a comparison with an unsolvated CNT which experiences an applied  $4.806 \times 10^{-7}$  W heat flux via the Ikeshoji Method. On the other hand, the unsolvated CNT featured in Figure 5.7 is simulated under equilibrium conditions. The spectra from both in-vacuum and in-fluid simulations share the same features, i.e., the low-frequency cascade and the broad peak near 50 THz. There is a slight blueshift in the location of the peaks, and the large 50 THz peak is narrowed. The most notable difference is the first low frequency peak in the vacuum simulation which has no corresponding peak in the solvated case. The peak is particularly noticeable

in Figure 5.6b. The low frequency cascade corresponds to acoustic phonon modes, and as discussed by others [52, 115, 116], contributes the most to the CNT TC. In the CNT in vacuum cases, the height of the first low frequency peak indicates a large contribution to the TC. Since this peak is not present in the CNT in fluid cases, it is a strong indication for why the solvated CNT has a reduced TC.

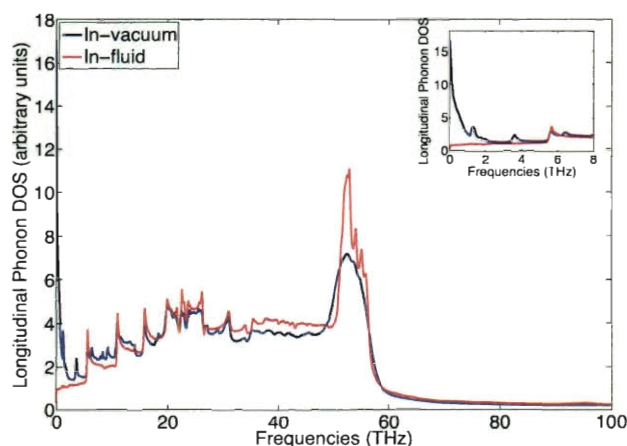
## 5.5 Results - Irving-Kirkwood-based Analysis

For a more in-depth investigation, the spatially dependent heat flux is also measured during the simulation. The heat flux density is measured on a per-atom basis using an extension of the Irving-Kirkwood formalism [129]. The original formalism expresses the atomic heat flux density as:

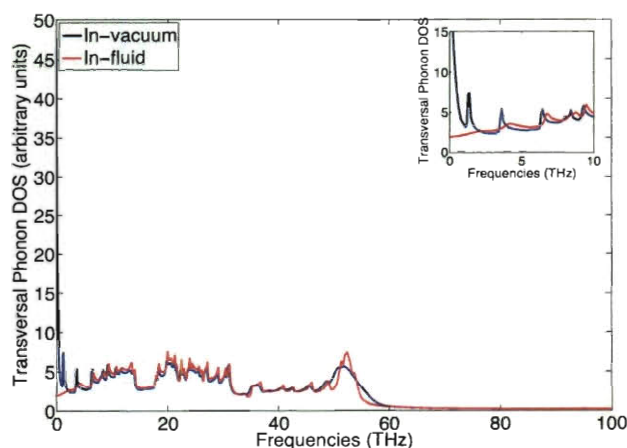
$$\mathbf{J}^i = \frac{1}{\mathcal{V}} \left[ E^i \mathbf{v}^i + \sum_{j \neq i} \left( \frac{1}{2} \mathbf{F}^{ij} \cdot \mathbf{v}^i \right) \mathbf{x}^{ij} \right], \quad (5.9)$$

where superscript indices denote atoms,  $\mathbf{J}^i$  is the heat flux density vector for atom  $i$ ,  $E^i$  is the total energy of atom  $i$ , i.e., kinetic energy plus the contribution from potential energy of interaction between atom  $i$  and all neighboring atoms,  $\mathbf{v}^i$  is the velocity of atom  $i$ ,  $\mathbf{F}^{ij}$  is the force exerted on atom  $i$  from atom  $j$ , and  $\mathbf{x}^{ij}$  is the vector pointing to atom  $i$  from atom  $j$ . The first term represents the convection of energy of atom  $i$ . The second term is the virial contribution associated with atomistic interactions. The volume,  $\mathcal{V}$ , is not initially included in the per-atom calculation. Note that this version of the formulation only applies to pairwise interactions. Expanding the energy to its

Figure 5.6 : The (a) longitudinal and (b) transversal DOS of a 100 nm (6,6) CNT simulated at 300 K. The blue spectra is from the CNT in vacuum simulations while the red spectra is the corresponding solvated case. The CNT in vacuum case presented here was subjected to a  $4.806 \times 10^{-7}$  W heat flux using the Ikeshoji Method. While the overall features remain the same, the low frequency peaks are highly attenuated in the solvated case. The inset shows the comparison at low frequencies. A distinct feature of the vacuum simulation is a large first peak below 1 THz. The aqueous simulation specifically does not share this feature. The large peak near 50 THz is narrowed and most features appear to be blueshifted and smoothed.

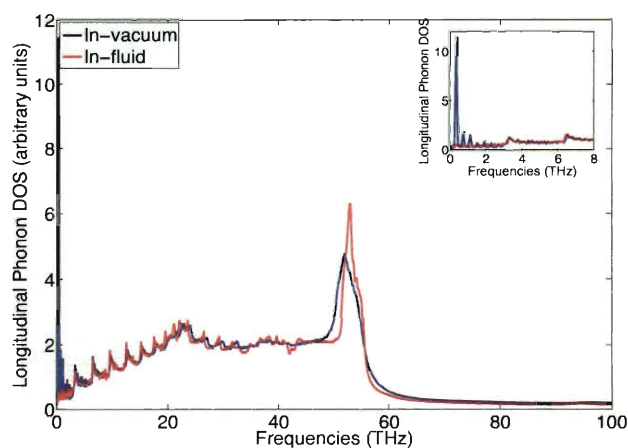


(a) Longitudinal DOS spectra

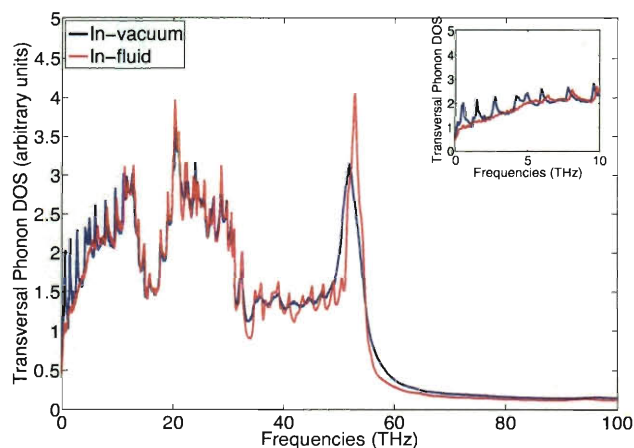


(b) Transversal DOS spectra

Figure 5.7 : The (a) longitudinal and (b) transversal DOS of a 25 nm (10,10) CNT simulated at 300 K. The blue spectra is from the CNT in vacuum simulations while the red spectra is the corresponding solvated case. The CNT in vacuum case presented here was simulated in an equilibrium environment with no applied fluxes. The comparison is very similar to Figure 5.6. Most features appear in both spectra, except the low frequency peaks are noticeably washed out in the aqueous simulations. The in-fluid peaks in general are also blueshifted.



(a) Longitudinal DOS spectra



(b) Transversal DOS spectra



potential and kinetic components gives

$$\mathbf{J}^i = \frac{1}{V} \left[ K^i \mathbf{v}^i + \frac{1}{2} \sum_{j \neq i} (P^{ij} \mathbf{v}^i + (\mathbf{F}^{ij} \cdot \mathbf{v}^i) \mathbf{x}^{ij}) \right], \quad (5.10)$$

where  $K$  is the kinetic energy and  $P$  is the potential energy. Note that the kinetic energy contribution is added once and is directly associated with the  $i$ -th atom. On the other hand, the potential energy contribution is summed over all atoms  $j \neq i$  and is partitioned amongst all atoms creating the potential. In this case, it is partitioned between two atoms due to the assumption that all interactions are pairwise.

For a fluid-solid composite material, there are solid atoms  $s \in \mathcal{S}$  and fluid atoms  $f \in \mathcal{F}$ .  $\mathcal{S}$  is the set of all solid atoms, and  $\mathcal{F}$  is the set of all fluid atoms. There are three conductivity/resistance values that are of interest. First is the TC of the fluid. Second is the TC of the solid. Third is the interfacial thermal resistance between the fluid and solid, or the Kapitza resistance. All three of these values depend on the heat flux within this material. The  $zz$ -component of the TC of the fluid based on Fourier's law is given by

$$\kappa_{zz}^f = -\frac{J_z^{ff}}{\partial T^f / \partial z}, \quad (5.11)$$

where  $J_z^{ff}$  is the  $z$ -component of the heat flux density from fluid to fluid, and  $\partial T^f / \partial z$  is the  $z$ -component of the temperature gradient in the fluid. The other diagonal components and the TC of the solid can be defined in the same fashion. The Kapitza resistance [36] is defined as

$$R_K = \frac{T^s - T^f}{(J_n^{sf} + J_n^{fs}) / 2}, \quad (5.12)$$

where  $J_n^{sf}$  is the normal component of the heat flux density vector from solid to fluid. Note that the solid-fluid and fluid-solid contributions are both included because they both represent the heat transfer at the interface. Therefore, the heat flux densities  $\mathbf{J}^{ff}$ ,  $\mathbf{J}^{ss}$ ,  $\mathbf{J}^{fs}$ , and  $\mathbf{J}^{sf}$  all need to be evaluated.

Recall that there is a constant thermal current,  $\mathbf{J}^{app} = J_z^{app} \hat{\mathbf{z}}$ , applied to the system. For a given plane normal to the  $z$ -direction, one can express the applied heat flux density as a summation of components:

$$J_z^{app} = J_z^f + J_z^s, \quad (5.13)$$

where

$$J_z^f \equiv J_z^{ff} + J_z^{fs}; \quad (5.14)$$

$$J_z^s \equiv J_z^{ss} + J_z^{sf}. \quad (5.15)$$

The applied thermal current is expanded fully as

$$J_z^{app} = J_z^{ff} + J_z^{fs} + J_z^{ss} + J_z^{sf}. \quad (5.16)$$

For the  $i$ -th atom, the heat flux density is given by Equation (5.10). For the arbitrary  $i$ - $j$  pair of atoms, the definition becomes unclear. Certainly the indices can be specified to be of particular atom types, but as noted above, the kinetic energy term cannot be directly associated with more than one atom. For instance, if one were to assign the definitions

$$\mathbf{J}^{ij} = \begin{cases} \frac{1}{V} \left[ K^i \mathbf{v}^i + \frac{1}{2} \sum_{j \neq i} (P^{ij} \mathbf{v}^i + (\mathbf{F}^{ij} \cdot \mathbf{v}^i) \mathbf{x}^{ij}) \right], & i, j \in \mathcal{F}, \\ \frac{1}{V} \left[ K^i \mathbf{v}^i + \frac{1}{2} \sum_{j \in \mathcal{S}} (P^{ij} \mathbf{v}^i + (\mathbf{F}^{ij} \cdot \mathbf{v}^i) \mathbf{x}^{ij}) \right], & i \in \mathcal{F}, j \in \mathcal{S}, \end{cases} \quad (5.17)$$

there would be a conflict since the kinetic energy term appears in both and would then be double-counted. Note that by observation, in general  $J_z^{fs} \neq J_z^{sf}$  due to the asymmetrical inclusion of the atomic velocity  $\mathbf{v}^i$ . So Equation (5.16) cannot be simplified.

Therefore, it seems reasonable that one assigns the kinetic energy term to just one of the heat fluxes, say the fluid-fluid heat flux to maintain a sense of convection specific to the fluid material. Then by extension, it is reasonable that the potential energy term is also transferred in whole to the fluid-fluid heat flux, since originally in Equation (5.9), the term was written as a convection of the total energy. Note that as convective quantities associated with atom  $i$ , it is natural that they would stay within the same medium as atom  $i$ .

The issue becomes particularly important because when pairwise interactions are not used in parts of the simulation, one or more of the component heat fluxes cannot be determined directly. In the present case, all of the interactions are pairwise except for the solid-solid interactions. The fluid-fluid, fluid-solid, and solid-fluid heat fluxes need to be determined in order to extract the solid-solid contribution indirectly.

The contributions are therefore expressed as:

$$\mathbf{J}^{ij} = \begin{cases} \frac{1}{V} \left[ K^i \mathbf{v}^i + \frac{1}{2} \sum_{k \neq i} P^{ik} \mathbf{v}^i + \frac{1}{2} \sum_{j \neq i} (\mathbf{F}^{ij} \cdot \mathbf{v}^i) \mathbf{x}^{ij} \right], & i, j \in \mathcal{F}, k \in \mathcal{F} \cup \mathcal{S} \\ \frac{1}{2V} \left[ \sum_{j \in \mathcal{S}} (\mathbf{F}^{ij} \cdot \mathbf{v}^i) \mathbf{x}^{ij} \right], & i \in \mathcal{F}, j \in \mathcal{S} \\ \frac{1}{2V} \left[ \sum_{j \in \mathcal{F}} (\mathbf{F}^{ij} \cdot \mathbf{v}^i) \mathbf{x}^{ij} \right], & i \in \mathcal{S}, j \in \mathcal{F}. \end{cases} \quad (5.18)$$

Notice in the fluid-fluid heat flux density, the potential energy is summed over all atoms  $k$ . There is no restriction on atom type for  $k$  since it is the total potential energy that is partitioned to atom  $i$ , contrary to how the virial term is computed. These contributions are applied to the simulations to extract heat flux densities for all pairwise interactions, i.e., fluid-fluid and fluid-solid. The solid-solid heat flux can later be inferred by conservation arguments, via

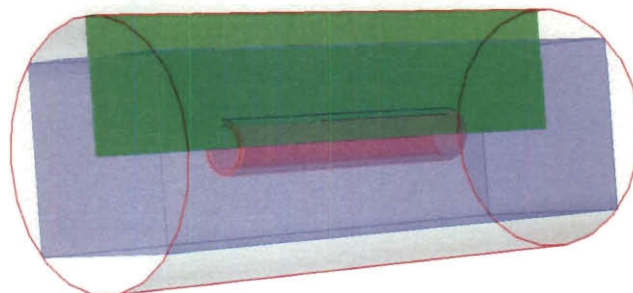
$$Q_z^{ss} = Q_z^{pp} - Q_z^{ff} - Q_z^{fs} - Q_z^{sf}, \quad (5.19)$$

where  $\mathbf{Q}^{ij} \equiv \mathbf{J}^{ij} \times A$  is the heat flux vector ( $A$  is the cross-sectional area). The heat flux density vector is projected onto the three-dimensional AtC mesh discussed previously, normalizing the projected nodal heat flux density vector by the volume associated with the projection operator. See Reference [55] for more details.

Heat flux density data is time- and ensemble-averaged, then converted from Cartesian vectors to cylindrical vectors, i.e., flux densities in the  $x$ - and  $y$ -directions are dotted with the position vector to form radial flux densities. The radial flux density at  $r = 0$  is taken to be the magnitude of the vector sum of the  $x$ -flux density and  $y$ -flux density values in order to avoid dotting with a zero-vector; this is done to obtain a measure of the amount of radial-flux at  $r = 0$ , although it is not directly equivalent to the radial-flux. The data is then interpolated from the Cartesian nodes onto concentric cylinders at specific measurement sites. The number of sites on each cylinder increases linearly with the radius; the number is comparable to the number of Cartesian nodes nearest to the cylinder. For each radius and  $z$ -plane, a value is

spatially averaged. This process essentially produces a cylindrical average of the 3D heat flux density data. Figure 5.8 shows a diagram of this process. The outer **cylinder** depicts the cylindrical averaging over all  $\theta$  and collapsed onto the green plane. The green plane is a representation of the spatial field presented in the following mappings.

Figure 5.8 : A diagram of the domain where the blue box and red tube represent the fluid box and CNT, respectively. The diagram is not drawn to scale. The cylinder shows data is averaged over  $\theta$  and collapsed onto the green plane. The green plane is the area shown in each of the subsequent mappings.



Figures 5.9 and 5.10 show an example of the heat flux density output for a CNT in fluid simulation. Figure 5.9 shows the  $z$ -component of the heat flux density while Figure 5.10 shows the  $r$ -component, with a positive-outward sign convention. The top-most mappings on both figures show the fluid-fluid interaction and the bottom two mappings show the fluid-solid and solid-fluid heat flux densities. A dotted line is drawn to indicate the approximate location of the CNT sidewall. The longitudinal heat flux density through the CNT, computed by conservation of energy arguments, is plotted in the overlaid horizontal bar in the top-most mapping in Figure 5.9. Note that there is no carbon-to-carbon interaction in the radial direction. The colorbar

scales in general are different for each mapping, but the color denoting zero remains consistent for easy comparison.

Figure 5.9 : An example of the time-averaged longitudinal heat flux density of a CNT in fluid simulation. Depicted here is a 25 nm (6,6) CNT, Case 1 from Table 5.3. The top-most plot shows the fluid-fluid heat flux density with the solid-solid heat flux density overlaid using a different scale. The other two plots show the fluid-solid and solid-fluid heat flux densities. The longitudinal components of the heat flux density vector show boundary conditions accurately persisting through the fluid until the CNT disrupts the “bulk” behavior. The CNT carries much of the heat transport load, particularly closer to the center.

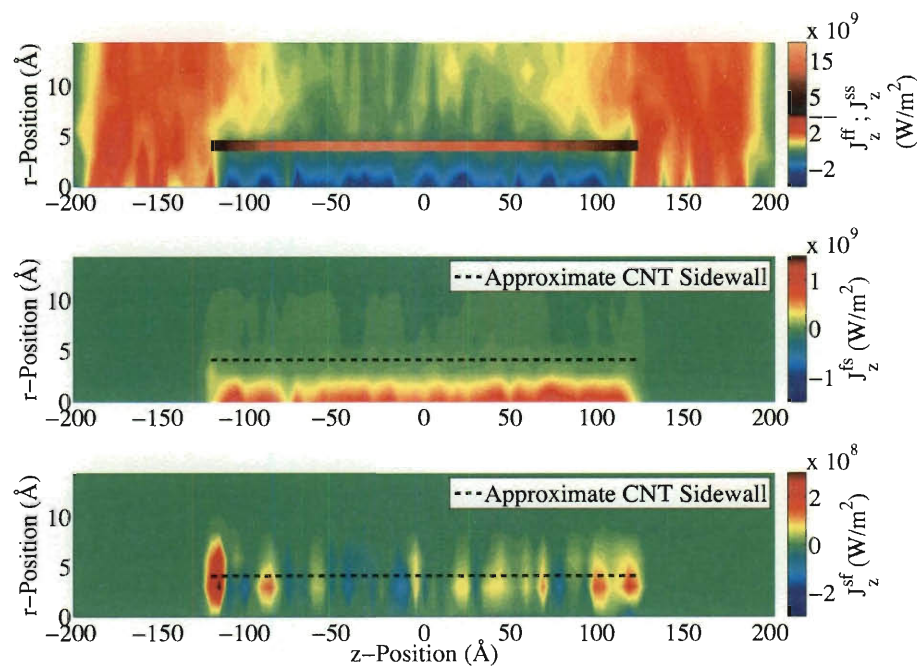
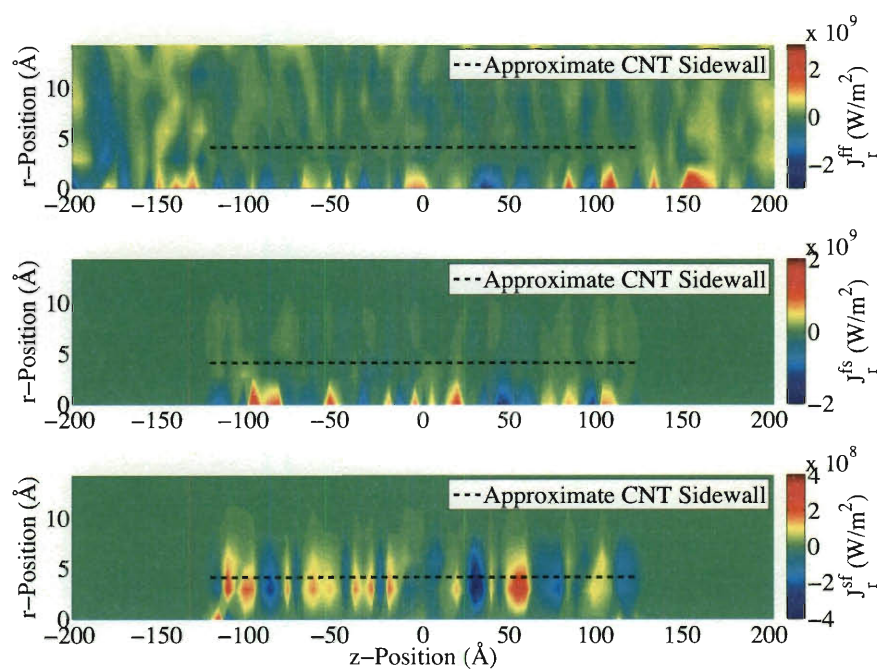


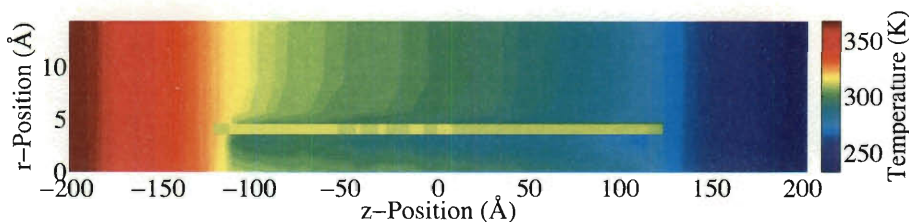
Figure 5.11 shows the temperature distribution in the domain, using the same averaging scheme as with the flux mappings. One can clearly note that most of the temperature gradient exists in the fluid and that there is relatively no temperature

Figure 5.10 : An example of the time-averaged radial heat flux density of a CNT in fluid simulation. Depicted here is a 25 nm (6,6) CNT, Case 1 from Table 5.3. The top-most plot shows the fluid-fluid heat flux density. The other two plots show the fluid-solid and solid-fluid heat flux densities. The radial components of the heat flux density vector show relatively zero heat flux radially except at the solid-fluid interface.



gradient within the CNT. This is consistent with Figure 5.3. It is also notable that the temperature gradient in the fluid directly surrounding the CNT is significantly diminished because most of the heat in this region is traveling through the CNT.

Figure 5.11 : The temperature distribution from the 25 nm (6,6) CNT example above. Most of the temperature gradient exists in the fluid due to the lower thermal conductivity of the fluid. In the region near the CNT, the temperature gradient is diminished due to heat being primarily transported through the highly conducting CNT.

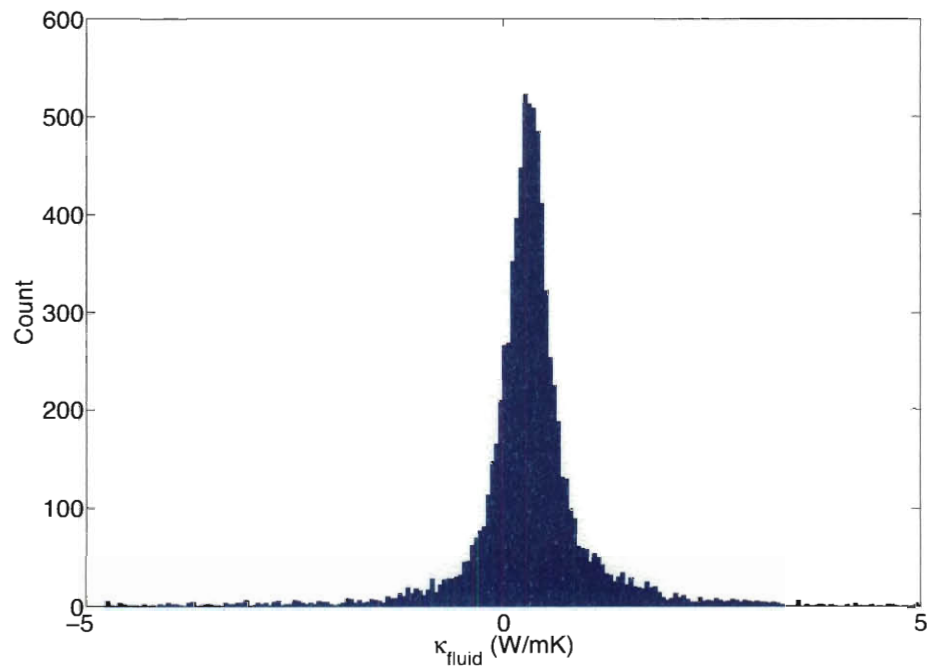


The TC of the base fluid is evaluated at all Cartesian mesh nodes according to Equation (5.11). The computed values are shown in a histogram in Figure 5.12 with outliers truncated. Similarly, the Kapitza resistance is computed at all Cartesian mesh nodes. To compute the Kapitza resistance, Equation (5.12) is utilized with a slight modification. Both radial and longitudinal Kapitza resistance values are measured.  $J_r^{fs}$  is used for the radial heat flux density across the sidewall interface; moreover, values are only computed for nodes external to the CNT. The reasoning for this is two-fold: 1)  $J_r^{fs}$  inside the CNT is poorly defined since it is computed indirectly via Cartesian coordinates, thus any finite radial flux is not accurately portrayed for  $r = 0$ ;



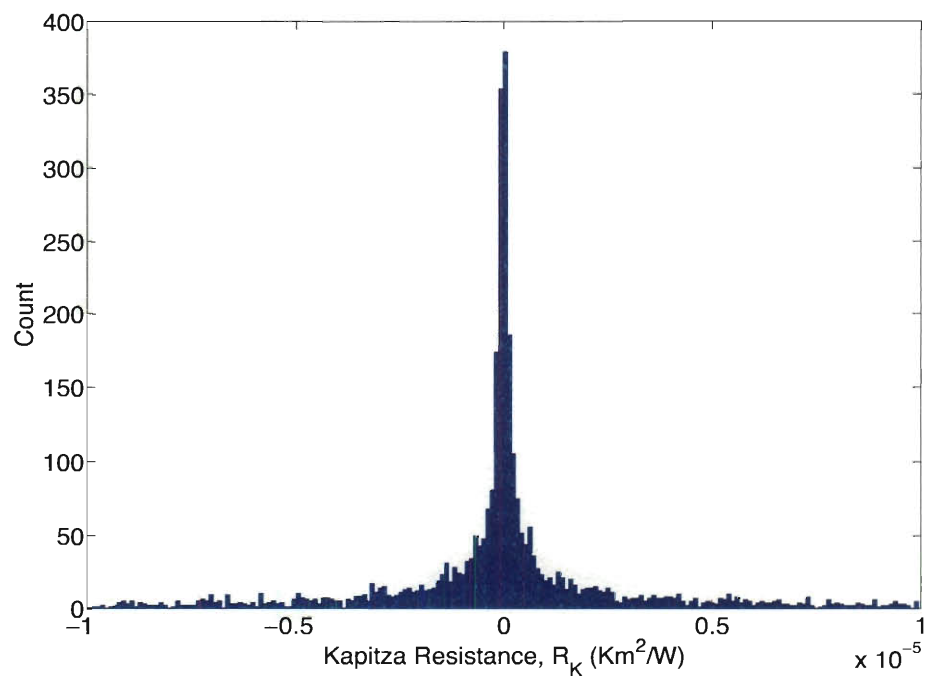
2)  $J_r^{sf}$  is the net effect from fluid inside and outside the CNT, so it actually represents two interfaces simultaneously and cannot be decomposed into distinct contributions. The computed radial resistance values are also presented in a histogram in Figure 5.13.

Figure 5.12 : The distribution of computed TC values for the base fluid according to Equation (5.11). The distribution presented is evaluated from the Case 1 data presented in the above figures. Outlier values are truncated, and the mean value is 0.3247 W/mK.



For the longitudinal Kapitza resistance, the interfacial heat flux density is taken to be  $(J_z^{fs} + J_z^{sf}) / 2$ . The heat flux density is summed over the center-most subset of nodes. The fluid-solid flux density is summed over the finite element plane that is one

Figure 5.13 : The distribution of computed Kapitza resistance values for the interfacial boundary according to Equation (5.12) with slight modifications specified in the text. The distribution presented is evaluated from the Case 1 data presented in the above figures. Outlier values are truncated, and the mean value is  $1.36 \times 10^{-8} \text{ Km}^2/\text{W}$ . This value agrees in order of magnitude with results from Shenogin *et al.*



plane away from the CNT end. The solid-fluid flux density is taken at the CNT end. The density is multiplied by the surface area of the 25 nodes; then it is divided by the surface area of the CNT, given by Equation (5.4). This area re-normalization is done in an effort to accurately portray the interface cross-sectional area. The average of the longitudinal Kapitza resistances from both ends is found to be  $2.70 \times 10^{-11}$  Km<sup>2</sup>/W, which is three orders of magnitude smaller than typical values reported for the sidewall Kapitza resistance. While this value is subject to uncertainties in the area definition, convergence of the solution, and choice of nodes included in the summation, it is nevertheless supported by the fact that most of the heat flux in the CNT appears at the tube ends. The flux through the CNT changes sharply near the ends and is relatively flat in the center. This is a strong suggestion that the CNT picks up most of the heat flux from the tube ends.

The heat flux density through the CNT can be used to evaluate the CNT conductivity in a solvated environment. The heat flux density,  $J_z^{ss}$  is averaged over time and space, and divided by the temperature gradient via Fourier's law. For Case 1, the TC is computed to be 117.34 W/mK, which is a 32.28% diminishment from the in-vacuum result shown in Table 5.2. It is a slightly larger reduction compared to the 20 Å long (6,6) CNT presented by Thomas *et al.* [52], which was approximately 23%. This is a subtle suggestion that fluid external to the CNT also dampens the CNT's ability to propagate phonons.

## 5.6 Conclusion

Various CNTs were modelled using molecular dynamics in aqueous environments to better understand heat transfer in CNT-nanofluid systems. Results were compared against CNT in vacuum simulations presented in Chapter 4. CNT chiralities included (6,6), (10,10), and (9,0) primarily with a nominal length of about 25 nm. One case was performed with a 100 nm CNT. Heat transfer is simulated by applying a constant heat flux in the longitudinal direction to the fluid. Three different methods are utilized to analyze the heat transfer. The first is a direct application of Fourier's law in which a linear slope is fitted to the temperature gradient and an effective TC is obtained. This method proves questionable in that the temperature gradient is a clearly piecewise function and cannot be properly represented by a linear fit. Nevertheless, the effective TC can be used as a measurement of the enhancement. Moreover, the values were used to compute the effective TC of a bulk nanofluid system via application of the HC model. This analysis provided solutions on the order of experimental results and with similar nonlinearity trends, particularly with longer CNTs and larger solvation domains. The second method compares the phonon spectra of the CNTs in the vacuum and aqueous environments. The results are comparable to those reported by Thomas *et al.* [52]. The third method involves evaluating the atomistic heat flux via the Irving-Kirkwood formulation. The original formulation is expanded upon here to treat composite systems. The per-atom heat flux and temperature data is projected onto a finite element mesh so that the data can be presented as a spatial

mapping. The mappings are a novel presentation of heat transfer in atomistic systems and show the heat flow is bottle-necked into the CNT, primarily from the ends. The concentration of heat flow within the CNT is an order of magnitude larger than in the surrounding fluid, yet displays a very small temperature gradient. The localized heat flux and temperature descriptions allow for calculations of the component TCs and interfacial thermal resistance, or Kapitza resistance. The thermal conductivity of the CNT is found to be diminished by 32.28% relative to the in-vacuum counterpart. The sidewall Kapitza resistance is on the same order of magnitude as reported by Shenogin *et al.* [48]. On the other hand, the tube end Kapitza resistance is found to be three orders of magnitude smaller, suggesting preferential sites for energy exchange with the solvent located at the ends.

## Chapter 6

### Conclusions and Future Work

Heat transfer in carbon nanotube-based nanofluids has been shown to display anomalous thermal conductivity enhancements with a nonlinear relationship to particle concentration. This work was aimed at using an atomistic modelling approach to better understand the physics involved in the heat transfer. Atomistic simulations based on molecular dynamics were performed for a range of cases. Single-walled CNTs were simulated in both vacuum and aqueous environments. Sensitivity to physical and numerical parameters were explored. Various methods were employed to analyze the heat transfer through the systems in post processing.

A wide parameter sweep was performed for the CNT in vacuum simulations. These simulations were performed without the use of PBCs, so the CNTs have finite lengths and are not fictitiously constrained by any boundaries. The simulations revealed an increase in TC as CNT length and radius increase. These relationships are due to an increased availability of phonon modes. The length dependency tapers as the length approaches hundreds of nanometers because increased phonon modes leads to phonon-phonon scattering. The scattering shortens the phonon mean free path, which changes the ballistic phonon transport to fully diffusive transport. As temperature increases, the CNT TC is observed to decrease. This is also due to increased phonon-phonon

scattering.

A comparison between the Tersoff and AIREBO interatomic potentials was explored. Both potentials produce the same qualitative trends, but the Tersoff potential predicts higher values of TC, particularly at longer length scales. Phonon spectra analysis shows that the two potentials produce a few similar features, but mostly disparate spectra. Two methods for generating a temperature gradient were examined. The direct method imposes a temperature gradient and monitors the heat flux required to maintain that gradient. The Ikeshoji method imposes a heat flux and monitors the resulting temperature gradient. In general, both methods agreed well on TC measurements, although a few cases produced notably different results. Some replicate runs from the Ikeshoji method produced (steady state averaged) oscillatory temperature gradients, which measured significantly larger TCs. The reason for the oscillations remains unclear, however the phonon spectra analysis reveals that the Ikeshoji method enhances the first two frequency peaks relative to the direct method. Moreover, the simulations that produced oscillatory temperature gradients enhanced those peaks even further. The enhancement in these low frequency peaks is a proximate cause for the difference in thermal conductivity measurements.

Simulations were also performed with CNTs in an aqueous environment. CNTs were solvated in a box of a simple monatomic Lennard-Jones fluid. In these simulations, the AIREBO potential was used for carbon-carbon interactions, and Lennard-Jones was used for all remaining interatomic interactions. Heat transfer was simulated

using the Ikeshoji method. Different chiralities, lengths, and box sizes were simulated. This work expands on computational abilities provided by atomistic simulations. The simulation domains are unique for a number of reasons. PBCs are only used in the transverse directions to recover bulk conditions. They are not used in the longitudinal direction so that finite sizes can be examined and heat can be transferred unidirectionally. The simulations are set up such that heat is transferred parallel to the CNT axis, which is the direction heat will generally flow in CNT-composites. Furthermore, heat is added and removed from the fluid so that the interfacial resistance becomes an important factor.

It was observed that the temperature gradient through the system is a piecewise function, and that a single linear least squares fit was insufficient to fully describe the system. A line was fit to obtain a measurement for the magnitude of enhancement for nanofluid unit cell. The enhancement values were used in the HC model based on weighted averages. This revealed a slightly nonlinear trend and a similar order of magnitude compared to experimental results. The application of the HC model to the MD simulation results is in a way an extension of Yu and Choi's work, in which they postulated that a nanolayer is responsible for the TC enhancement. This work explicitly models the "nanolayer" and absorbs its contribution into a lumped particle TC. Since the outermost fluid in the MD simulations is nearly bulk-like, there is expected to be no interfacial resistance to the bulk fluid. This extension is particularly notable because the properties of the nanolayer are not assumed and



there are no tuning parameters. The results suggest that as the size of the fluid box is increased and the outer fluid escapes the CNT's volume of influence, the model becomes more nonlinear and the enhancement better resembles Choi *et al.*'s original results. Increasing the length of the CNT to more realistic lengths also improves the model.

The phonon spectra analysis was applied to these simulations and compared against the CNT in vacuum simulations. It was revealed that all the low frequency peaks which were enhanced previously in the Ikeshoji in-vacuum cases were damped out. The low frequency cascade still exists, however the peaks are slightly blueshifted. Moreover, a large broad peak around 50 THz was observed to be narrowed and also slightly blueshifted.

A novel analysis technique was developed which utilizes the Irving-Kirkwood formalism for atomic heat flux. The original formulation is decomposed logically into different contributions within a fluid-solid composite system. Given that solid-solid interactions are not pairwise in this case, the solid-solid heat flux is determined indirectly via conservation of energy arguments. The fluid-fluid heat flux is determined as in the original formalism, but the fluid-solid and solid-fluid heat fluxes lack the convection term because the kinetic energy can not be partitioned among interacting particles the way the potential energy is. The atomistic heat flux density is evaluated for all atoms. An atomistic-to-continuum coupling scheme is used to extract these quantities as a continuum variable at finite element mesh nodes. The quantities are

time- and ensemble-averaged, then spatially-averaged in cylindrical space over  $\theta$ . The resulting heat flux maps are a unique and novel way to study the data.

The heat flux maps reveal that the fluid transversally surrounding the CNT experiences very little heat flux, since the CNT is able to support most of the heat. The volume of influence of the CNT is found to extend further than  $10 \text{ \AA}$  beyond the CNT sidewall. Most of the heat is observed to enter and exit the tube from the free ends and only marginally from the sidewalls. The CNT acts as a tunnel for heat to bypass the less conductive fluid. The heat flux maps also provide sufficient data to evaluate the fluid TC and interfacial Kapitza resistance. The sidewall Kapitza resistance is computed to be on the  $\mathcal{O}(10^{-8}) \text{ Km}^2/\text{W}$ , which is in agreement with previous works. The tube end Kapitza resistance is found to be on the  $\mathcal{O}(10^{-11}) \text{ Km}^2/\text{W}$ , suggesting a path of least resistance through the tube ends.

The current model, while having many successes, is still an incomplete model of an actual nanofluid system. The application of the HC model is somewhat crude. Aside from the fact that it is based on a linear fit line to a piecewise function, it also does not take into consideration particle orientation. One possible future direction would be to build a finite element model of a bulk nanofluid system using the MD simulation results as unit cells in a large grid. Tensor rotation can be utilized to achieve different alignment configurations.

The MD model alone can be expanded on in numerous ways. More tests can be performed by simply changing the size of the fluid domain relative to the CNT.

Longer CNTs should be tested to better simulate real-world CNTs. More complicated solvents can be explored, e.g., a TIP3P model for water, long chain hydrocarbons, or polymers. Tube-tube interactions can be studied by solvating two CNTs in various configurations, i.e., parallel, perpendicular, and skew. Multi-walled CNTs can also be explored as an alternate tube-tube interaction. It is possible that tube-tube interactions plays a large role in producing the nonlinear trend because the onset of a percolation network can presumably provide a significant boost to the TC enhancement.

Finally, since the heat flux mappings suggested that most of the heat enters and leaves the CNT at the tube ends, this is a very useful prospect to explore. Computationally, a simple test could be to modify the Lennard-Jones parameters of the carbon atoms at the ends and observe the system's sensitivity to those parameters. Experimentally, one could consider adding functionalizations to the tube ends to improve the interfacial conductivity with the fluid.

## Bibliography

- [1] Das, S.K., Choi, S.U.S., and Patel, H.E., “Heat transfer in nanofluids—A review,” *Heat Transfer Engineering*, vol. 27, pp. 3–19, 2006.
- [2] Choi, S.U.S. and Eastman, J.A., “Enhancing thermal conductivity of fluids with nanoparticles,” *ASME - FED*, vol. 231, pp. 99–105, 1995.
- [3] Maxwell, J.C., *A Treatise on Electricity and Magnetism*, vol. 1. Clarendon Press, Oxford, U.K., 2nd ed., 1881.
- [4] Maxwell-Garnett, J.C., “Colours in metal glasses and in metallic films,” *Philosophical Transactions of the Royal Society of London A*, vol. 203, no. 359-371, 1904.
- [5] Hamilton, R.L. PhD thesis, University of Oklahoma, 1960.
- [6] Hamilton, R.L. and Crosser, O.K., “Thermal conductivity of heterogeneous two component systems,” *Industrial and Engineering Chemistry Fundamentals*, vol. 1, no. 3, pp. 187–191, 1962.
- [7] Rocha, A. and Acrivos, A., “On the effective thermal conductivity of dilute dispersions: Highly conducting inclusions of arbitrary shape,” *The Quarterly*

- Journal of Mechanics and Applied Mathematics*, vol. 26, no. 4, pp. 441–455, 1973.
- [8] Lee, S., Choi, S.U.S., Li, S., and Eastman, J.A., “Measuring thermal conductivity of fluids containing oxide nanoparticles,” *Transactions of ASME, Journal of Heat Transfer*, vol. 121, pp. 280–289, 1999.
- [9] Wang, X., Xu, X., and Choi, S.U.S., “Thermal conductivity of nanoparticle-fluid mixture,” *Journal of Thermophysics and Heat Transfer*, vol. 13, pp. 474–480, 1999.
- [10] Xie, H.Q., Wang, J.C., Xi, T.G., Liu, Y., and Ai, F., “Thermal conductivity enhancement of suspensions containing nanosized alumina particles,” *Journal of Applied Physics*, vol. 91, no. 7, pp. 4568–4572, 2002.
- [11] Xie, H.Q., Wang, J.C., Xi, T.G., Liu, Y., Ai, F., and Wu, Q.R., “Thermal conductivity enhancement of suspensions containing nanosized alumina particles,” *Journal of Applied Physics*, vol. 21, pp. 1469–1471, 2002.
- [12] Murshed, S.M.S., Leong, K.C., and Yang, C., “Enhanced thermal conductivity of TiO<sub>2</sub>-water based nanofluids,” *International Journal of Thermal Science*, vol. 44, pp. 367–373, 2005.
- [13] Xuan, Y. and Li, Q., “Heat transfer enhancement of nanofluids,” *International Journal of Heat and Fluid Flow*, vol. 21, no. 1, pp. 58–64, 2000.

- [14] Eastman, J.A., Choi, S.U.S., Li, S., Yu, W., and Thompson, L.J., "Anomalously increased effective thermal conductivities of ethylene glycol based nanofluids containing copper nanoparticles," *Applied Physics Letters*, vol. 78, no. 6, pp. 718–720, 2001.
- [15] Patel, H.E., Das, S.K., Sundararajan, T., Sreekumaran, N.A., George, B., and Pradeep, T., "Thermal conductivities of naked and monolayer protected metal nanoparticle based nanofluids: Manifestation of anomalous enhancement and chemical effects," *Applied Physics Letters*, vol. 83, no. 14, 2003.
- [16] Hong, T.K., Yang, H.S., and Choi, C.J., "Study of the enhanced thermal conductivity of Fe nanofluids," *Journal of Applied Physics*, vol. 97, no. 6, p. 064311, 2005.
- [17] Iijima, S., "Helical microtubules of graphitic carbon," *Nature*, vol. 354, no. 6348, pp. 56–58, 1991.
- [18] Dresselhaus, M.S., Dresselhaus, G., and Saito, R., "Physics of carbon nanotubes," *Carbon*, vol. 33, no. 7, pp. 883–891, 1995.
- [19] Rao, C.N.R., Satishkumar, B.C., Govindaraj, A., and Nath, M., "Nanotubes," *ChemPhysChem*, vol. 2, no. 2, pp. 78–105, 2001.
- [20] Dresselhaus, M.S., Dresselhaus, G., and Avouris, P., *Carbon nanotubes: synthesis, structure, properties, and applications*, vol. 80 of *Topics in Applied Physics*,

- ch. Phonons and Thermal Properties of Carbon Nanotubes. Berlin: Springer-Verlag, 2001. Chapter by Hone, J.
- [21] Choi, S.U.S., Zhang, Z.G., Yu, W., Lockwood, F.E., and Grulke, E.A., "Anomalous thermal conductivity enhancement in nanotube suspensions," *Applied Physics Letters*, vol. 79, pp. 2252–2254, 2001.
- [22] Xie, H., Lee, H., Youn, W., and Choi, M., "Nanofluids containing multiwalled carbon nanotubes and their enhanced thermal conductivities," *Journal of Applied Physics*, vol. 94, no. 8, pp. 4967–4971, 2003.
- [23] Liu, M.-S., Lin, M.C.-C., Huang, I.-T., and Wang, C.-C., "Enhancement of thermal conductivity with carbon nanotube for nanofluids," *International Communications in Heat and Mass Transfer*, vol. 32, no. 9, pp. 1202–1210, 2005.
- [24] Ding, Y., Alias, H., Wen, D., and Williams, R.A., "Heat transfer of aqueous suspensions of carbon nanotubes (CNT nanofluids)," *International Journal of Heat and Mass Transfer*, vol. 49, no. 1-2, pp. 240–250, 2006.
- [25] Marquis, F.D.S. and Chibante, L.P.F., "Improving the heat transfer of nanofluids and nanolubricants with carbon nanotubes," *Journal of the Minerals, Metals and Materials Society*, vol. 57, no. 12, pp. 32–43, 2005.
- [26] Hwang, Y.J., Ahn, Y.C., Shin, H.S., Lee, C.G., Kim, G.T., Park, H.S., and Lee, J.K., "Investigation on characteristics of thermal conductivity enhancement of nanofluids," *Current Applied Physics*, vol. 6, no. 6, pp. 1068–1071, 2006.

- [27] Assael, M.J., Metaxa, I.N., Kakosimos, K., and Constantinou, D., "Thermal conductivity of nanofluids - Experimental and theoretical," *International Journal of Thermophysics*, vol. 27, no. 4, pp. 999–1017, 2006.
- [28] Yu, W. and Choi, S.U.S., "The role of interfacial layers in the enhanced thermal conductivity of nanofluids: A renovated Hamilton-Crosser model," *Journal of Nanoparticle Research*, vol. 6, pp. 355–361, 2004.
- [29] Yu, W. and Choi, S.U.S., "The role of interfacial layers in the enhanced thermal conductivity of nanofluids: A renovated Maxwell model," *Journal of Nanoparticle Research*, vol. 5, pp. 167–171, 2003.
- [30] Leong, K.C., Yang, C., and Murshed, S.M.S., "A model for the thermal conductivity of nanofluids – the effect of interfacial layer," *Journal of Nanoparticle Research*, vol. 8, pp. 245–254, 2006.
- [31] Murshed, S.M.S., Leong, K.C., and Yang, C., "Thermal conductivity of nanoparticle suspensions (nanofluids)," *IEEE, 0-7803-9358-9*, pp. 155–158, 2006.
- [32] Nan, C.-W., "Physics of inhomogeneous inorganic materials," *Progress in Materials Science*, vol. 37, no. 1, pp. 1–116, 1993.
- [33] Nan, C.-W., Birringer, R., Clarke, D.R., and Gleiter, H., "Effective thermal conductivity of particulate composites with interfacial thermal resistance," *Journal of Applied Physics*, vol. 81, no. 10, pp. 1623–1628, 1997.



- [34] Nan, C.-W., Shi, Z., and Lin, Y., "A simple model for thermal conductivity of carbon nanotube-based composites," *Chemical Physics Letters*, vol. 375, no. 5-6, pp. 666–669, 2003.
- [35] Nan, C.-W., Liu, G., Lin, Y., and Li, M., "Interface effect on thermal conductivity of carbon nanotube composites," *Applied Physics Letters*, vol. 85, no. 16, pp. 3549–3551, 2004.
- [36] Kapitza, P.L., "The study of heat transfer in helium II," in *Collected Papers of P.L. Kapitza, Volume II* (ter Haar, D., ed.), Oxford: Pergamon Press, 1967.
- [37] Bruggeman, D.A.G., "Berechnung verschiedener physikalischer konstanten von heterogenen substanzen. I. Dielektrizitätskonstanten und leitfähigkeiten der mischkörper aus isotropen substanzen," *Annalen der Physik*, vol. 416, no. 7, pp. 636–664, 1935.
- [38] Jiajun, W. and Xiao-Su, Y., "Effects of interfacial thermal barrier resistance and particle shape and size on the thermal conductivity of AlN/PI composites," *Composites Science and Technology*, vol. 64, no. 10-11, pp. 1623–1628, 2004.
- [39] Gao, L., Zhou, X., and Ding, Y., "Effective thermal and electrical conductivity of carbon nanotube composites," *Chemical Physics Letters*, vol. 434, no. 4-6, pp. 297–300, 2007.
- [40] Foygel, M., Morris, R.D., Anez, D., French, S., and Sobolev, V.L., "Theoretical and computational studies of carbon nanotube composites and suspen-

- sions: Electrical and thermal conductivity,” *Physical Review B*, vol. 71, no. 10, p. 104201, 2005.
- [41] Strauss, M.T. and Pober, R.L., “Nanotubes in liquids: Effective thermal conductivity,” *Journal of Applied Physics*, vol. 100, no. 8, p. 084328, 2006.
- [42] Vadasz, J.J., Govender, S., and Vadasz, J., “Heat transfer enhancement in nano-fluids suspensions: Possible mechanisms and explanations,” *International Journal of Heat and Mass Transfer*, vol. 48, no. 13, pp. 2673–2683, 2005.
- [43] Vadasz, P., “Heat conduction in nanofluid suspensions,” *Journal of Heat Transfer*, vol. 128, no. 5, pp. 465–477, 2006.
- [44] Wang, J. and Wang, J.S., “Carbon nanotube thermal transport: Ballistic to diffusive,” *Applied Physics Letters*, vol. 88, no. 11, p. 111909, 2006.
- [45] Xie, H., Fujii, M., and Zhang, X., “Effect of interfacial nanolayer on the effective thermal conductivity of nanoparticle–fluid mixture,” *International Journal of Heat and Mass Transfer*, vol. 48, no. 14, pp. 2926–2932, 2005.
- [46] Zhou, X.F. and Gao, L., “Effective thermal conductivity in nanofluids of non-spherical particles with interfacial thermal resistance: Differential effective medium theory,” *Journal of Applied Physics*, vol. 100, no. 2, p. 024913, 2006.
- [47] Huxtable, S.T., Cahill, D.G., Shenogin, S., Xue, L., Ozisik, R., Barone, P., Usrey, M., Strano, M.S., Siddons, G., Shim, M., and Keblinski, P., “Interfacial

- heat flow in carbon nanotube suspensions,” *Nature Materials*, vol. 2, no. 11, pp. 731–734, 2003.
- [48] Shenogin, S., Xue, L., Ozisik, R., Keblinski, P., and Cahill, D., “Role of thermal boundary resistance on the heat flow in carbon-nanotube composites,” *Journal of Applied Physics*, vol. 95, no. 12, pp. 8136–8144, 2004.
- [49] Shenogin, S., Bodapati, A., Xue, L., Ozisik, R., and Keblinski, P., “Effect of chemical functionalization on thermal transport of carbon nanotube composites,” *Applied Physics Letters*, vol. 85, no. 12, pp. 2229–2231, 2004.
- [50] Ikeshoji, T. and Hafskjold, B., “Non-equilibrium molecular dynamics calculation of heat conduction in liquid and through liquid-gas interface,” *Molecular Physics*, vol. 81, no. 2, pp. 251–261, 1994.
- [51] Unnikrishnan, V.U., Banerjee, D., and Reddy, J.N., “Atomistic-mesoscale interfacial resistance based thermal analysis of carbon nanotube systems,” *International Journal of Thermal Sciences*, vol. 47, no. 12, pp. 1602–1609, 2008.
- [52] Thomas, J.A., Iutzi, R.M., and McGaughey, A.J.H., “Thermal conductivity and phonon transport in empty and water-filled carbon nanotubes,” *Physical Review B*, vol. 80, no. 4, p. 045413, 2010.
- [53] Plimpton, S.J., “Fast parallel algorithms for short-range molecular dynamics,” *Journal of Computational Physics*, vol. 117, no. 1, pp. 1–19, 1995.

- [54] Wagner, G.J., Jones, R.E., Templeton, J.A., and Parks, M.L., “An atomistic-to-continuum coupling method for heat transfer in solids,” *Computer Methods in Applied Mechanics and Engineering*, vol. 197, no. 41-42, pp. 3351–3365, 2008.
- [55] Zimmerman, J.A., Webb, E.B. III, Hoyt, J.J., Jones, R.E., Klein, P.A., and Bammann, D.J., “Calculation of stress in atomistic simulation,” *Modelling and Simulation in Materials Science and Engineering*, vol. 12, no. 4, pp. S319–S332, 2004.
- [56] Frenkel, D. and Smit, B., *Understanding Molecular Simulation: From Algorithms to Applications*. Academic Press, second ed., 2002.
- [57] Verlet, L., “Computer “experiments” on classical fluids. I. Thermodynamical properties of Lennard-Jones molecules,” *Physical Review*, vol. 159, no. 1, pp. 98–103, 1967.
- [58] Verlet, L., “Computer “experiments” on classical fluids. II. Equilibrium correlation functions,” *Physical Review*, vol. 165, no. 1, pp. 201–214, 1968.
- [59] Jones, J.E., “On the determination of molecular fields. II. From the equation of state of a gas,” *Proceedings of the Royal Society of London. Series A, Containing Papers of a Mathematical and Physical Character*, vol. 106, no. 738, pp. 463–477, 1924.
- [60] MacKerell, A.D., Bashford, D., Bellott, M., Dunbrack, R.L., Evanseck, J.D., Field, M.J., Fischer, S., Gao, J., Guo, H., Ha, S., and et al., “All-atom empirical

- potential for molecular modeling and dynamics studies of proteins,” *Journal of Physical Chemistry B*, vol. 102, no. 18, pp. 3586–3616, 1998.
- [61] Tersoff, J., “New empirical approach for the structure and energy of covalent systems,” *Physical Review B*, vol. 37, no. 12, pp. 6991–7000, 1988.
- [62] Tersoff, J., “Empirical interatomic potential for silicon with improved elastic properties,” *Physical Review B*, vol. 38, no. 14, pp. 9902–9905, 1988.
- [63] Tersoff, J., “Modeling solid-state chemistry: Interatomic potentials for multi-component systems,” *Physical Review B*, vol. 39, no. 8, pp. 5566–5568, 1988.
- [64] Brenner, D.W., “Empirical potential for hydrocarbons for use in simulating the chemical vapor deposition of diamond films,” *Physical Review B*, vol. 42, no. 15, pp. 9458–9471, 1990.
- [65] Finnis, M.W. and Sinclair, J.E., “A simple empirical  $N$ -body potential for transition metals,” *Philosophical Magazine A*, vol. 50, no. 1, pp. 45–55, 1984.
- [66] Brenner, D.W., Shenderova, O.A., Harrison, J.A., Stuart, S.J., Ni, B., and Sinnott, S.B., “A second-generation reactive empirical bond order (REBO) potential energy expression for hydrocarbons,” *Journal of Physics: Condensed Matter*, vol. 14, no. 4, pp. 783–802, 2002.
- [67] Stuart, S.J., Tutein, A.B., and Harrison, J.A., “A reactive potential for hydrocarbons with intermolecular interactions,” *Journal of Chemical Physics*,

- vol. 112, no. 14, pp. 6472–6486, 2000.
- [68] Pauling, L., *The Nature of the Chemical Bond*. Cornell University Press, 3rd ed., 1960.
- [69] Ewald, P.P., “Die berechnung optischer und elektrostatischer gitterpotentiale,” *Annalen der Physik*, vol. 369, no. 3, pp. 253–287, 1921.
- [70] Hockney, R.W. and Eastwood, J.W., *Computer simulation using particles*, ch. 8, pp. 267–304. McGraw-Hill, 1988.
- [71] Nosé, S., “A unified formulation of the constant temperature molecular dynamics methods,” *Journal of Chemical Physics*, vol. 81, no. 1, pp. 511–519, 1984.
- [72] Hoover, W.G., “Canonical dynamics: Equilibrium phase-space distributions,” *Physical Review A*, vol. 31, no. 3, pp. 1695–1697, 1985.
- [73] Hoover, W.G., *Computational Statistical Mechanics*. Amsterdam, NL: Elsevier, 1991.
- [74] Schelling, P.K., Phillpot, S.R., and Keblinski, P., “Comparison of atomic-level simulation methods for computing thermal conductivity,” *Physical Review B*, vol. 65, no. 14, p. 144306, 2002.
- [75] Zhong, H. and Lukes, J., “Thermal conductivity of single-wall carbon nanotubes,” in *Proceedings of IMECE04*, ASME International Mechanical Engineering Congress and Exposition, 2004.

- [76] Lukes, J. and Zhong, H., "Thermal conductivity of individual single-wall carbon nanotubes," *Journal of Heat Transfer*, vol. 129, no. 6, pp. 705–716, 2007.
- [77] Müller-Plathe, F. and Reith, D., "Cause and effect reversed in non-equilibrium molecular dynamics: an easy route to transport coefficients," *Computational and Theoretical Polymer Science*, vol. 9, no. 3, pp. 203–209, 1999.
- [78] Maiti, A., Mahan, G.D., and Pantelides, S.T., "Dynamical simulations of nonequilibrium processes - Heat flow and the Kapitza resistance across grain boundaries," *Solid State Communications*, vol. 102, no. 7, pp. 517–521, 1997.
- [79] Schelling, P.K. and Phillpot, S.R., "Mechanism of the cubic-to-tetragonal phase transition in zirconia and yttria-stabilized zirconia by molecular-dynamics simulation," *Journal of the American Ceramic Society*, vol. 84, no. 7, pp. 1609–1619, 2001.
- [80] Oligschleger, C. and Schön, J.C., "Simulation of thermal conductivity and heat transport in solids," *Physical Review B*, vol. 59, no. 6, pp. 4125–4133, 1999.
- [81] Jund, P. and Jullien, R., "Molecular-dynamics calculation of the thermal calculation of vitreous silica," *Physical Review B*, vol. 59, no. 21, pp. 13707–13711, 1999.
- [82] Baranyai, A., "Heat flow studies for large temperature gradients by molecular dynamics simulation," *Physical Review E*, vol. 54, no. 6, pp. 6911–6917, 1996.

- [83] Poetzsch, R.H.H. and Böttger, H., “Interplay of disorder and anharmonicity in heat conduction: Molecular-dynamics study,” *Physical Review B*, vol. 50, no. 21, pp. 15757–15763, 1994.
- [84] Evans, D.J., “Homogeneous NEMD algorithm for thermal conductivity-Application of non-canonical linear response theory,” *Physics Letters A*, vol. 91, no. 9, pp. 457–460, 1982.
- [85] Gillan, M.J. and Dixon, M., “The calculation of thermal conductivities by perturbed molecular dynamics simulation,” *Journal of Physics C: Solid State Physics*, vol. 16, no. 5, pp. 869–878, 1983.
- [86] Berber, S., Kwon, Y.-K., and Tománek, D., “Unusually high thermal conductivity of carbon nanotubes,” *Physical Review Letters*, vol. 84, no. 20, pp. 4613–4616, 2000.
- [87] Paolini, G.V., Ciccotti, G., and Massobrio, C., “Nonlinear thermal response of a Lennard-Jones fluid near the triple point,” *Physical Review A*, vol. 34, no. 2, pp. 1355–1362, 1986.
- [88] Maruyama, S., “A molecular dynamics simulation of heat conduction of a finite length single-walled carbon nanotube,” *Microscale Thermophysical Engineering*, vol. 7, no. 1, pp. 41–50, 2003.
- [89] Che, J., Çağın, T., and Goddard, W.A., “Thermal conductivity of diamond and



- related materials from molecular dynamics simulations,” *Journal of Chemical Physics*, vol. 133, no. 16, pp. 6888–6900, 2000.
- [90] Che, J., Çağın, T., and Goddard, W.A. III, “Thermal conductivity of carbon nanotubes,” *Nanotechnology*, vol. 11, no. 2, pp. 65–69, 2000.
- [91] Li, J., Porter, L., and Yip, S., “Atomistic modeling of finite-temperature properties of crystalline  $\beta$ -SiC: II. Thermal conductivity and effects of point defects,” *Journal of Nuclear Materials*, vol. 255, no. 2, pp. 139–152, 1998.
- [92] Volz, S.G. and Chen, G., “Molecular-dynamics simulations of thermal conductivity of silicon crystals,” *Physical Review B*, vol. 61, no. 4, pp. 2651–2656, 2000.
- [93] Lee, Y.H., Biswas, R., Soukoulis, C.M., Wang, C.Z., Chan, C.T., and Ho, K.M., “Molecular-dynamics simulation of thermal conductivity in amorphous silicon,” *Physics Review B*, vol. 43, no. 8, pp. 6573–6580, 1991.
- [94] Ladd, A.J.C. and Moran, B., “Lattice thermal conductivity: A comparison of molecular dynamics and anharmonic lattice dynamics,” *Physical Review B*, vol. 34, no. 8, pp. 5058–5064, 1986.
- [95] Vogelsang, R., Hoheisel, C., and Ciccotti, G., “Thermal conductivity of the Lennard-Jones liquid by molecular dynamics calculations,” *Journal of Chemical Physics*, vol. 86, no. 11, pp. 6371–6375, 1987.

- [96] Hardy, R.J., “Formulas for determining local properties in molecular-dynamics simulations: Shock waves,” *Journal of Chemical Physics*, vol. 76, pp. 622–628, 1982.
- [97] Hardy, R.J. and Karo, A.M., “Stress and energy flux in the vicinity of a shock front,” in *Shock Compression of Condensed Matter: Proceedings of the American Physical Society Topical Conference*, pp. 161–164, 1990.
- [98] Hardy, R.J., Root, S., and Swanson, D.R., “Continuum properties from molecular simulations,” in *AIP Conference Proceedings*, 620, pp. 363–366, American Physical Society, 2002.
- [99] Jorgensen, W.L., Chandrasekhar, J., Madura, J.D., Impey, R.W., and Klein, M.L., “Comparison of simple potential functions for simulating liquid water,” *Journal of Chemical Physics*, vol. 79, no. 2, pp. 926–935, 1983.
- [100] Werder, T., Walther, J.H., Jaffe, R.L., Halicioglu, T., and Koumoutsakos, P., “On the water-carbon interaction for use in molecular dynamics simulations of graphite and carbon nanotubes,” *Journal of Physical Chemistry B*, vol. 107, pp. 1345–1352, 2003.
- [101] Lee, J.W., Meade, A.J., Jr., Barrera, E.V., and Templeton, J.A., “Dependencies of the thermal conductivity of individual single-walled carbon nanotubes,” *Proceedings of the Institution of Mechanical Engineers, Part N, Journal of Nanoengineering and Nanosystems*, vol. 224, no. 1-2, pp. 41–54, 2011.

- [102] Kim, P., Shi, L., Majumdar, A., and McEuen, P.L., “Thermal transport measurements of individual multiwalled nanotubes,” *Physical Review Letters*, vol. 87, no. 21, p. 215502, 2001.
- [103] Yu, C.H., Shi, L., Yao, Z., Li, D.Y., and Majumdar, A., “Thermal conductance and thermopower of an individual single-wall carbon nanotube,” *Nano Letters*, vol. 5, no. 9, pp. 1842–1846, 2005.
- [104] Fujii, M., Zhang, X., Xie, H., Ago, H., Takahashi, K., and Ikuta, T., “Measuring the thermal conductivity of a single carbon nanotube,” *Physical Review Letters*, vol. 95, no. 6, p. 065502, 2005.
- [105] Pop, E., Mann, D., Wang, Q., Goodson, K., and Dai, H., “Thermal conductance of an individual single-wall carbon nanotube above room temperature,” *Nano Letters*, vol. 6, no. 1, pp. 96–100, 2006.
- [106] Choi, T.-Y., Poulikakos, D., Tharian, J., and Sennhauser, U., “Measurement of the thermal conductivity of individual carbon nanotubes by the four-point three- $\omega$  method,” *Nano Letters*, vol. 6, no. 8, pp. 1589–1593, 2006.
- [107] Hu, X.J., Padilla, A.A., Xu, J., Fisher, T.S., and Goodson, K.E., “3-omega measurements of vertically oriented carbon nanotubes on silicon,” *Journal of Heat Transfer*, vol. 128, no. 11, pp. 1109–1113, 2006.
- [108] Akoshima, M., Hata, K., Futaba, D.N., Mizuno, K., Baba, T., and Yumura, M.,

- “Thermal diffusivity of single-walled carbon nanotube forest measured by laser flash method,” *Japanese Journal of Applied Physics*, vol. 48, p. 05EC07, 2009.
- [109] Dresselhaus, M and Eklund, P.C., “Phonons in carbon nanotubes,” *Advanced Physics*, vol. 49, no. 6, pp. 705–814, 2000.
- [110] Yi, W., Lu, L., Zhang, D.-L., Pan, Z.W., and Xie, S.S., “Linear specific heat of carbon nanotubes,” *Physical Review B*, vol. 59, no. 14, pp. R9015–R9018, 1999.
- [111] Osman, M.A. and Srivastava, D., “Temperature dependence of the thermal conductivity of single-wall carbon nanotubes,” *Nanotechnology*, vol. 12, no. 1, pp. 21–24, 2001.
- [112] Hansen, J.-P. and McDonald, I.R., *Theory of Simple Liquids*, ch. 5, pp. 109–146. London: Academic, 2nd ed., 1986.
- [113] Moreland, J.F., Freund, J.B., and Chen, G., “The disparate thermal conductivity of carbon nanotubes and diamond nanowires studied by atomistic simulation,” *Microscale Thermophysical Engineering*, vol. 8, no. 1, pp. 61–69, 2004.
- [114] Padgett, C.W. and Brenner, D.W., “Influence of chemisorption on the thermal conductivity of single-wall carbon nanotubes,” *Nano Letters*, vol. 4, no. 6, pp. 1051–1053, 2004.
- [115] Mingo, N. and Broido, D.A., “Length dependence of carbon nanotube thermal conductivity and the “problem of long waves”,” *Nano Letters*, vol. 5, no. 7,

- pp. 1221–1225, 2005.
- [116] Mingo, N. and Broido, D.A., “Carbon nanotube ballistic thermal conductance and its limits,” *Physical Review Letters*, vol. 95, no. 9, p. 096105, 2005.
- [117] Donadio, D. and Galli, G., “Thermal conductivity of isolated and interacting carbon nanotubes: Comparing results from molecular dynamics and the Boltzmann transport equation,” *Physical Review Letters*, vol. 99, no. 25, p. 255502, 2007.
- [118] Mahan, G.D. and Jeon, G.S., “Flexure modes in carbon nanotubes,” *Physical Review B*, vol. 70, no. 7, p. 075405, 2004.
- [119] Frey, J.T. and Doren, D.J., “Tubegen 3.2.” University of Delaware, Newark DE, 2003.
- [120] Ashcroft, N.W. and Mermin, N.D., *Solid State Physics*. Thomson Learning, 1976.
- [121] Kittel, C., *Introduction to Solid State Physics*. New York: John Wiley & Sons, 7th ed., 1996.
- [122] Sokhan, V.P., Nicholson, D., and Quirke, N., “Phonon spectra in model carbon nanotubes,” *Journal of Chemical Physics*, vol. 113, no. 5, pp. 2007–2015, 2000.
- [123] Fouquet, M., Telg, H., Maultzsch, J., Wu, Y., Chandra, B., Hone, J., Heinz, T.F., and Thomsen, C., “Longitudinal optical phonons in metallic and semi-

- conducting carbon nanotubes,” *Physical Review Letters*, vol. 102, p. 075501, 2009.
- [124] Sastry, N.N.V., Bhunia, A., Sundararajan, T., and Das, S.K., “Predicting the effective thermal conductivity of carbon nanotube based nanofluids,” *Nanotechnology*, vol. 19, p. 055704, 2008.
- [125] Sun, H., Mumby, S.J., Maple, J.R., and Hagler, A.T., “An ab initio all-atom force field for polycarbonates,” *Journal of the American Chemical Society*, vol. 116, no. 7, pp. 2978–2987, 1994.
- [126] Rappe, A.K., Casewit, C.J., Colwell, K.S., Goddard, W.A. III, and Skiff, W.M., “UFF, a full periodic table force field for molecular mechanics and molecular dynamics simulations,” *Journal of the American Chemical Society*, vol. 114, no. 25, pp. 10024–10035, 1992.
- [127] Legoas, S.B., Coluci, V.R., Braga, S.F., Coura, P.Z., Dantas, S.O., and Galvão, D.S., “Molecular-dynamics simulations of carbon nanotubes as gigahertz oscillators,” *Physical Review Letters*, vol. 90, no. 5, 2003.
- [128] Zimmerman, J.A., Jones, R.E., and Templeton, J.A., “A material frame approach for evaluating continuum variables in atomistic simulations,” *Journal of Computational Physics*, vol. 229, no. 6, pp. 2364–2389, 2010.
- [129] Irving, J.H. and Kirkwood, J.G., “The statistical mechanical theory of transport

processes. IV. The equations of hydrodynamics," *Journal of Chemical Physics*,  
vol. 18, no. 6, pp. 817–829, 1950.